POTENTIAL AND GEOMECHANICAL RISKS OF HIGH-TEMPERATURE HEAT STORAGE IN DEEP RESERVOIRS

Zur Erlangung des akademischen Grades eines

DOKTORS DER NATURWISSENSCHAFTEN (Dr. rer. nat.)

von der KIT Fakultät für

Bauingenieur-, Geo- und Umweltwissenschaften

des Karlsruher Instituts für Technologie (KIT)

genehmigte

DISSERTATION

von

M.Sc. Kai Robin Stricker

aus Waldshut-Tiengen

Tag der mündlichen Prüfung: 12. Juni 2024

Referent: Prof. Dr. Thomas Kohl

Korreferent: Prof. Dr. Philip Vardon

Karlsruhe 2024

ABSTRACT

As the latest report of the Intergovernmental Panel on Climate Change (IPCC, 2023) unequivocally demonstrates, global warming poses an urgent challenge for humanity. The undeniable influence of human-induced greenhouse gas emissions on global warming necessitates a rapid and far-reaching reduction in emissions across all sectors. To achieve this, a reduction in fossil fuel consumption and a corresponding increase in the share of renewable energy sources are essential. However, the intermittent nature of most renewable energy sources, particularly solar and wind power, illustrates the importance of complementary energy storage systems with substantial capacities. Here, subsurface systems, such as aquifer thermal energy storage (ATES), emerge as the most viable option due to their unparalleled storage capabilities.

While ATES systems are primarily employed in low-temperature applications, such as residential and greenhouse heating, the potential for high-temperature (HT)-ATES systems to supply heat for industrial needs or district heating networks, remains largely untapped. The lack of operational or demonstrator HT-ATES systems further underscores the need for extensive research in this area. The DeepStor project, located near Karlsruhe in southwest Germany, aims to address this gap by establishing a research infrastructure to demonstrate the feasibility of HT-ATES in depleted hydrocarbon reservoirs in the Upper Rhine Graben (URG), harnessing Germany's largest heat anomaly.

This thesis presents a comprehensive investigation into the viability of utilizing oil reservoirs as HT-ATES systems, particularly focusing on the planned research infrastructure DeepStor as a case study. Additionally, the conducted research assesses potential hazards, such as ground surface movements and induced seismicity, to provide insights for the practical implementation of HT-ATES systems as a critical element in the energy transition.

In the **first study** (Chapter 3), the suitability of depleted oil reservoirs in the URG for HT-ATES applications is quantified. By gathering and analyzing existing petrophysical and geological data, a thermo-hydraulic numerical model is developed to evaluate the storage potential of these reservoirs. The simulations indicate storage capacities of up to 10 GWh with recovery efficiencies around 80 % when operated with seasonal injection/production cycles. Notably, the results highlight the significant influence of reservoir thickness, injection/production flow rates, and well geometry on the storage capacity. The study concludes that approximately 80 % of the examined oil reservoirs in the URG could be

repurposed as HT-ATES systems.

The **second study** (Chapter 4) investigates the impact of stress changes induced by HT-ATES operations on the reservoir and its potential influence on ground surface deformation. A simplified coupled thermo-hydraulic-mechanical (THM) numerical model representing an average oil field in the URG is employed. The results demonstrate that stress changes and deformation in the reservoir are primarily driven by thermoelasticity (90 % of the total displacements), while ground surface displacements are predominantly governed by poroelasticity. Moreover, it is shown that ground surface displacements are significantly attenuated compared to those in the reservoir, resulting in negligible sub-mm-scale movements. In contrast to other forms of subsurface utilization, the study highlights that the cyclic operation of HT-ATES systems effectively mitigates cumulative uplift at the ground surface. A sensitivity analysis identifies the reservoir depth, the elastic modulus, and the injection/production flow rate as the parameters that mainly control ground surface movements.

The **third study** (Chapter 5) evaluates the potential risk of fault reactivation and induced seismicity associated with HT-ATES operations at the planned DeepStor research infrastructure. In contrast to the simplified THM model of the second study, a detailed thermo-hydraulic numerical model of the DeepStor site, based on 3D seismic data, is combined with semi-analytical stress calculations along a fault plane near the planned well doublet. The simulation results suggest a relatively low risk for fault reactivation and induced seismicity, attributed in part to the mechanically stabilizing effect of hot water injection. The study identifies stress gradients, the angle between the stress field orientation and the fault strike, as well as operational parameters, such as injection/production flow rates and the distance between the HT-ATES well doublet and the fault as the most sensitive factors influencing fault failure. It also emphasizes that these identified risks can be effectively mitigated through a comprehensive operational framework considering these operational and subsurface boundary conditions.

This thesis presents evidence supporting the general suitability of depleted hydrocarbon reservoirs in the URG for HT-ATES applications. Moreover, the conducted studies indicate that only minimal risks for ground surface movements and induced seismicity can be expected. Nevertheless, to ensure the safe operation of HT-ATES systems, it is essential to implement an effective mitigation strategy that encompasses (i) maintaining a sufficient distance between the well doublet and nearby faults to minimize the likelihood of induced seismicity, (ii) carefully selecting injection/production flow rates that align with the reservoir transmissivity, thereby regulating their impact on ground surface movements and induced seismicity, and (iii) considering sufficiently deep reservoir formations to reduce the impact on ground surface deformation.

KURZFASSUNG

Wie der jüngste Bericht des „Intergovernmental Panel on Climate Change“ (IPCC, 2023) unmissverständlich zeigt, stellt die globale Erwärmung eine äußerst dringliche Herausforderung für die Menschheit dar. Der unbestreitbare Einfluss der vom Menschen verursachten Treibhausgasemissionen auf die globale Erwärmung macht eine rasche und weitreichende Reduktion der Emissionen in allen Sektoren erforderlich. Um dies zu erreichen, sind eine Reduzierung der Nutzung fossiler Brennstoffe und eine entsprechender Ausbau der erneuerbaren Energien unerlässlich. Da die meisten erneuerbaren Energiequellen, insbesondere Solar- und Windenergie, jedoch nicht kontinuierlich zur Verfügung stehen, sind ergänzende Energiespeichersysteme mit hohen Speicherkapazitäten erforderlich. Hier spielen unterirdische Speichersysteme, wie z.B. Wärmespeicherung in Aquiferen („aquifer thermal energy storage“; ATES), aufgrund ihrer besonders hohen Speicherkapazität eine wichtige Rolle.

Während ATES-Systeme hauptsächlich für Anwendungen im Niedertemperaturbereich wie der Beheizung von Wohn- und Gewächshäusern eingesetzt werden, bleibt das Potenzial von Hochtemperatursystemen („high-temperature“ (HT)-ATES), z.B. für die Wärmeversorgung der Industrie oder von Fernwärmenetzen, noch weitgehend ungenutzt. Die geringe Anzahl an im Betrieb befindlichen Systemen oder Demonstrationsprojekten unterstreicht den Bedarf an umfassender Forschung zu HT-ATES. Das DeepStor-Projekt in der Nähe von Karlsruhe im Südwesten Deutschlands zielt darauf ab mit der Einrichtung einer Forschungsinfrastruktur diese Lücke zu schließen, um die Machbarkeit von HT-ATES in erschöpften Kohlenwasserstoff-Reservoiren im Oberrheingraben (ORG) zu demonstrieren und Deutschlands größte Wärmeanomalie für Wärmespeicherung zu nutzen.

In dieser Arbeit wird eine umfassende Untersuchung der Machbarkeit der Nutzung von Erdöllagerstätten als HT-ATES-Systeme vorgestellt, wobei die geplante Forschungsinfrastruktur DeepStor als Fallstudie im Mittelpunkt steht. Darüber hinaus werden mögliche Gefährdungen wie Hebungen und Senkungen an der Oberfläche sowie induzierte Seismizität bewertet, um Erkenntnisse für die praktische Umsetzung von HT-ATES-Systemen als wichtiger Baustein der Energiewende zu gewinnen.

Die **erste Studie** (Kapitel 3) quanitfiziert die Eignung von erschöpften Erdöllagerstätten im ORG für HT-ATES-Systeme. Auf Basis der Erfassung und Analyse vorhanderen petrophysikalischer und geologischer Daten wird ein thermohy-

draulisches numerisches Modell entwickelt, um das Speicherpotenzial dieser Lagerstätten zu ermitteln. Aus den Simulationen ergeben sich Speicherkapazitäten von bis zu 10 GWh, wobei unter saisonalen Betriebszyklen bis zu 80 % der gespeicherten Energie wiedergewonnen werden kann. Die Ergebnisse verdeutlichen außerdem den signifikanten Einfluss von Reservoirmächtigkeit, Injektions- und Produktionsfließraten sowie der Bohrlochgeometrie auf die Speicherkapazität. Die Studie kommt zu dem Schluss, dass etwas 80 % der untersuchten Erdöllagerstätten im ORG als HT-ATES-Systeme genutzt werden können.

Die **zweite Studie** (Kapitel 4) untersucht die Auswirkungen der durch HT-ATES-Operationen hervorgerufenen Spannungsänderungen im Reservoir und deren möglicher Einfluss auf Hebungen und Senkungen an der Erdoberfläche. Zu diesem Zweck wird ein vereinfachtes, gekoppeltes thermohydraulisch-mechanisches (THM) numerisches Modell entwickelt, welches ein durchschnittliches Ölfeld im ORG repräsentiert. Die Ergebnisse dieser Studie zeiegen, dass Spannungsänderungen und Verformungen im Reservoir in erster Linie von der Thermoelastizität angetrieben werden (90 % der gesamten Verschiebungen), während Hebungen und Senkungen an der Erdoberfläche primär von der Poroelastizität bestimmt werden. Darüber hinaus wird gezeigt, dass die Bewegungen an der Erdoberfläche im Vergleich zum Reservoir deutlich abgeschwächt sind, was zu vernachlässigen Hebungen und Senkungen im sub-mm-Bereich führt. Im Gegensatz zu anderen Formen der Untergrundnutzung zeigt die Studie, dass der zyklische Betrieb von HT-ATES-Systemen nicht zu signifikanten kumulativen Hebungen und Senkungen an der Erdoberfläche führt. Eine Sensitivitätsanalyse identifiziert die Reservoirtiefe, den Elastizitätsmodul sowie die Injektions- und Produktionsfließraten als diejenigen Parameter, welche die Hebungen und Senkungen an der Erdoberfläche maßgeblich steuern.

Die **dritte Studie** (Kapitel 5) bewertet das potentielle Risiko einer Reaktivierung von Störungen bzw. damit verbunderer induzierter Seismizität im Zusammenhang mit dem Betrieb der geplanten HT-ATES Forschungsinfrastruktur DeepStor. Im Gegensatz zu dem vereinfachten THM-Modell der zweiten Studie wird ein detailliertes thermohydraulisches numerisches Modell des DeepStor-Reservoirs, welches auf seismischen 3D-Daten basiert, mit semi-analytischen Spannungsberechnungen entlang einer Störung in der Nähe der geplanten Bohrlochdoublette kombiniert. Die Simulationsergebnisse deuten auf ein relativ geringes Risiko für eine Reaktivierung der Störung und damit verbundener induzierter Seismizität hin, was zum Teil auf die mechanisch stabilisierende Wirkung der Heißwasserinjektion zurückzuführen ist. In der Studie werden Spannungsgradienten, der Winkel zwischen der Orientierung des Spannungsfeldes und dem Streichen der Störung sowie Betriebsparameter wie Injektions-/Produktionsfließraten und der Abstand zwischen der Bohrungsdoublette und der Störung als die sensitivsten Faktoren identifiziert, welche das Versagen der

Störung beeinflussen. Zudem wird betont, dass die identifizierten Risiken durch die Berücksichtigung der betrieblichen und geologischen Rahmenbedingungen wirksam gemindert werden können.

In dieser Arbeit wird die generelle Eignung von erschöpften Kohlenwasserstoffreservoiren im ORG für die Nutzung als HT-ATES-Systeme beschieden. Darüber hinaus zeigen die durchgeführten Studien, dass nur minimale Risiken durch Hebungen und Senkungen an der Erdoberfläche sowie durch induzierte Seismizität zu erwarten sind. Um den sicheren Betrieb von HT-ATES-Systemen zu gewährleisten, ist es jedoch unerlässlich, eine Strategie zu entwickeln, welche Risiken durch folgende Maßnahmen reduziert: (i) die Einhaltung eines ausreichenden Abstands zwischen der Bohrlochdoublette und nahe gelegenen Störungen, um die Wahrscheinlichkeit induzierter Seismizität zu minimieren, (ii) die sorgfältige Auswahl von Injektions-/Produktionsfließraten, die auf die Transmissivität des Reservoirs abgestimmt sind und dadurch die Auswirkungen auf Hebungen/Senkungen an der Erdoberfläche und induzierte Seismizität regulieren und (iii) die Berücksichtigung ausreichend tiefer Reservoirformationen, um die Auswirkungen auf Hebungen und Senkungen an der Erdoberfläche zu verringern.

CONTENTS

LIST OF FIGURES

LIST OF TABLES

ACRONYMS

ABBREVIATIONS

ATES	aquifer thermal energy storage
BC	bondary condition
BTES	borehole thermal energy storage
CCS	carbon capture and storage
CS	Coulomb stress
CTES	cavern thermal energy storage
CW	cold well
GHG	greenhouse gas
GNSS	global navigation satellite systems
HC	hydrocarbons
HW	hot well
HT-ATES	high-temperature aquifer thermal energy storage
IC	initial condition
InSAR	interferometric satellite radar
IPCC	Intergovernmental Panel on Climate Change
MOOSE	Multiphysics Object-Oriented Simulation Environment
ORG	Oberrheingraben
OWC	oil-water-contact
REV	representative elementary volume
ROS	residual oil saturation
TH	thermo-hydraulic
TIGER	THC sImulator for GEoscientific Research
THM	thermo-hydraulic-mechanical

URG	Upper Rhine Graben
UTES	underground thermal energy storage

LATIN VARIABLES

A	area
c_h	bulk hydraulic storage capacity of the porous rock
$\boldsymbol{C}$	elastic stiffness tensor
e	density of the total flux of E'
E	Young's modulus
E'	extensive quantity
$\boldsymbol{F}$	(body) force
$\boldsymbol{g}$	gravitational acceleration
G	Second Lamé coefficient
$\boldsymbol{I}$	identity matrix
$\boldsymbol{k}$	permeability
K	bulk modulus
K_b	drained bulk modulus of the rock
K_s	bulk modulus of the rock's individual solid grains
l	rupture length
L	length
M_L	seismic magnitude
M_0	seismic moment
$M0_m$	seismic moment density
$\boldsymbol{n}$	normal vector
p	pressure
P_p	pore pressure
$\boldsymbol{p}(\boldsymbol{x};\boldsymbol{n})$	traction vector

$\boldsymbol{q}$	Darcy velocity
Q	source/sink term for injection and production
S_m	mixture-specific storage coefficient of the medium
S_0	cohesion
t	time
T	temperature
T_s	slip tendency
$\boldsymbol{u}$	displacement
$\boldsymbol{v}$	advective fluid velocity
$\boldsymbol{V}$	fluid velocity
$\boldsymbol{V}^{\boldsymbol{E'}}$	velocity of the E'-continuum
v_f	fluid flux
x	arbitrary point
z	depth

GREEK VARIABLES

α	Biot parameter
α_T	coefficient of linear thermal expansion
β	orientation of the resulting failure plane to the maximum effective principle stress
β_d	volumetric drained thermal expansion coefficient
δ_{ij}	Kronecker delta
$\Delta\sigma$	average excess Coulomb stress
ε	strain
ε_v	volumetric strain
$\boldsymbol{\lambda}$	thermal conductivity
λ	First Lamé coefficient

μ'	fluid dynamic viscosity
μ	coefficient of internal friction
ν	Poisson's ratio
ρc_p	heat capacity
$(\rho c_p)_f$	heat capacity of the fluid
ρ_f	fluid density
ρ_s	solid rock density
ρ_0	reference density
$\rho\Gamma^{E'}$	source of E'
$\boldsymbol{\sigma}$	stress
σ_{ii}	normal stress component
σ_m	mean stress
σ_1	largest principal stress
σ_2	medium principal stress
σ_3	smallest principal stress
$\boldsymbol{\sigma'}$	effective stress
τ_{ij}	shear stress component
ϕ	porosity
ϕ'	angle of internal friction

1

INTRODUCTION

1.1 MOTIVATION

Unequivocally, human greenhouse gas (GHG) emissions are the driving force behind global warming, with anthropogenic CO_2 emissions as the strongest contributor. The Intergovernmental Panel on Climate Change (IPCC) affirmed that global surface temperatures surpassed 1.1 °C above the pre-industrial reference period of 1850-1900 during the 2011-2020 decade (IPCC, 2023). This rise in global temperatures affected various weather and climate extremes, including heatwaves, heavy precipitation events, and droughts across the globe. Furthermore, human-caused climate change amplifies the adverse impacts on water resources, agricultural productivity, human health and well-being, and built infrastructure. Current IPCC projections indicate a global warming range between 1.4 °C to 4.4 °C for the period 2081-2100. Limiting global warming to the 1.5 °C goal necessitates a very low GHG emissions scenario that includes substantial negative emissions during the latter half of the century (Figure 1.1).

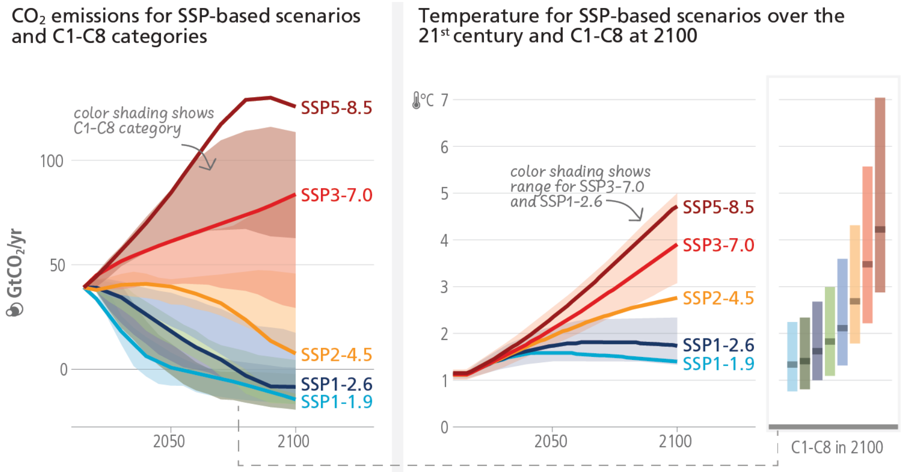

Figure 1.1: CO_2 emission trajectories (left) and global surface temperature responses (right) for five different GHG emission scenarios (SSPx-y), categorized into eight global mean temperature change ranges (C1-C8). Adapted from IPCC (2023).

Addressing global warming necessitates a rapid and far-reaching reduction in GHG emissions across all sectors, departing sharply from current trends and surpassing the scope of existing and planned policies. This unequivocal requirement demands a significant decrease in overall fossil fuel consumption and a substantial increase in the usage of low-emission (e.g. renewable) energy sources (IPCC, 2022). For instance, such measures would involve supplying 70-85 % of the world's electricity from renewable sources by 2050 and implementing large-scale carbon capture and storage (CCS) technologies in the latter half of this century (Tollefson, 2018).

In recent years, the transition to a decarbonized society led to a continuous increase in the share of renewable energies (particularly wind and solar power, but also e.g. geothermal). In 2021 alone, more than 314 GW of global renewable power capacity was added, representing a market growth of 11 % (IEA, 2023; REN21, 2022). However, the temporal availability of most renewable energy sources, particularly wind and solar power, is inherently constrained by climatic and weather conditions. This seasonal mismatch between peak energy demand in winter (primarily for residential and commercial heating) and the highest renewable supply in summer poses a significant challenge (Dinçer and Rosen, 2011; IEA, 2023). Addressing this seasonal mismatch requires the implementation of large-scale energy storage systems. Given the physical limitations of above-ground storage, the subsurface emerges as the most viable option for accommodating these systems (Lee, 2013; Li, 2016).

Among various subsurface energy storage technologies, including borehole or cavern thermal energy storage, aquifer thermal energy storage (ATES) systems are frequently employed for low-temperature storage applications such as residential or greenhouse heating (Yang et al., 2021). However, to extend the applicability of ATES systems beyond residential or greenhouse heating, encompassing industrial needs or providing heat for district heating networks, higher temperatures of up to 150 °C and corresponding storage capacities are essential. Such high-temperature (HT)-ATES systems, usually operating in deeper reservoirs, offer an advantage over conventional low-temperature ATES systems by minimizing conflicts with groundwater utilization (Wesselink et al., 2018). Nevertheless, only a limited number of HT-ATES systems are currently operational, such as in Rostock in northeastern Germany (Bauer et al., 2010), or were successfully operated in the last decades (e.g. in Berlin and Neubrandenburg; Fleuchaus et al., 2021; Holstenkamp et al., 2017). Research on HT-ATES is actively being conducted in various pilot and demonstration projects in Germany, the Netherlands, and Switzerland (Bremer et al., 2022; Oerlemans et al., 2022).

As part of one of these projects, in the DeepStor project near Karlsruhe in the Upper Rhine Graben (URG) in southwestern Germany, the feasibility of HT-ATES utilizing a depleted oil reservoir is being investigated (Bremer et al., 2022). The URG, a 300 km long, NNE-SSW-trending continental rift system, has accumulated up to 3.5 km of Cenozoic sediments since the onset of the graben formation 47 Ma ago (Geyer et al., 2011). These Cenozoic sediments are strongly influenced by fault-controlled convective flow within the underlying Mesozoic sediments and the crystalline basement (Bächler et al., 2003; Baillieux et al., 2013). This results in significantly elevated geothermal gradients ranging from 35 K km^{-1} to 58 K km^{-1}, locally reaching up to 100 K km^{-1}, creating exceptionally favorable conditions for geothermal utilization (Bresee, 1992; Maurer et al., 2020).

The extensive history of hydrocarbon (Reinhold et al., 2016; Rinck, 1987; Schnaebelé, 1948) and geothermal Frey.2022 exploration and exploitation, make the URG one of the geoscientifically most extensively investigated continental rift systems worldwide (Böcker et al., 2017; Grimmer et al., 2017). As a result, the numerous depleted oil fields in the URG are exceptionally well characterized, with detailed knowledge of their depth, geometry, and favorable petrophysical reservoir properties (Böcker, 2015; Bruss, 2000; Grandarovski, 1971). This provides a comprehensive data basis for evaluating their suitability for HT-ATES operations. Furthermore, these depleted oil fields are situated in proximity to potential heat sources for storage (e.g. excess heat from geothermal power plants or solar energy during summer, along with industrial waste heat) and are located within a densely populated area with high heat demand. In conclusion, depleted oil reservoirs in the URG may be ideally suited for HT-ATES operations. This high potential may extend to comparable hydrocarbon provinces, such as the Geneva basin in Switzerland (Moscariello, 2019), and clastic reservoirs in the Netherlands (van Wees et al., 2017), where similar close links between hydrocarbon and geothermal activities have been observed.

Any utilization of the subsurface, particularly the extraction of fossil fuels like coal, oil, and gas, is inherently associated with various hazards that can impact human populations or the environment. These hazards notably include subsidence (Gambolati et al., 2005; Holzer and Galloway, 2005), induced seismicity (Buijze et al., 2019; Doglioni, 2018; van der Baan and Calixto, 2017), and water pollution (Zhang et al., 2019; van der Gun et al., 2016). As our society transitions towards renewable energy sources, other forms of subsurface utilization (e.g. CCS, various forms of energy storage, geothermal energy, but also nuclear waste disposal) will grow in importance (REN21, 2022) and their associated hazards must be considered. In contrast to hydrocarbon production (Suckale, 2009; Van Thienen-Visser and Fokker, 2017), geothermal energy (Békési et al., 2019; Buijze et al., 2019), and CCS (Rutqvist et al., 2016; Vilarrasa et al., 2019), there is a lack of research quantifying the risk of HT-ATES systems, particularly in terms of induced seismicity or surface movements. Unlike other forms of subsurface utilization, HT-ATES typically involves increasing rather than decreasing temperatures (Wesselink et al., 2018), generating smaller pressure perturbations (Birdsell et al., 2021), and targeting shallower sedimentary aquifers instead of fault systems (Fleuchaus et al., 2020). Subsequently, it becomes evident that specific risk assessments are required to account for the unique characteristics and operational framework of HT-ATES systems compared to other well-studied forms of subsurface utilization.

1.2 STRUCTURE OF THE THESIS

The urgent challenges of human-induced climate change and the necessary transition to low-emission (e.g. renewable) energy sources underscore the significance of large-scale energy storage, including heat storage in the subsurface. Currently, subsurface heat storage systems (e.g. ATES) are predominantly employed for low-temperature applications, such as residential or greenhouse heating, leaving a large unused potential for high-temperature storage systems to supply heat for industrial needs or district heating networks untapped. Consequently, this thesis is motivated by the need to evaluate the potential role of HT-ATES within the future energy landscape, particularly in the context of abundant depleted hydrocarbon reservoirs.

In this thesis, I aim to address the following key questions: 1) Are depleted hydrocarbon reservoirs, with the URG serving as a case study, suitable for conversion into HT-ATES systems? If so, what subsurface and operational parameters determine their suitability? 2) What is the geomechanical impact of HT-ATES operations on the stress distribution around the wells in the subsurface? To what extent do the induced storage-related displacements result in uplift or subsidence at the ground surface? 3) Can the stress changes in the subsurface pose a risk of reactivation of nearby faults, potentially leading to induced seismicity? These questions will be addressed by employing sophisticated coupled thermo-hydraulic and thermo-hydraulic-mechanical simulations, complemented by semi-analytical calculations.

Chapter 2 lays out a strategic vision for how seasonal HT-ATES in e.g. depleted hydrocarbon reservoirs can complement conventional geothermal operations, enabling them to not only meet base load heat demand but also cover peak demand in winter. It also introduces the general concept of "push-pull" heat storage, typically implemented using a well doublet with separate hot and cold legs, and describes the challenges associated with HT-ATES systems. Additionally, the fundamental equations governing thermal, hydraulic, and (geo-)mechanical processes, forming the foundation for the numerical simulations in this thesis, are presented.

Chapter 3 presents the first study in this thesis, investigating the suitability of depleted oil reservoirs in the URG for HT-ATES applications. It compiles and evaluates available petrophysical and geological data from depleted and operational hydrocarbon reservoirs in the URG. Based on this comprehensive data analysis, a simplified thermo-hydraulic model is employed to numerically assess the heat storage potential of these reservoirs. To investigate the influence of various reservoir and operational parameters, as well as two well geometries (vertical and horizontal), a parameter sensitivity analysis is performed.

Chapter 4 focuses on assessing the impact of stress changes in the reservoir induced by HT-ATES operations on ground surface deformation. In this second study, a simplified thermo-hydraulic-mechanical (THM) model of the proposed DeepStor demonstrator, based on the data compilation presented in Chapter 3, is employed. In this study, I aim to address two primary objectives: 1) To elucidate the relative contributions of poroelastic and thermoelastic stress changes to reservoir deformation and ground surface movements. 2) To determine the likelihood of surface uplift and identify the most sensitive parameters.

In Chapter 5, the main focus is set to the assessment of the risk of fault reactivation and induced seismicity associated with HT-ATES operations. Unlike the previous study, I did not employ a fully coupled THM model; instead, stress changes on a specific fault plane were calculated following a semi-analytical approach based on the results of thermo-hydraulic numerical simulations. Furthermore, the previously used synthetic simplified model of an HT-ATES system was replaced by a subsurface model of the planned HT-ATES demonstrator DeepStor.

Two approaches are employed to assess this risk, both incorporating a Monte Carlo analysis to account for uncertainties in various reservoir and operational parameters: 1) Assuming an unstressed fault, the risks were evaluated based on the slip tendency distribution at the fault of interest. 2) Assuming a nearly critically stressed fault, the sensitivity of Coulomb stress changes at the fault, which could potentially lead to failure, was assessed.

2

GEOTHERMAL HEAT STORAGE AND ITS FUNDAMENTAL PROCESSES

2.1 STRATEGIC VISION FOR GEOTHERMAL HEAT

Heating and cooling account for a substantial portion of the final energy consumption, representing around 59 % in Germany in 2021. This comprises 28.5 % for heating and cooling of buildings, 5.5 % for warm water provision, and 25 % for heating and cooling in industrial processes (AGEB, 2022). This translates to approximately 40 % of Germany's CO_2 emissions, the highest individual share among all energy sectors (BDEW, 2021). The high proportion of CO_2 emissions associated with heating and cooling can be attributed to the significantly lower share of renewable heating and cooling sources (17.4 %) compared to renewable electricity, where approximately 46 % are provided by renewables, primarily biomass, wind, and solar (Umweltbundesamt, 2023). This issue is not unique to Germany; globally, the renewable supply of heating lags behind that of renewable electricity (11.2 % vs. 28.0 %; IEA, 2023).

Further complicating the challenges of utilizing renewable energy for heating and cooling is the seasonal mismatch between peak demand in winter (particularly for residential heating) and the maximum renewable energy supply during summer (Dinçer and Rosen, 2011). Unlike other renewable energy sources (particularly solar and wind), geothermal energy can effectively meet the base load of heating (and cooling) demand without substantial seasonal fluctuations (Agemar et al., 2014). However, this leaves the peak demand for heating and cooling to be met by other energy sources, currently predominantly fossil fuels, such as coal, gas, and oil boilers installed individually in residential or commercial buildings (European Commission, 2016). Seasonal heat storage represents a key technology to address this mismatch (Lee, 2013; Li, 2016). This particularly applies to high-temperature heat storage, which can complement the heat supply from conventional geothermal by storing excess heat in the subsurface in summer (when supply exceeds demand) and then producing it during winter (when demand exceeds supply; Wesselink et al., 2018)

2.2 UNDERGROUND THERMAL ENERGY STORAGE

2.2.1 *Overview*

Thermal energy storage encompasses various forms, each employing distinct mechanisms to store and retrieve heat: 1) Sensible heat storage relies on the temperature change of a liquid (e.g. water or oil-based fluids) or solid (e.g. rocks or metals) medium, absorbing heat by increasing temperature and releasing it by decreasing temperature. 2) Latent heat storage exploits the latent heat of phase changes, storing and releasing heat as substances undergo phase transitions, such as the melting of salt hydrates or paraffins (Hasnain, 1998). 3) Thermochemical reactions, harnessing the enthalpy of chemical reactions, store thermal energy by breaking down a compound into its components using heat and releasing it when the reaction is reversed (Lee, 2013).

Underground thermal energy storage (UTES) represents a sub-type of sensible heat storage, commonly employed for storing large quantities of heat. Aquifer thermal energy storage (ATES) systems utilize saturated and permeable aquifers to store heated water, offering the greatest storage capacity and long-term applicability of all UTES technologies (Dinçer and Rosen, 2011). Borehole thermal energy storage (BTES) systems operate on a closed-loop principle, exchanging heat between a network of borehole heat exchangers (BHEs) and the surrounding rocks or sediments (Skarphagen et al., 2019). Cavern thermal energy storage (CTES) involves storing heated water in large, open underground caverns, either natural or man-made. Similarly, artificial water tanks and pit storage systems can be constructed underground or near the surface for heat storage purposes (Lee, 2013).

2.2.2 *Principles of "push-pull" ATES*

As this thesis focuses on the viability of high-temperature ATES systems and a geomechanical risk assessment thereof, the operating principle of "push-pull" ATES is outlined in the following. ATES systems harness the temperature difference between the subsurface (unaffected by seasonal surface temperatures) and the surface to provide cooling (summer) and heating (winter) services (Dickinson et al., 2009). A well doublet is the most commonly used arrangement: excess heat is injected as water into the warm well in summer ("push") and extracted in winter ("pull"), while a cold well serves for cooling purposes, with the process reversed (Kim et al., 2010; Stricker et al., 2020). Separate storage of heated and cooled water near the respective wells eliminates thermal interaction, minimizing efficiency losses (Gholami Korzani et al., 2020; Sommer et al., 2015). However, single-well (Jeon et al., 2015) or multiple-well (Sommer et al., 2015) configurations are also employed, albeit less frequently than well doublets. ATES systems are typically operated seasonally, and occasional rest periods without injection or production may be incorporated into the operating schedule to accommodate periods of reduced heating or cooling demand (Kim et al., 2010).

2.2.3 *ATES applications*

ATES systems are versatile and adaptable to various applications, ranging from direct cooling to direct and indirect heating as well as hybrid systems, depending on specific climatic conditions and end-user requirements (Andersson et al., 2003; Andersson, 2007; Lee, 2013). For indirect heating (when subsurface temperatures fall short of demand), supplementary thermal energy needs to be supplied by external sources such as cogeneration waste heat or renewable energy sources (Fleuchaus et al., 2018). As of 2018, over 2800 systems were operational globally, predominantly in the Netherlands and in Sweden (ca. 85 %), along with notable deployments in Denmark and Belgium. 99 % of these ATES systems operate with storage temperatures of < 25 °C. They provided over 2.5 TWh of heating and cooling annually, equivalent to the average thermal energy consumption of 150,000 households in Central Europe (Fleuchaus et al., 2018). In the Netherlands, a significant majority (approximately 70 %) of ATES systems supply thermal energy for public and commercial buildings, while the remaining 30 % are utilized for private housing and low-temperature industrial applications (Nordell et al., 2015). More recently, the heating and cooling of greenhouses has emerged as a promising application for ATES (Paksoy and Beyhan, 2015; Turgut et al., 2009).

2.2.4 *High-temperature ATES: benefits and challenges*

Over the past few decades, several pilot projects were developed to investigate the feasibility of high-temperature (HT)-ATES systems at greater depths compared to shallow systems, aiming at broadening the applicability of ATES systems beyond residential or greenhouse heating. Higher storage temperatures and corresponding capacities are envisaged in the context of providing heat for industrial processes or district heating networks (Wesselink et al., 2018). This means that usually external (excess) energy is stored in HT-ATES systems, rather than using the building energy itself. Furthermore, HT-ATES systems offer the advantage of higher extraction temperatures compared to conventional ATES systems, enabling direct heating without the need for auxiliary heat pumps (Drijver et al., 2012). This opens up complementary operations with deep geothermal systems. By storing surplus heat in summer, HT-ATES could mitigate the reliance on expensive fossil-fuel-based heating during winter (Réveillère et al., 2013).

Despite their potential, several challenges have hampered the widespread adoption of HT-ATES systems. Currently, only one operational system exists worldwide in Rostock, Germany (Bauer et al., 2010), alongside a few ongoing research and operational pilot projects, e.g. in Middenmeer, the Netherlands (Oerlemans et al., 2022). Fleuchaus et al. (2020) identify the major risks associated with HT-ATES operations, including not only technical and financial considerations but also social, political, and legal aspects. Notably, the most prominent technical risks involve well scaling and clogging, as well as uncertainties in the energy supply and demand.

For example, Nitschke et al. (2023) assessed the potential for mineral precipitation and dissolution in the planned DeepStor demonstrator, specifically focusing on the impact of temperature changes and the associated perturbations of the chemical equilibrium. The study highlights the need for site-specific investigations due to the large variations in the composition of HT-ATES brines and their influence on system operation. Furthermore, Fleuchaus et al. (2020) point out that many HT-ATES operations have been terminated due to either overestimating heating demand or losing their heat source, underlining the need for holistic energy concepts.

2.3 HYDRAULIC PROCESSES AND HEAT TRANSPORT

Throughout this thesis, the impact of thermo-hydraulic-mechanical processes associated with high-temperature heat storage is investigated. In this and the subsequent section, the underlying physics of fluid flow through a porous medium and the interaction with the solid are described. A comprehensive derivation of the relevant equations exceeds the scope of this thesis but is well-documented in textbooks, such as Bear and Cheng (2010) for hydraulic processes in porous media, Carslaw and Jaeger (1959) for heat transport, or Jaeger et al. (2007) for rock mechanics. Consequently, in the following, I limit the description of the governing equations to the processes that are important for this thesis.

2.3.1 *Hydraulic processes*

Fluid flow is governed by the principle of mass and momentum balance. For any extensive quantity, E', mass balance describes the balance between the quantity of E' accumulating within the specified spatial domain as well as the net quantity of E' entering the domain and the net production (source/sink) of E' within the domain. Expressing the E'-flux as the sum of advective and diffusive fluxes, the mass balance equation can be written in the form (Bear and Cheng, 2010):

$$\frac{\partial e}{\partial t} = -\nabla \cdot e\boldsymbol{V}^{\boldsymbol{E'}} + \rho \Gamma^{E'} \tag{2.1}$$

t is the time, e the density of the total flux of E', $\boldsymbol{V}^{E'}$ the velocity of the E'-continuum, and $\rho\Gamma^{E'}$ the source of E'.

Mass balance on the macroscopic level (i.e. fluid flow in a porous medium) can be derived by averaging the mass balance equation on the microscopic level over a representative elementary volume (REV), which consists of averaged material properties that correspond to pore-scale quantities of the entire domain of interest. Under the assumption that the dispersive mass flux is much smaller than the advective one (as well as the absence of diffusive flux), the macroscopic mass balance equation for a fluid phase can be written as:

$$S_m \frac{\partial p}{\partial t} = -\nabla \cdot \boldsymbol{q} + Q \tag{2.2}$$

S_m is the mixture-specific storage coefficient of the medium, p is the pressure, $\boldsymbol{q}$ is the Darcy velocity, and Q is the source/sink term for injection and production.

Similarly, as for mass balance, the momentum balance can also be derived from the respective equation on the microscopic level, the differential balance equation of linear momentum, which describes the rate of accumulation of momentum as the sum of the rate of momentum gained by advection and diffusion, as well as the rate of supply of momentum by the body force, typically gravity (Bear and Cheng, 2010).

$$\frac{\partial}{\partial t} \rho_f \boldsymbol{V} = -\nabla \cdot \rho_f \boldsymbol{V}\boldsymbol{V} + \nabla \cdot \boldsymbol{\sigma} + \rho_f \boldsymbol{F} \tag{2.3}$$

ρ_f is the fluid density, $\boldsymbol{V}$ the fluid velocity, $\boldsymbol{\sigma}$ the stress, and $\boldsymbol{F}$ the body force.

Under the assumptions of a Newtonian fluid, negligible inertial forces compared to viscous ones, as well as negligible momentum transfer within the fluid compared to the drag produced at the fluid-solid interface, the momentum balance can be averaged over a REV, resulting in a simplified form, the well-known Darcy's law:

$$\mathbf{q} = \frac{\boldsymbol{k}}{\mu}(-\nabla p + \rho_f \boldsymbol{g}) \tag{2.4}$$

$\boldsymbol{k}$ is the permeability tensor, μ is the fluid dynamic viscosity, and $\boldsymbol{g}$ is the gravitational acceleration.

2.3.2 *Transport processes*

In the following, the underlying processes for the transport of a medium, such as heat or solutes, in the subsurface are described. Heat transport in porous media is influenced by several processes and can be described as analogous to the transport of particles: On the one hand, heat is transported by groundwater flow (advection), and on the other hand by conduction in the solid and liquid medium. As the groundwater flow velocity can be heterogeneous, additionally thermal dispersion effects can occur. However, these effects are usually not taken into account due to their negligible effect compared to advection and conduction. (Marsily, 1993). Based on Fourier's law, conductive heat transport can be written in the form of the energy conservation equation (Carslaw and Jaeger, 1959)):

$$\frac{\partial T}{\partial t} = \frac{\boldsymbol{\lambda}}{\rho c_p} \nabla^2 T \tag{2.5}$$

T is the temperature, $\boldsymbol{\lambda}$ and ρc_p are the thermal conductivity and the heat capacity of the medium, respectively.

This equation can be extended to also take advective heat transport into account, with the Darcy velocity, $\boldsymbol{q}$, realizing the coupling to the pressure field. Under the additional assumption of local thermal equilibrium between the solid and the fluid phase, as well as neglecting the dissipation of mechanical energy due to the deformation of the solid phase, the thermal transport equation, which describes energy balance, can be expressed as follows (Gholami Korzani et al., 2020; Kohl and Hopkirk, 1995):

$$\rho c_p \frac{\partial T}{\partial t} - \boldsymbol{\lambda} \nabla^2 T + (\rho c_p)_f \boldsymbol{q} \nabla T = Q \tag{2.6}$$

$(\rho c_p)_f$ represents the heat capacity of the fluid. Both heat capacity and thermal conductivity are assumed to be equivalent to the mean value of each phase weighted by the respective volumetric fraction:

$$\rho c_p = \phi (\rho c_p)_f + (1 - \phi)(\rho c_p)_s \tag{2.7}$$

$$\boldsymbol{\lambda} = \phi \boldsymbol{\lambda}_f + (1 - \phi) \boldsymbol{\lambda}_s \tag{2.8}$$

where ϕ represents the porosity, and the subscripts f and s represent the fluid and solid phase, respectively.

2.4 GEOMECHANICAL PROCESSES

In the following section, a brief introduction to geomechanical processes in the earth's crust is given, focusing on elastic rock deformation. A comprehensive understanding of geomechanics is important for both engineers, dealing with applications, such as avoiding fault reactivation close to dams or in the vicinity of geothermal activities, as well as geoscientists, who want to understand natural phenomena, such as mountain building or the evolution of sedimentary basins (Cornet, 2015). Herein, scales vary over multiple magnitudes, both for time and space. Hence, geomechanical problems cover processes varying from e.g. small-scale instabilities around boreholes induced by drilling, taking place over seconds to hours (Stricker et al., 2023) to geomechanical questions related to nuclear waste storage, where storage security needs to be guaranteed over up to a million years (Gens et al., 2009), or subsidence caused by hydrocarbon production, where reservoir compaction impacts the ground surface up to several kilometers above the reservoir (Gambolati et al., 2005; Holzer and Galloway, 2005). The following introduction mainly follows the work of Cornet (2015), Guéguen and Palciauskas (1994), Jaeger et al. (2007) and Zoback (2007).

2.4.1 *Basic definitions*

Stress in the lithosphere is defined by the forces acting upon and within it. Generally, the traction vector, $\boldsymbol{p(x;n)}$, describes the influence of a force, $\boldsymbol{F}$, on an arbitrary point, x, on a plane with the area, A (Jaeger et al., 2007):

$$\boldsymbol{p(x;n)} = \lim_{dA \to 0} \frac{\boldsymbol{dF}}{dA} \tag{2.9}$$

where $\boldsymbol{n}$ represents the vector normal to the plane.

The stress tensor combines the traction vectors of all three directions into a second-order tensor σ_{ij}, consisting of 9 components with i,j = 1,2,3. It describes the density of forces that act on all surfaces through a given point and is given for a homogeneous, isotropic body by the following (Zoback, 2007):

$$\boldsymbol{\sigma} = \begin{pmatrix} \sigma_{xx} & \tau_{xy} & \tau_{xz} \\ \tau_{xy} & \sigma_{yy} & \tau_{yz} \\ \tau_{xz} & \tau_{yz} & \sigma_{zz} \end{pmatrix} \tag{2.10}$$

The indices of the individual components denote the direction of the acting force, $\boldsymbol{F}$, and the surface upon which the stress component acts, respectively. The diagonal entries of the stress tensor are called normal stresses σ_{ii}, which act in the direction of the plane normal. All other entries describe shear stresses τ_{ij}, acting parallel to the respective surface (Figure 2.1). The stress tensor is symmetric due to equilibrium conditions, thus $\tau_{ij} = \tau_{ji}$. Compressive stresses are defined as positive values as in situ stresses in depths relevant to geomechanical problems are always compressive.

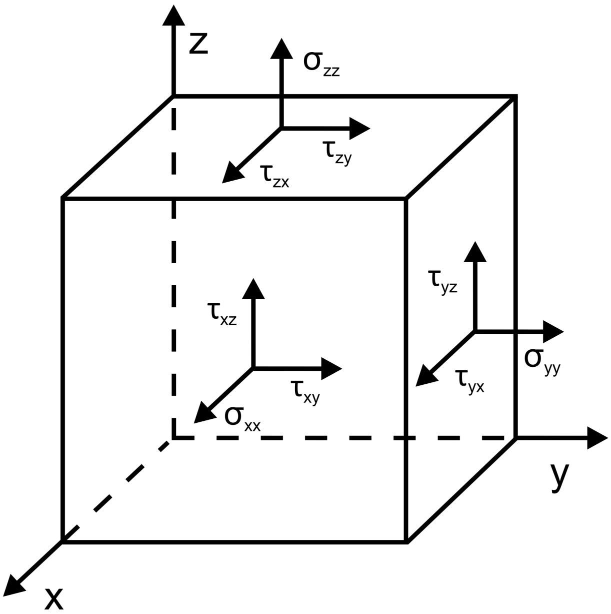

Figure 2.1: The stress tensor components acting on the volume planes.

Tensor transformation allows the calculation of stresses for any coordinate system. By calculating the eigenvalues of the stress tensor, it can be further simplified to represent the stress state in the principal coordinate system (parallel to x, y, and z in Figure 2.1), in which the so-called principal stresses $\sigma_1 > \sigma_2 > \sigma_3$ fully describe the stress field without any shear components:

$$\boldsymbol{\sigma} = \begin{pmatrix} \sigma_1 & 0 & 0 \\ 0 & \sigma_2 & 0 \\ 0 & 0 & \sigma_3 \end{pmatrix} \tag{2.11}$$

2.4.2 *Linear elasticity*

Stress changes lead to a displacement field, $\boldsymbol{u}$, which can be described by the second-order strain tensor (Zoback, 2007):

$$\varepsilon_{ij} = \frac{1}{2}\left(\frac{\partial u_i}{\partial x_j} + \frac{\partial u_j}{\partial x_i}\right) \tag{2.12}$$

The basic assumption of linear elasticity is that deformations are proportional to stresses and reversible. The relationship between the stress tensor $\boldsymbol{\sigma}$ and the strain tensor $\boldsymbol{\varepsilon}$ is then given by Hooke's law, where $\boldsymbol{C}$ is the elastic stiffness tensor (Guéguen and Palciauskas, 1994):

$$\sigma_{ij} = C_{ijkl}\varepsilon_{kl} \tag{2.13}$$

Assuming that a rock matrix can be described by an isotropic medium, Hooke's law can be expressed in a simplified form (Cornet, 2015):

$$\sigma_{ij} = \lambda \varepsilon_v \delta_{ij} + 2G\varepsilon_{ij} \tag{2.14}$$

where δ_{ij} represents the Kronecker delta, ε_v the volumetric strain, as well as λ and G are the first and second Lamé coefficients. G is also called the shear modulus. By computing the mean stress, σ_m, the bulk modulus, K, can be defined as the proportional constant between the volumetric strain and the mean stress (Jaeger et al., 2007):

$$\sigma_m = (\sigma_1 + \sigma_2 + \sigma_3)/3 = \left(\lambda + \frac{2}{3}G\right) \varepsilon_v \tag{2.15}$$

$$K = \lambda + \frac{2}{3}G \tag{2.16}$$

The inverse of the bulk modulus, $1/K$, is called bulk compressibility. The two further elastic parameters are Young's modulus, E, and Poisson's ratio, ν, which can be derived from the introduced elastic parameters, for instance, as follows:

$$E = \frac{9KG}{3K + G} \tag{2.17}$$

$$\nu = \frac{3K - 2G}{6K + 2G} \tag{2.18}$$

In general, only two elastic parameters are independent for an isotropic material: if two parameters are known, the other three can be determined similarly as outlined above. A full listing of the respective equations to express any three parameters of the set λ, K, G, E, ν can be found in Davis and Selvadurai (1996).

2.4.3 *Thermo-poroelastic coupling*

The subsurface, and especially geothermal reservoirs, consists of a porous medium, which is saturated with a fluid, such as a geothermal brine or hydrocarbons. The behavior of rock is described by the theory of poroelasticity, which has mainly been derived by Biot (1962). For the description of the influence of the pore pressure, P_p, on the stress state in the porous medium, the concept of the effective stress, σ'_{ij}, is introduced (Nur and Byerlee, 1971):

$$\sigma'_{ij} = \sigma_{ij} - \delta_{ij} \alpha P_p \tag{2.19}$$

where α is the Biot parameter:

$$\alpha = 1 - K_b/K_g \tag{2.20}$$

with K_b as the drained bulk modulus of the rock, and K_g the bulk modulus of the rock's individual solid grains. It becomes clear that the pore pressure only acts on the normal stress components, σ_{ii}, and not the shear stress components, τ_{ij}. Taking into account the concept of effective stresses, Equation 2.14 can be rewritten as follows (Zoback, 2007):

$$\sigma'_{ij} = \lambda \varepsilon_v \delta_{ij} + 2G\varepsilon_{ij} - \delta_{ij}\alpha P_p \tag{2.21}$$

In addition to pore pressure, thermal effects on the mechanical behavior of rock have also to be considered, especially in the context of geothermal applications. Thus, the theory of thermo-poroelasticity also takes into account the effect of temperature changes on stress and strain. Equation 2.21 can be extended as follows:

$$\sigma'_{ij} = \lambda \varepsilon_v \delta_{ij} + 2G\varepsilon_{ij} - \delta_{ij}\alpha P_p + K\alpha_T \delta_{ij}\Delta T \tag{2.22}$$

where α_T represents the coefficient of linear thermal expansion and defines the change in length, L, of a material as response to a temperature change δT:

$$\alpha_T = \frac{1}{L}\frac{\delta L}{\delta T} \tag{2.23}$$

Consequently, temperature increases lead to the expansion and temperature decreases to a contraction of a material. Similarly to the effect of poroelasticity, temperature changes only affect normal stresses.

2.4.4 *Rock failure*

The previous sections have described the elastic behavior of porous media, such as rocks in the subsurface. However, above a certain threshold (i.e. the rock strength) rocks no longer deform elastically when submitted to stresses and failure occurs (Guéguen and Palciauskas, 1994). Rock failure highly depends on rock properties and stress conditions. Hence, various failure criteria were developed for different applications, failure modes, and rock types (Fjær et al., 2008). The simplest, but still most widely used, failure criterion is the Coulomb failure criterion, which assumes failure to occur due to shear stress acting along a plane (Coulomb, 1773). Failure will occur if a certain threshold of shear stress, τ_f, is exceeded:

$$|\tau_f| = S_0 + \mu' \sigma_n \tag{2.24}$$

where S_0 represents the cohesion, μ the coefficient of internal friction, and σ_n the normal stress. The Coulomb failure criterion can be visualized in the simplified Mohr diagram with a linearized envelope, where the y-axis interception represents S_0 (Figure 2.2). The slope of the line is μ', from which the angle of internal friction, ϕ', can be derived (Jaeger et al., 2007):

$$\phi' = \tan^{-1} \mu' \tag{2.25}$$

Failure occurs for principal stresses that lead to a Mohr circle touching the envelope.

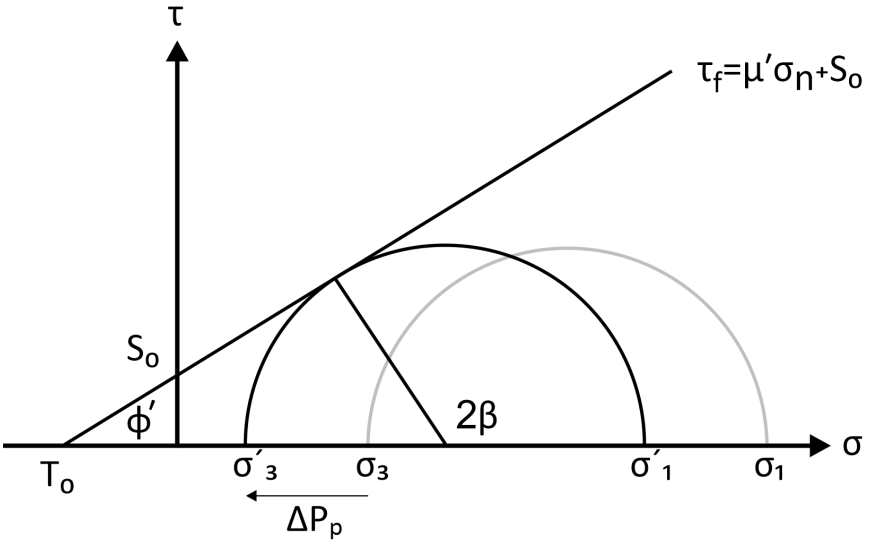

Figure 2.2: Mohr-diagram with the Coulomb failure criterion. The grey semicircle represents the initial non-critical stress state, whereas failure occurs for an increase in pore pressure, leading to the black semicircle touching the (linearized) failure envelope.

As described in Chapter 2, pore pressure leads to a reduction in the effective normal stress. Hence, an increase in pore pressure (e.g. caused by fluid injection in the subsurface) shifts the Mohr circle to the left, bringing the rock closer to failure. The orientation β of the resulting failure plane to the maximum effective principle stress, σ'_1 is given by:

$$\beta = 45 + \frac{1}{2}\phi' \tag{2.26}$$

Deformation of rocks in the subsurface typically takes place on predefined surfaces, such as fractures or faults. Under the assumption that these planes are not critically stressed before the utilization of the subsurface (e.g. hydrocarbon extraction or geothermal production), failure occurs when the slip tendency, T_s, exceeds the friction coefficient of the fault, μ' (Morris et al., 1996; Worum et al., 2004):

$$T_s = \frac{\tau}{\sigma_n'} \geqslant \mu' \tag{2.27}$$

3

THE POTENTIAL OF DEPLETED OIL RESERVOIRS FOR HIGH-TEMPERATURE STORAGE SYSTEMS

This chapter was published in Energies 2020 13(24), 6510
DOI: 10.3390/en13246510

ABSTRACT

HT-ATES (high-temperature aquifer thermal energy storage) systems are a future option to shift large amounts of high-temperature excess heat from summer to winter using the deep underground. Among others, water-bearing reservoirs in former hydrocarbon formations show favorable storage conditions for HT-ATES locations. This study characterizes these reservoirs in the Upper Rhine Graben (URG) and quantifies their heat storage potential numerically. Assuming a doublet system with seasonal injection and production cycles, injection at 140 °C in a typical 70 °C reservoir leads to an annual storage capacity of up to 12 GWh and significant recovery efficiencies increasing up to 82% after ten years of operation. Our numerical modeling-based sensitivity analysis of operational conditions identifies the specific underground conditions as well as drilling configuration (horizontal/vertical) as the most influencing parameters. With about 90% of the investigated reservoirs in the URG transferable into HT-ATES, our analyses reveal a large storage potential of these well-explored oil fields. In summary, it points to a total storage capacity in depleted oil reservoirs of approximately 10 TWh a^{-1}, which is a considerable portion of the thermal energy needs in this area.

3.1 INTRODUCTION

Continuous efforts of our society to reduce CO_2 emissions have led to a large expansion of renewable energy sources (IEA, 2017; REN21, 2019). Their industrial and domestic utilization is, however, hampered by the limited temporal availability of these energy sources, especially at times when necessary weather or daylight conditions for solar or wind energy sources are not given (Dinçer and Rosen, 2011). Furthermore, climatic conditions in most highly industrialized countries require the provision of significant amounts of thermal energy for heating purposes (IEA, 2017), leading to a seasonal mismatch between excess heat in summer and heat demand in winter. This mismatch between supply and demand of energy represents a central challenge for the integration of renewable energy sources and requires energy buffer systems of huge capacity (Lee, 2013; Li, 2016).

Geothermal energy technologies allow for energy production as well as storage. Already today, numerous storage applications exist, especially in shallow underground systems, ranging from hot water tanks and gravel pits to borehole heat exchangers (Dinçer and Rosen, 2011). Most present are BTES ("Borehole Thermal Energy Storage") systems, which are typically reversing heat pump circulation to store excess heat through borehole heat exchangers (Bär et al., 2015; Rad and Fung, 2016), and ATES ("Aquifer Thermal Energy Storage") systems, which store and recover heat using the high permeability of shallow groundwater layers (Dickinson et al., 2009; Lee, 2013). In some countries, these systems can be considered to be state-of-the-art and are used in a variety of private and public buildings. Worldwide, >2800 ATES systems are in operation, mainly in the Netherlands, providing more than 2.5 TWh a^{-1} for heating and cooling purposes (Fleuchaus et al., 2018; van Heekeren and Bakema, 2015).

However, the operational temperatures of typically T < 50 °C cover mainly individual domestic needs and ignore the industrial or district heating demand for high temperature (HT) heat storage, where temperatures up to 150 °C are required (Fraunhofer ISI, 2017; Sayegh et al., 2018). These systems – herein referred to as "HT-ATES" – offer several advantages over conventional ATES systems: (1) They are operated in deeper reservoirs not perturbing near-surface groundwater horizons, and (2) they allow for shifting large amounts of excess heat to cooler winter periods (Wesselink et al., 2018). Furthermore, they can be operated at relatively low flow rates inhibiting environmental risk (e.g., induced seismicity) and allowing them to be placed even in an urban environment (Kabus et al., 2008; Sanner and Knoblich, 2004). Worldwide, only a few HT-ATES systems are in operation. Holstenkamp et al. (2017) describe the conditions and experience of the two German systems HT-ATES in Berlin and Neubrandenburg, emphasizing the need for further research.

The Upper Rhine Graben (URG) with its generally high-temperature gradients, which can locally reach up to 100 K km^{-1}, provides one of the most favorable geothermal conditions in Central Europe (Baillieux et al., 2013) and a long-standing hydrocarbon (HC) and recent geothermal exploitation history at German, Swiss and French sites. The close link between hydrocarbon and geothermal reservoirs is manifested in (1) the vicinity of temperature anomalies and hydrocarbon reservoirs, (2) the unintended discovery of the HC reservoir Römerberg (Speyer) by geothermal exploration (Böcker, 2015; LBEG, 2009), and (3) the large areal coverage with 3D seismic hydrocarbon exploration that are now also used for geothermal exploration. A similar co-occurrence of geothermal and hydrocarbon resources is for example investigated for the Geneva Basin in Switzerland (Moscariello, 2019). The long history of hydrocarbon and geothermal exploration has led to the URG being geoscientifically the most intensively investigated continental rift system worldwide (Böcker et al., 2017; Grimmer et al., 2017). The numerous depleted oil fields in the URG are proven reservoirs, are well characterized by their depth, geometry, and reservoir properties (Böcker, 2015; Bruss, 2000; Grandarovski, 1971), and seismicity and environmental impact have shown to be minimal during production. Potentially available heat sources for storage comprise excess heat from geothermal power plants or solar energy during summer, as well as waste heat from industrial processes. These sources are accompanied by a high heat demand in this densely populated area. Therefore, the HC reservoirs in the URG may represent ideally situated sites for HT-ATES. This also includes the water-bearing sandstone layers below the oil-water contact that presumably may be characterized by similar reservoir properties, even though no specific data on these layers are available from hydrocarbon or geothermal exploration.

Similar to the assessment of geothermal systems for energy production, numerical modeling represents a widespread approach to evaluate the potential of geothermal storage (Gao et al., 2017; Kohl et al., 2003; O'Sullivan et al., 2001). Storage capacity is mostly assessed by simulating operating shallow ATES systems with low injection temperatures (Bakr et al., 2013; Bridger and Allen, 2014). Rarely, these simulations were extended to HT-ATES with high injection temperatures in deep reservoirs (Major et al., 2018). Kastner et al. (2017) further show a numerical study for shallow ATES coupled with solar energy. Studies on geothermal storage mostly addressed the performance of storage systems (Drijver et al., 2012; Sommer et al., 2014) and investigated the influence of hydraulic (Ganguly et al., 2017) and thermal reservoir properties (Bridger and Allen, 2014). Further studies aim at the optimization of the placement and spacing of injection and production wells (Kim et al., 2010; Xiao et al., 2016) as well as the influence of reservoir heterogeneities (Bridger and Allen, 2014; Winterleitner et al., 2018).

As stated above, the framework conditions in the URG seem to be favorable for the economic usage of HC reservoirs as HT thermal energy storage in terms of geology, technology, and energy supply and demand. The objective of this paper is to quantitatively evaluate the general suitability and storage potential of HC reservoirs in the URG. The herein presented numerical investigation characterizes the possible heat storage in water-bearing reservoirs within depleted HC formations in the URG. Numerous simulations using a generic model of a HT-ATES system are carried out. These simulations are complementary to existing simulations of deeper geothermal systems in the URG (Bächler et al., 2003; Egert et al., 2020; Kohl et al., 2000), but specify a storage scenario and benefit from the broad database of HC reservoirs. In this context, available geological and petrophysical data from the URG are compiled and transferred into a numerical model to estimate the feasibility for HT-ATES. Next, a sensitivity analysis quantifies the storage behavior across the expected range of reservoir and operational parameters. Finally, the storage capacity of depleted HC reservoirs in the URG and total storage potential in terms of extractable energy are estimated.

3.2 DESCRIPTION OF DEPLETED OIL RESERVOIRS

3.2.1 *Regional and petroleum geology*

The Upper Rhine Graben (URG) is an about 300 km long NNE-SSW-trending continental rift system that has developed since about 47 Ma and accumulated up to 3.5 km of Cenozoic sediments (Figure 3.1). A first sedimentary sequence was deposited during WNW-ESE-extension at varying fluvial-lacustrine-brackish-marine conditions from late Eocene (c. 47 Ma) to Miocene (c. 16 Ma) times (Geyer et al., 2011). The deposition was followed by uplift and erosion mostly in the southern and central URG. This uplift and erosion phase caused a basin-wide unconformity in the URG, which can be identified in seismic sections (Rotstein et al., 2005). Basin-wide deposition resumed in Pliocene times within the present NE-SW-transtensional stress field (Figure 3.1). For a review and further details of the geological development of the URG see Grimmer et al. (2017) and references therein.

Hydrocarbon production in the URG occurred over more than 200 years, with a maximum of exploration and production activities in the 1950s to early 1960s (Figure 3.2; Reinhold et al., 2016; Rinck, 1987; Schnaebelé, 1948). Modern research on the petroleum system, sedimentary-stratigraphic evolution, and diagenesis has been resumed in recent times (Berger et al., 2005; Böcker, 2015; Bruss, 2000; Derer, 2003; Pirkenseer et al., 2013, 2011).

Oilfields in the URG can be either characterized by their origin from different source rocks (oil families A, B, C, D; Bruss, 2000) or by their reservoir rocks from which the hydrocarbons have been extracted (Reinhold et al., 2016) and comprise either (i) Mesozoic rocks or (ii) both Mesozoic and Tertiary rocks or (iii) solely Tertiary rocks (Figure 3.3). Stacked reservoirs, i.e., production of oil from more than one reservoir either at the oilfield scale or at the borehole scale, are a characteristic feature in the URG for most oil fields. Figure 3.3 shows the range of the annual production of German oil reservoirs in the URG, which can be used to estimate their minimum storage capacities.

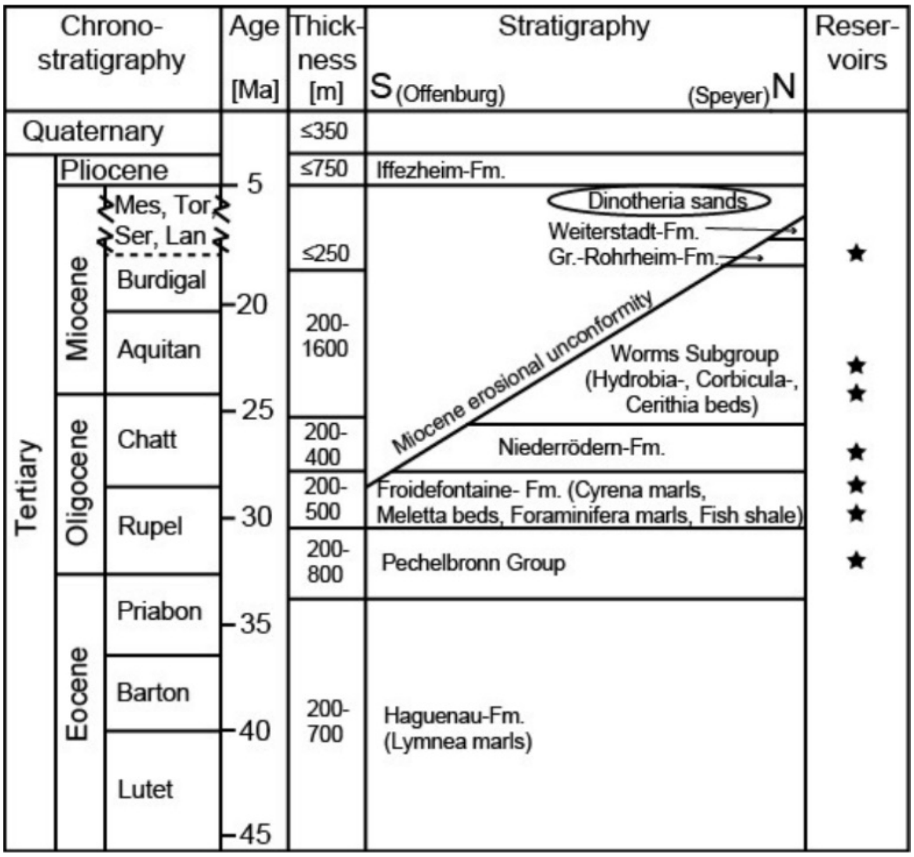

Figure 3.1: Stratigraphy of graben filling sediments in the central and northern URG Böcker (modified from 2015). Abbreviations of Miocene stages are as follows Mes.: Messinian, Tor.: Tortonian, Ser.: Serravalian, Lan.: Langhian. Asterisks mark formations that include hydrocarbon reservoirs and thus potential geothermal storage layers.

The permeability of Cenozoic reservoir rocks is predominantly porosity-controlled. These reservoirs occur mainly in (1) the Pechelbronn Group (Eich-Königsgarten, Stockstadt, Landau, Pechelbronn; Reinhold et al., 2016), (2) the Froidefontaine Formation, including the Meletta beds and Cyrena marls (e.g., *Leopoldshafen*), as well as (3) the Niederrödern Formation (e.g., *Leopoldshafen, Knielingen, Hayna, Rheinzabern, Graben, Huttenheim*) (Figure 3.3). Higher up in the stratigraphy, minor reservoirs of a few meter thick fractured dolomites and limestones rocks appear in the Worms Subgroup comprising the Cerithia, Corbicula, and Hydrobia beds. Medium to coarse-grained, weakly compacted sand layers in the Gr. Rohrheim and Weiterstadt Formations provide reservoir conditions for natural gas in the northern URG (e.g., *Eich-Königsgarten; Stockstadt*). These data typically originate from the boreholes drilled into the Tertiary stratigraphy. At the end of oil production at both individual borehole- and oilfield-scale the residual oil saturation, ROS, has commonly decreased to <10% (NLfB, 1963; Wolf and Hinners, 2013). In addition to low ROS, technical and economic reasons may also cause production stops. For locations at a larger distance from the oil-bearing parts of the reservoir, i.e., beneath the oil-water-contact (OWC), the reservoir rocks are assumed to be filled with formation waters with a negligible ROS; the reservoirs are thus referred to here as "depleted". As hydrocarbons accumulate in the uppermost parts of a reservoir rock, the exploited oil commonly represents only a minor portion of the total volume of the reservoir rocks.

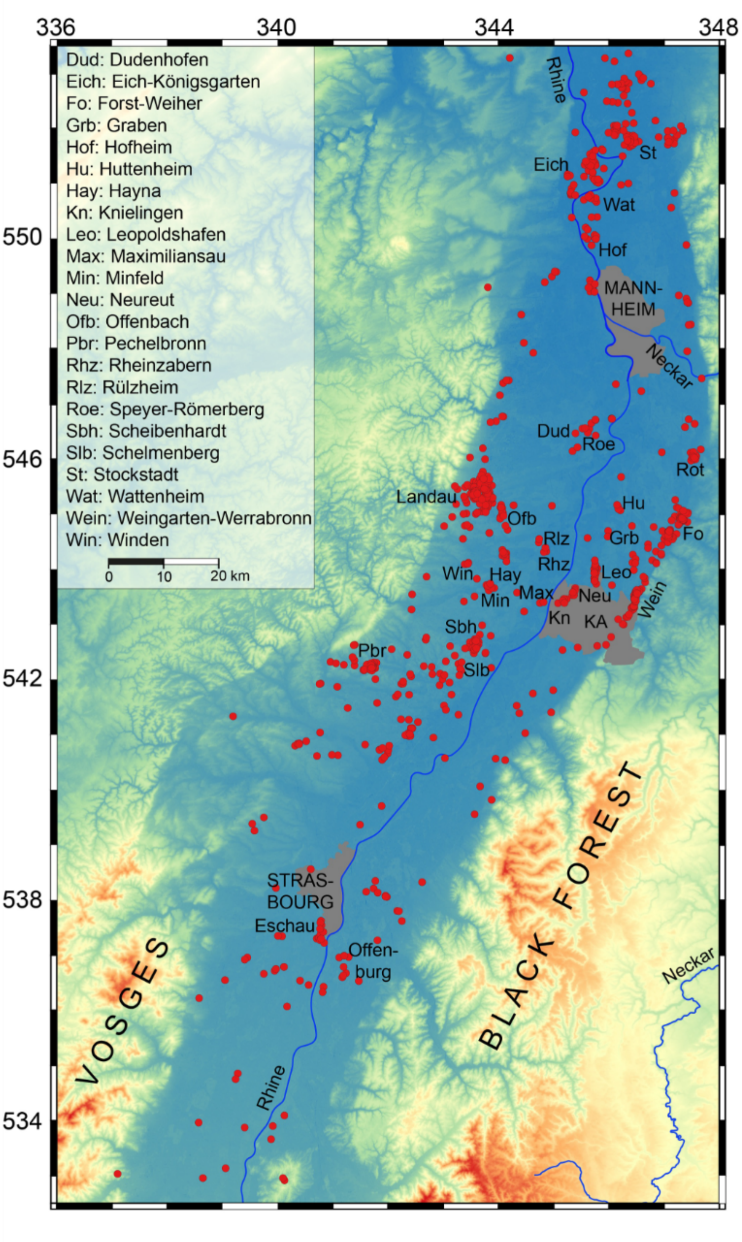

Figure 3.2: Digital elevation model of the Upper Rhine Graben area showing the distribution of boreholes ⩾500 m depth beneath surface (red circles) in the central Upper Rhine Graben. Data sources: Agemar et al. (2012), NASA et al. (2019). KA: Karlsruhe.

While the clay-rich Haguenau Formation essentially lacks significant reservoir rocks – except for few occurrences along the URG margins, the sequences of the Pechelbronn Group host reservoirs mainly in the northern URG (e.g., *Eich-Königsgarten*), but also along the eastern and western URG margins (Pechelbronn, Landau; Reinhold et al., 2016). The major Rupelian transgression caused full marine conditions in the URG and deposition of the Rupel Clay, a major basin-wide seismic reflector in the URG (Rotstein et al., 2005), representing the lower part of the Froidefontaine Formation (Böcker, 2015). Deposition of commonly 5–15 m, locally up to 23 m, thick calcareous fine-grained sand layers in the marine upper Meletta beds indicates short regressive phases (Pirkenseer et al., 2011). The stratigraphically overlaying Cyrena marls, deposited under brackish conditions, host fine to medium-grained calcareous sand-rich channel fillings with typical thicknesses of <10 m, but locally up to >40 m (Grandarovski, 1971; Sauer et al., 1981). These channel fillings pinch out within short lateral distances (Sauer et al., 1981). The Niederrödern Formation hosts ⩽20 m, locally up to >30 m, thick fluvial and lacustrine fine-grained marly sand layers and lenses that show lateral thinning or pinch-out within several hundred meters (Grandarovski, 1971; Sauer et al., 1981). Due to varying displacements between graben internal blocks (Grimmer et al., 2017; Wirth, 1962), the depth of these reservoir rocks varies between the surface to about 2000 m (Böcker, 2015; Bruss, 2000; Caron, 2012; GeORG-Projektteam, 2013; Grandarovski, 1971; Sauer et al., 1981) depending on their position between central and marginal fault blocks (Grimmer et al., 2017; Wirth, 1962).

Due to the intense deformation of the sedimentary successions in the URG, structural hydrocarbon traps prevail over sedimentary traps (Durst, 1991; Reinhold et al., 2016): Most hydrocarbons were trapped in slightly tilted sand-rich layers or lenses in the footwall of normal faults. These faults comprise either single (*Leopoldshafen*; Wirth, 1962) or multiple structural traps that are structurally rather simple (*Stockstadt, Eich, Scheibenhard*; Blumenroeder, 1962; Straub, 1962) or more complex (*Landau*; Schad, 1962). Along the eastern URG margin dome structures comprise structural traps (*Weingarten*; Wirth, 1962). Oil traps in gentle rollover structures occur locally (*Knielingen, Neureuth*; Wirth, 1962). Unconformities are of particular importance in the northern URG (*Eich*; Straub, 1962) for natural gas trapped in sand-rich layers of the Groß Rohrheim- and Weiterstadt-Formations beneath the regional Miocene unconformity and for the Mesozoic reservoirs (e.g., *Eschau, Römerberg (Speyer)*) beneath the basal Eocene unconformity of the URG, commonly covered by sealing mudstones of the Haguenau Formation. In the southern parts of the URG, Eocene evaporites comprise important seals of Mesozoic reservoirs (Blumenroeder, 1962). Hydrocarbon migration and accumulation appear to be a relatively young, possibly ongoing process in the URG that probably has been initiated during the late Miocene – early Pliocene times (Reinhold et al., 2016).

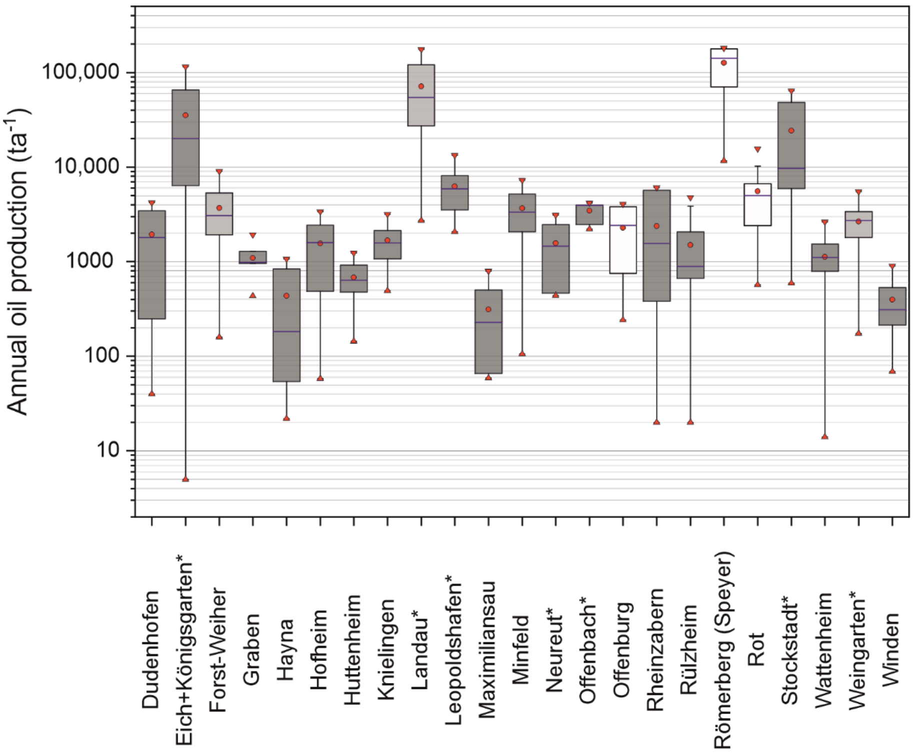

Figure 3.3: Annual oil production of German oil fields in the URG (LBEG, 2018). Shown are the mean production (red circle), the median production (blue line), the interquartile range (filled grey box), and the total variation (filled red triangles). Fields that have solely produced from the Tertiary are represented in dark grey, fields that have produced from both Tertiary and Mesozoic are in medium grey, and fields that have solely produced from the Mesozoic are in white boxes. Not shown are fields for which production data of only one year is available: Büchenau (168 ta^{-1}), Deidesheim (345 ta^{-1}), and Schwarzbach (632 ta^{-1}). The asterisks indicate the oil fields that are used for HT-ATES potential estimation (see Chapter 3.5).

3.2.2 *Thermal and petrophysical data of reservoir rocks*

The URG is characterized by deep-reaching thermal anomalies resulting from fault-controlled convective fluid flow mostly within the crystalline basement and Mesozoic successions beneath low permeable clay-rich graben filling sediments (Bächler et al., 2003; Baillieux et al., 2014). These anomalies are also evident in the Cenozoic graben filling sediments, with temperatures locally exceeding 140 °C in 2 km depth (Baillieux et al., 2013; Pribnow and Schellschmidt, 2000) and geothermal gradients between 35 K km^{-1} and 58 K km^{-1}, locally even reaching gradients of up to 100 K km^{-1} (Agemar et al., 2012; Sauer et al., 1981).

For heat storage systems, the hydraulic properties (e.g., porosity and permeability) of the rock are of key importance. Typical porosities and permeabilities of 5–20% and 10^{-16}–10^{-14} m^2, respectively, are obtained from 85 core samples belonging to 39 exploration and production wells in 19 different oil-bearing Tertiary reservoir rocks in the URG (Böcker, 2015; Bruss, 2000; Caron, 2012; GeORG-Projektteam, 2013; Grandarovski, 1971; Sauer et al., 1981). Heterogeneous carbonate cementation and secondary carbonate dissolution (Bruss, 2000) lead to porosities of 30% and permeabilities of 10^{-12} m^2 (Figure 3.4). While an exponential correlation between porosity and permeability is observed, both values show no straightforward correlation with depth and cannot be used to distinguish between different target formations. Note that due to larger uncertainties, logging data (as compiled by e.g., Bär et al., 2020) are not included in Figure 3.4 and not further considered.

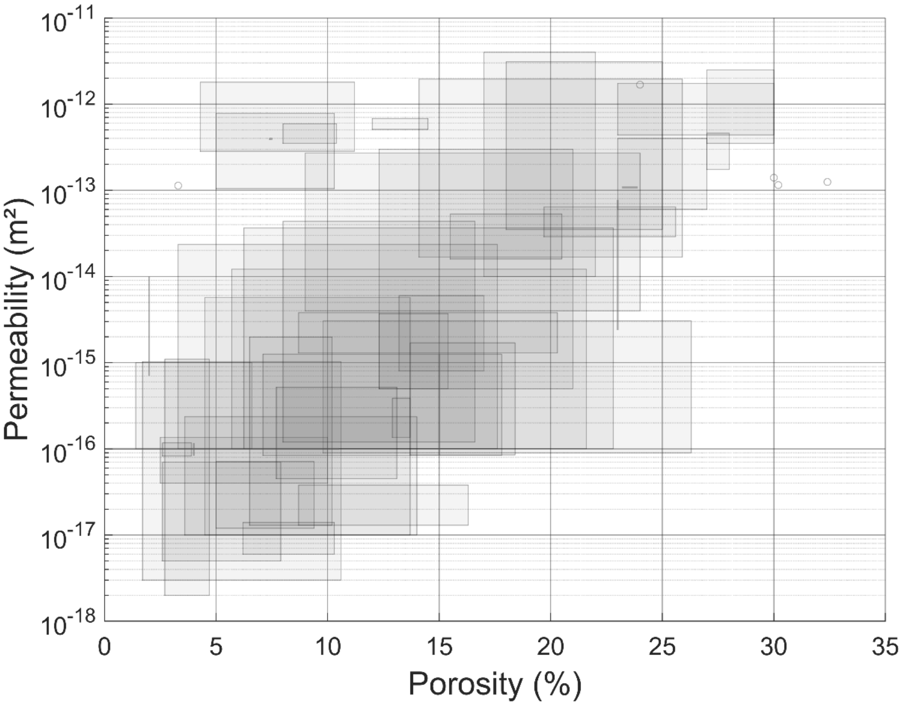

Figure 3.4: Overview of porosity and permeability data measured from core plugs of Tertiary oil reservoir rocks in the central URG (France and Germany; # of data sets: 51). Rectangles mark individual data spread for both porosity and permeability data from individual sites and depths, respectively. Small circles mark specific data from one site. Greyscale displays the maximum stacking of individual data sets. Data are compiled from the following literature (Böcker, 2015; Bruss, 2000; Caron, 2012; GeORG-Projektteam, 2013; Grandarovski, 1971; Sauer et al., 1981).

Thermal properties of Tertiary rocks in the URG are very scarce and reveal large variations and uncertainties. Whereas thermal conductivities were measured on core samples (GeORG-Projektteam, 2013; Hintze et al., 2018; Sattel, 1982), data on heat capacities are only available for comparable lithologies of the same age in the Northern German Basin (Magri et al., 2008; Scheck, 1997).

3.3 NUMERICAL MODELING

Data of depleted HC reservoirs in the URG are the basis of a numerical evaluation of the viability and efficiency of seasonal HT-ATES in these reservoirs. The numerical study is especially advantageous to quantify the impacts of uncertainties in the compiled geological and petrophysical data. Our modeling approach is limited to the REV concept ("representative elementary volume"; Bear, 1972) and the mutual coupling of hydrothermal processes. The modeling concept of the seasonal HT-ATES is assuming a doublet borehole system consisting of a cold and a hot leg with semi-annual injection and production load-time-functions (Figure 3.5). In this way, the cold leg is used for the injection during winter and the production during summer, whereas the hot leg is operated in the opposite configuration. It offers the advantage of installing specific temperature-dependent compounds in each well. Due to the low thermal diffusivities of rock (Clauser and Villinger, 1990) steady-state conditions cannot be reached after a foreseeable period. Therefore, a transient approach is used for modeling with a total simulation period of ten years.

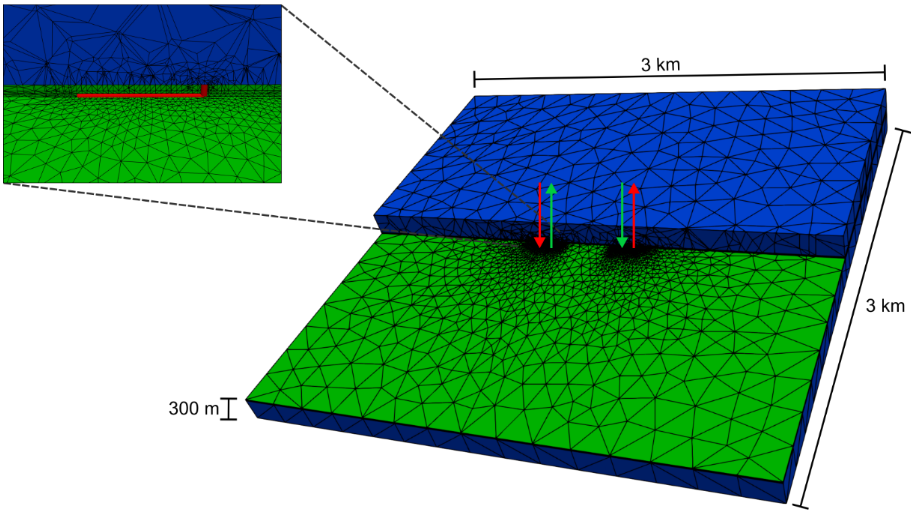

Figure 3.5: Generic model developed to analyze the feasibility and potential of HT-ATES in the URG. The model consists of a reservoir of variable thickness (5, 10, or 20 m; green) and two confining layers (blue). The enlarged section in the upper left gives a detailed view of the refined mesh around the hot well of the doublet. The arrows illustrate the semi-annual injection and production during summer (red) and winter (green).

3.3.1 *Modeling approach*

The mass transport equation used to estimate the pore pressure, p, is given by mass balance along with the Darcy velocity, $\boldsymbol{q}$, as follows (Bear, 1972):

$$S_m \frac{\partial p}{\partial t} + \nabla \cdot \boldsymbol{q} = Q \tag{3.1}$$

$$\mathbf{q} = \frac{\boldsymbol{k}}{\mu}(-\nabla p + \rho_f \boldsymbol{g}) \tag{3.2}$$

S_m is the mixture specific storage coefficient of the medium; t is the time; Q is the source/sink term for injection and production, $\boldsymbol{k}$ is the permeability tensor, μ and ρ_f are the fluid dynamic viscosity and density, respectively and $\boldsymbol{g}$ is the gravitational acceleration. In the considered scale of geothermal storage, fluid dynamic viscosity, and density nonlinearly depend on temperature and pressure (Smith and Chapman, 1983). This nonlinearity leads to high computational efforts.

It is assumed that the solid and liquid phases in porous media are in local thermodynamic equilibrium. Heat transport, used to estimate the temperature, can be mathematically expressed using the advection-diffusion equation as:

$$\rho c_p \frac{\partial T}{\partial t} - \boldsymbol{\lambda} \nabla^2 T + (\rho c_p)_f \boldsymbol{q} \nabla T = 0 \tag{3.3}$$

ρc_p and $\boldsymbol{\lambda}$ are the volumetric heat capacity and thermal conductivity of the mixture, respectively. $(\rho c_p)_f$ represents the volumetric heat capacity of the fluid. The open-source code TIGER (THC sImulator for GEoscientific Research; Gholami Korzani et al., 2020) has been deployed, which is based on the described assumptions and implemented within the object-oriented framework MOOSE (Gaston et al., 2009; Permann et al., 2020).

With ROS being ignored for the simulated water-bearing formations, only single-phase flow is considered. It is assumed that injection and production take place below the oil-water contact in the reservoir layer and are not affected by accumulations of residual oil. Besides, it may be assumed that potential ROS is further reduced after a few injection and production cycles having washed out any oil traces.

A generic 3D model of a potential HT-ATES site in the URG represents the core of the numerical study. The center of the reservoir is assumed to be at a depth of 1.2 km corresponding to an average value of former oil reservoirs. The lateral extension of the model (3 km × 3 km) is chosen to avoid any boundary effects on the area of interest. Vertically, the model extends over 300 m with three layers assumed: the reservoir in the center of the model with variable thicknesses of 5, 10, or 20 m and two confining layers with equal thicknesses (Figure 3.5). The selected thickness values of the confining layers further assure that top and bottom boundaries do not affect the modeling area of interest. Two wells are located in the center of the model with a lateral distance of 500 m from each other to avoid any thermal interference between the wells as this significantly reduces the storage efficiency (Gholami Korzani et al., 2020; Sommer et al., 2015). Two different well trajectories were considered: (1) vertical boreholes only and (2) a vertical section covering the top half of the reservoir layer with a horizontal section of 100 m length in the center of the reservoir layer pointing in opposite directions. While the vertical design represents a normal borehole, the addition of a horizontal section represents a technical approach to increase the contact area between the borehole and the reservoir, similar to the effect of a larger reservoir thickness.

The unstructured mesh consisting of tetrahedral elements was created by the Gmsh software (Geuzaine and Remacle, 2009). The element sizes vary between 2.5 m (along the vertical well sections) and 187.5 m (at the model boundaries). Further refinement was performed along the horizontal well sections as well as in the area surrounding the wells where the highest gradients of the pressure and temperature field are expected to occur. A mesh sensitivity analysis was performed to avoid any mesh dependency on the results. In total, the model contains 18,589 nodes connected by 107,894 elements.

Hydrostatic pore pressure was applied to the model by setting Dirichlet boundary conditions (BCs) at the top and the bottom of the model domain with an associated initial condition (IC). Injection and production flow were implemented by using time-dependent mass flux functions at the top of the reservoir with six months' cycles. These time-dependent functions represent simplified approximations of a real pumping operation by assumed instantaneous reversal of the pumping direction at the end of each cycle. The temperature distribution within the model is based on a favorable geothermal gradient of 50 K km^{-1} under the URG setting (see above). It was achieved by setting Dirichlet BCs at the top and the bottom of the model domain and corresponding ICs throughout the model. To implement the injection of water with a specific temperature into the two wells, Dirichlet BCs at the top of the reservoir (corresponding to the beginning of the open hole section) are activated during the injection period of the respective well.

It is considered that the hydraulic operational parameters imply major constraints for the operation of HT-ATES. Both, flow rate and associated pressure changes involve a potential hazard to induce micro-earthquakes. Herein, we assume a cautious operation in an urban or sensitive environment limiting the hydraulic parameters to a maximum overpressure of P_{max} = 2 MPa and flow rate of Q_{max} = 10 Ls^{-1}. Experience has shown, that this P_{max}/Q_{max} combination does not create a major mechanical impact (induced seismicity; Evans et al., 2012; Zang et al., 2014) on a reservoir. This cautious combination can be exceeded under specific conditions. Model simulations are thus aborted if pressure changes caused by the injection exceed this P_{max} threshold.

3.3.2 *Reference case*

A reference model (hereafter called "reference case") of typical parameterization (Table 3.1) was developed to demonstrate the general behavior of an HT-ATES. It also serves for comparison to further parameter sensitivity studies. The two seasonal operation modes are represented by injection with a temperature of 140 °C in the hot well during the summer (using the cold well as producer) and an inverted mode during the winter when water with a temperature of 70 °C (i.e., the ambient reservoir temperature) is injected in the cold well (using the hot well as producer).

The selected temperature conditions do not imply an energy balanced storage operation. The setting involves a negative energy budget due to the diffusive losses around the hot well as water with a temperature exceeding the ambient reservoir temperature is stored. As a result, the simulation is resulting in continuous warming of the reservoir next to the hot well. The minimum production temperature at the end of each winter operation increases from 94.5 °C after the first year to 112.7 °C after the 10th year (Figure 3.6). It reflects the accumulation of thermal energy in the reservoir that is also shown in Figure 3.7. This behavior agrees with earlier assessments of geothermal storage systems (Kim et al., 2010). Under the assumed conditions the thermal perturbation during injection extends over a maximum distance of 90 m from the hot well after 10 years. The accumulation of heat leads to a slow temperature increase in the reservoir and yields a decreasing diffusive heat loss with time (Drijver et al., 2012). The temperature difference of 70 K between injection and ambient conditions will thus reduce with time and reservoir temperature asymptotically approaches injection temperatures of 140 °C at near steady-state conditions. This contrasts the behavior of shallow storage systems with smaller temperature differences close to a balanced energy budget (Kim et al., 2010), where near steady-state conditions are reached after a comparably short operation time of already three years.

Table 3.1: Parametrization of the reference case.

Parameter	**Value**
Reservoir thickness (m)	10[a]
Reservoir permeability (m^2)	6.6×10^{-14}[a]
Bulk thermal conductivity of the reservoir ($W.m^{-1}K^{-1}$)	2.5[a]
Bulk thermal conductivity of the caprock ($W.m^{-1}K^{-1}$)	1.4[a]
Injection/production flow rate (Ls^{-1})	2[a]
Injection temperature of the cold well (°C)	70[a]
Injection temperature of the hot well (°C)	140[a]
Porosity (reservoir and caprock) (-)	0.15[a]
Permeability of the caprock (m^2)	10^{-18}[a]
Volumetric heat capacity of the reservoir ($MJ.m^{-3}K^{-1}$)	3.15[e]
Volumetric heat capacity of the caprock ($MJ.m^{-3}K^{-1}$)	3.3[e]
Fluid thermal conductivity ($W.m^{-1}K^{-1}$)	0.65[d]
Fluid specific heat capacity ($J.kg^{-1}K^{-1}$)	4194
Fluid density (kgm^{-3})	1060[b]
Fluid dynamic viscosity (Pa.s)	f(T,p)[d]
Well diameter (m)	0.2159[a]

Data origin is marked with [a]our data compilation/assumptions, [b]Millero et al. (1980), [c]Smith and Chapman (1983), [d]Coker and Ludwig (2007), [e]Scheck (1997). In contrast to the above described general nonlinear dependency of the fluid density on temperature and pressure, it is kept constant in the modeling due to its insensitivity on the modeling results.

This behavior is reflected by an improved recovery efficiency, ε. It represents an important parameter for the feasibility of heat storage systems and is defined as the ratio between extracted and stored energy. Since the conditions at the cold well do not change, ε characterizes the conditions at the hot well:

$$\varepsilon = \frac{\int (T_p(t) - T_a)\ dt}{\int (T_i(t) - T_a)\ dt} \tag{3.4}$$

with $T_p(t)$ the production temperature, $T_i(t)$ the injection emperature, and T_a the average initial reservoir temperature. Herein, ε is calculated for periods with a length of one year.

Figure 3.6 shows an increase in ε from 66% in the 1st year to 82% in the 10th year. These values correspond to the amount of extracted energy increasing from 1.8 GWh to 2.2 GWh under the conditions of the reference case with

2.7 GWh of heat injected annually in the reservoir. These high ε values seem to be representative for geothermal systems as they confirm earlier studies for low (Kim et al., 2010) or high-temperature storage (Kastner et al., 2017; Sommer et al., 2013). The increase of ε of 16% in the reference case compares well to earlier studies on shallow thermal storage, implicating increases between 1% and 30% (Drijver et al., 2012; Major et al., 2018).

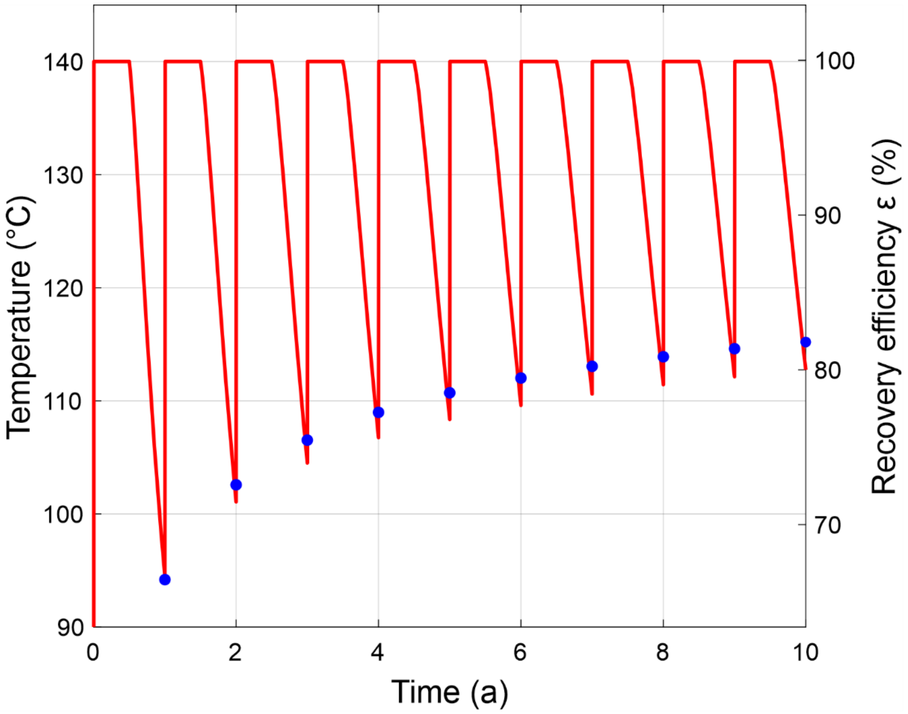

Figure 3.6: Temperature over time (red curve) of the reference case model. The blue circles show the recovery efficiency ε of each year.

3.4 PARAMETER SENSITIVITY ON RECOVERY EFFICIENCY

The findings of the reference case exemplify the behavior of an HT-ATES based on an average reservoir parametrization of the URG. Chapters 3.2.1 and 3.2.2 show a large variety of relevant parameters for a general resource estimation of depleted hydrocarbon reservoirs in the URG. Herein, we systematically investigate the influence of the most important reservoir parameters and the drilling trajectory to determine their impact on storage efficiency, using an adapted and extended filtering concept, which was originally developed in Gholami Korzani et al. (2020). The following sensitivity range is investigated (Table 3.2).

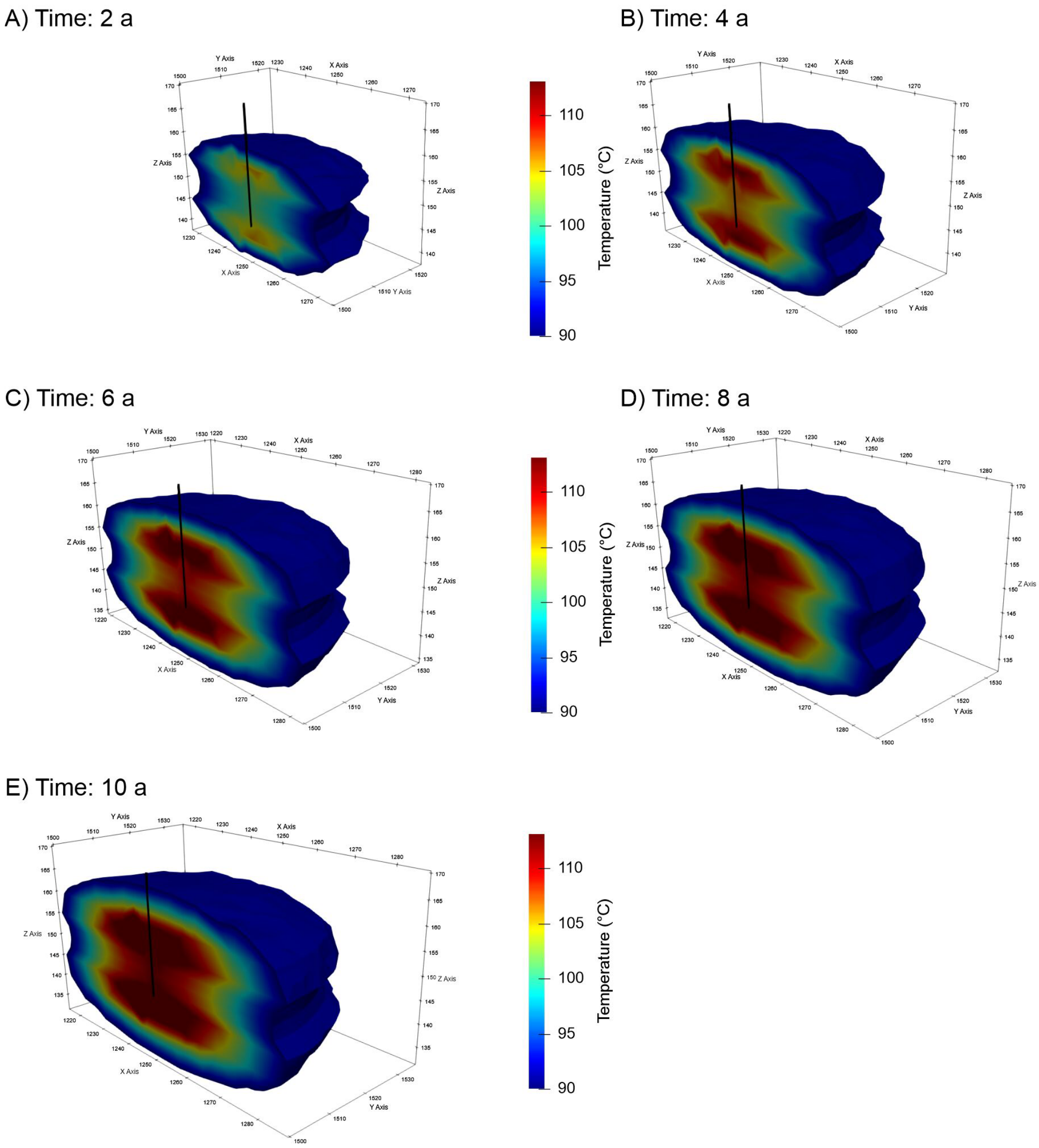

Figure 3.7: Evolution of the reservoir temperature after (**A**) 2 years, (**B**) 4 years, (**C**) 6 years, (**D**) 8 years, and (**E**) 10 years. Shown is the state of the reservoir of the reference case at the end of the winter production phase next to the hot well.

3.4.1 *Parameter variation for the vertical well setup*

The influence of reservoir thickness, permeability, and flow rates on ε is first investigated with constant thermal conductivities (λ_{res} = 2.5 / λ_{cap}= 1.4 $Wm^{-1}K^{-1}$) for a vertical well setup. For the parameter variation an adapted grid sampling was used based on Table 3.2 (see Table A.1). Figure 3.8 shows the impact of reservoir thickness and flow rate on ε with higher values being obtained for higher thicknesses and flow rates. After the 10th operation cycle ε <77% is reached for a thickness of 5 m and ε of up to >87% for a thickness of 20 m. Under the constraints of the P_{max} threshold, typically a minimum permeability between 10^{-14} m² and 10^{-13} m² (cases I and IV in Figure 3.8) is required for these HT-ATES with even higher values for higher flow rates. At a given permeability, high reservoir thicknesses allow for more variable flow rates due to their lower injection pressure, e.g., at 10^{-13} m² flow rates can increase up to the Q_{max} = 10 Ls^{-1} threshold, whereas at 10^{-14} m² flow rates can only reach 1 Ls^{-1}.

Table 3.2: Selected ranges of geological and operational parameters to determine their influence on recovery efficiency ε.

Parameter		**Range**	
		Min	**Max**
Reservoir permeability (m^2)	Vertical well	6.6×10^{-15}	3.3×10^{-13}
	Horizontal well	1×10^{-15}	3.3×10^{-13}
Reservoir thickness (m)		5	20
Thermal conductivity (W$m^{-1}K^{-1}$)	Reservoir (λ_{res})	2	3
	Cap rock (λ_{cap})	1	2
Injection/production flow rate (Ls^{-1})		1	10

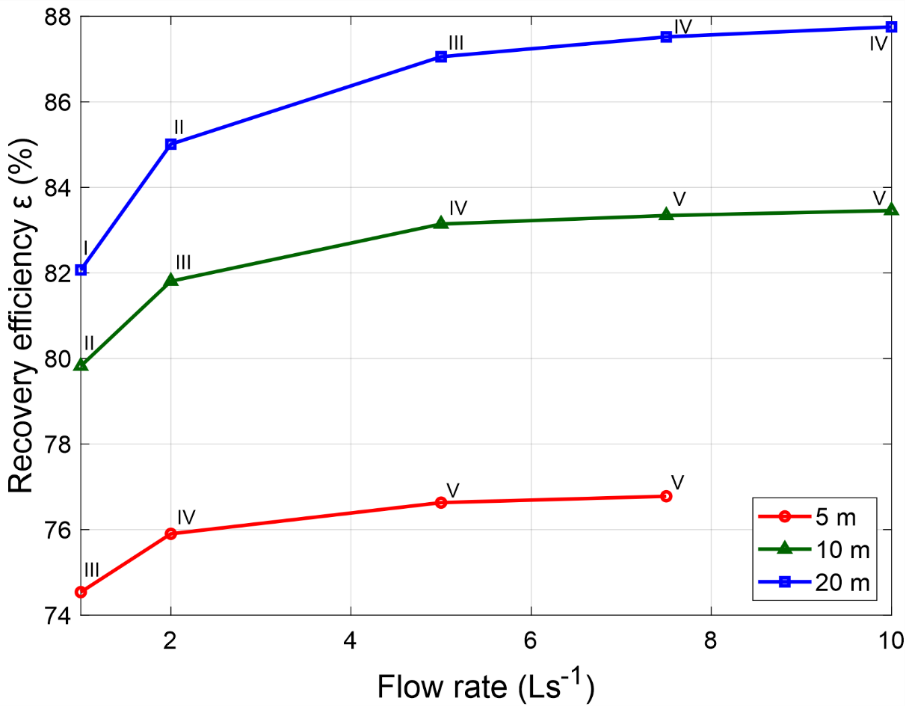

Figure 3.8: The dependency of ε on flow rate, reservoir permeability, and thickness. The numbers identify the specific permeability for each flow rate: (I) 10^{-14} m², (II) 3.3×10^{-14} m², (III), 6.6×10^{-14} m², (IV), 10^{-13} m², and (V) 3.3×10^{-13} m².

The sensitivity of these three parameters on ε is illustrated in Figure 3.9. Due to the limitations set by the P_{max} threshold, the sensitivity was calculated in comparison to a model slightly different from the reference case (with a permeability of 10^{-13} m² instead of 6.6×10^{-14} m²). A variation of reservoir thickness represents the strongest individual influence on ε with a 50% variation leading to a change in ε of nearly 10%. The same variation for flow rate leads only to a change in ε of 2%. Although reservoir permeability shows only a low influence on ε, its importance arises from its impact on the pressure evolution in the reservoir and thus the operation with high flow rates. It can be concluded that major attention should be paid to the reservoir thickness when choosing a potential HT-ATES site.

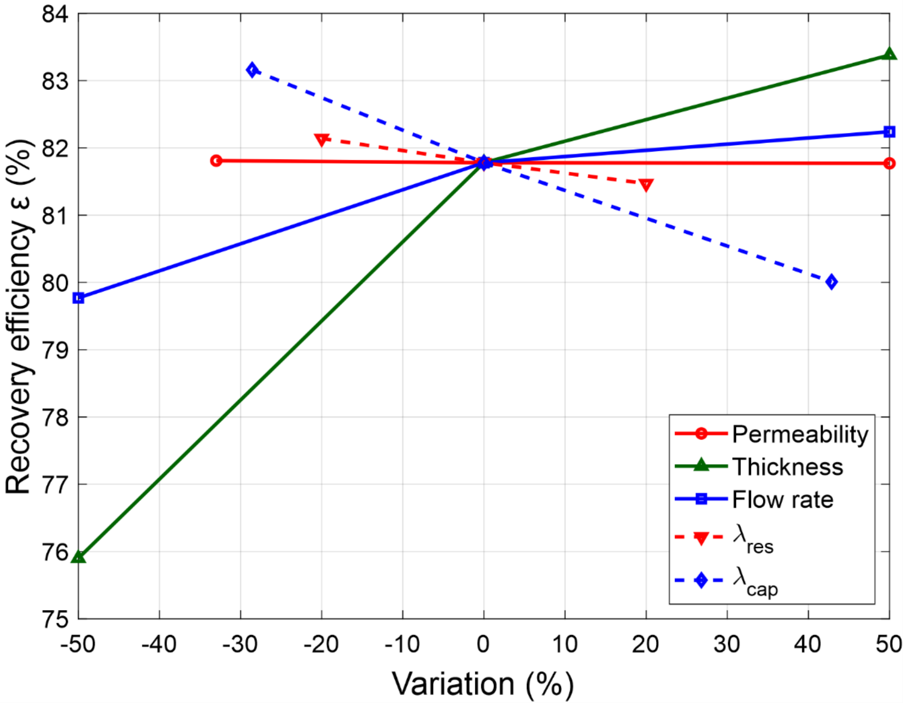

Figure 3.9: Sensitivity analysis on the parameter influence on ε. The shown changes are referenced to a model comprising a permeability of 10^{-13} m², a thickness of 10 m, and a flow rate of 2 Ls^{-1}.

Figure 3.9 also illustrates the influence of thermal conductivity. For this purpose, the flow rate was kept constant at 2 Ls^{-1} and reservoir permeability at 10^{-13} m². The importance of proper treatment of λ_{res} and λ_{cap} is highlighted by the fact that the impact of their variation on ε reaches the same order of magnitude as changes in flow rate and reservoir thickness. This means that variations of thermal conductivities in the subsurface should receive equal attention as hydraulic and geometrical reservoir parameters in the planning of HT-ATES sites. On the other hand, this further implies that all results regarding the variation of hydraulic and geometrical parameters are additionally subjected to the described uncertainties related to varying thermal conductivities of both the caprock and the reservoir.

Figure 3.10 provides more details to this statement for variations of λ_{res} and λ_{cap}. Typically, a lower λ_{cap} tends to isolate the reservoir leading to higher ε whereas higher values imply higher heat losses. At lower reservoir thicknesses a variation of λ_{res} is nearly insignificant (manifesting as vertical ε isolines in Figure 3.10a). λ_{res} is only getting important when the reservoir thickness increases drastically, yielding inclined ε isolines (Figure 3.10c). This effect is caused by the decreasing influence of the caprock (acting as a thermal insulator) on the propagation of the injected hot water.

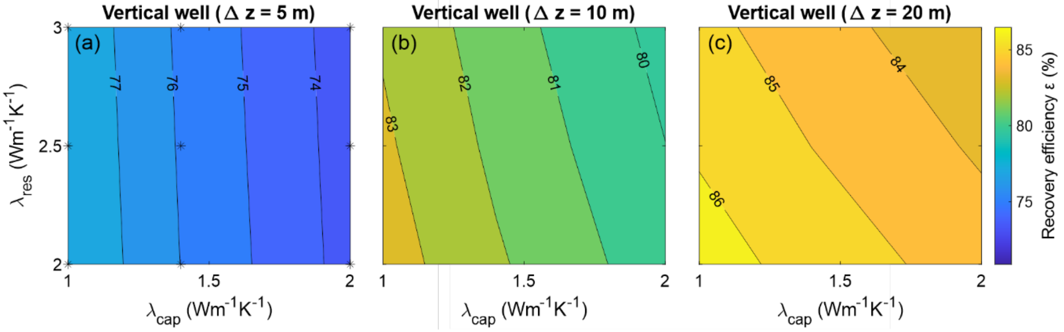

Figure 3.10: Comparison of the influence of the variation of the thermal conductivities of the reservoir (λ_{res}, on the y-axis) and the caprock (λ_{cap}, on the x-axis) on ε for reservoir thicknesses of 5 m (**a**), 10 m (**b**), and 20 m (**c**). In the left figure (**a**) the simulated scenarios are marked by asterisks.

3.4.2 *Comparison of vertical and horizontal well setups*

Drilling horizontal wells are becoming a standard procedure for the exploitation of hydrocarbon reservoirs (Allouche et al., 2000; Burgess and van de Slijke, 1991) and could also be a possible blueprint for geothermal storage. Therefore, and particularly concerning the geological setting of potential reservoir layers in the URG, the influence of the well setup on the operation of HT-ATES is investigated by comparing the vertical well setup with a 100 m long horizontal well setup. Figure 3.11 shows the results for a 10 m thick reservoir layer with permeability and flow rate variations as provided in Table 3.2.

The horizontal well section leads to reducing pressure variations within the reservoir due to the larger contact area between the well and the reservoir compared to the vertical drill path. Consequently, higher operational flexibility could result from applying higher flow rates or utilizing reservoirs of otherwise uneconomically low permeability (Figure 3.11). For a permeability of 10^{-13} m^2 (case IV in Figure 3.11), for instance, drilling of such a horizontal well section leads to an increase of the maximum flow rate from 5 Ls^{-1} to 10 Ls^{-1} or reservoirs with a permeability of 10^{-14} m^2 (case I in Figure 3.11) could still be used. However, drilling horizontal wells could also have minor adverse effects. At low flow rates, the higher heat transfer through the larger surrounding surface area will increase heat losses and results therewith in lower ε. This difference diminishes with higher flow rates.

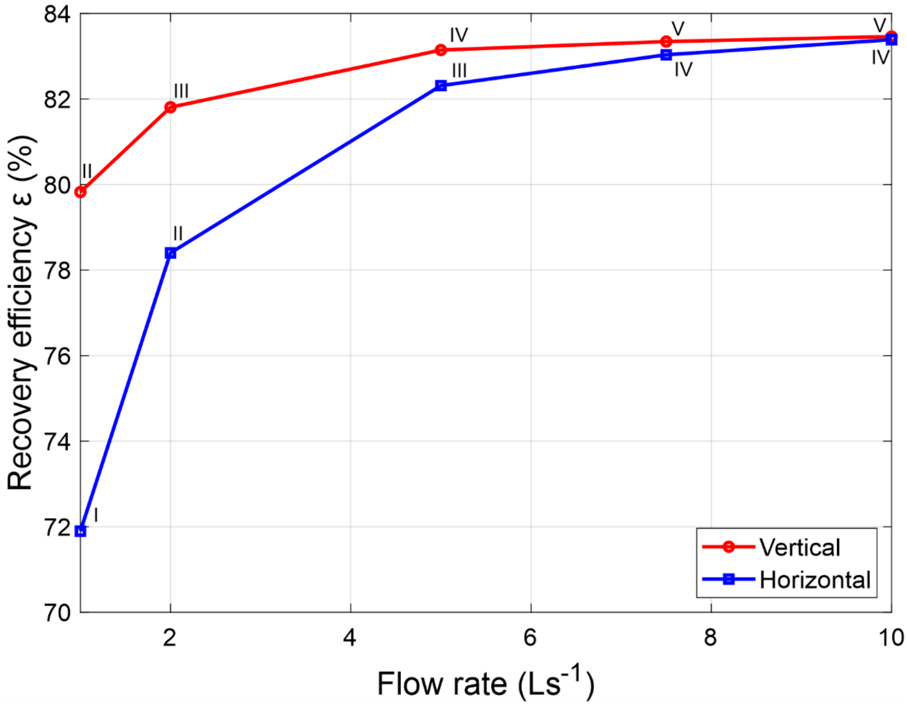

Figure 3.11: The dependency of ε on reservoir permeability, flow rate, and the well setup. The numbers identify the specific permeability for each flow rate: (I) 10^{-14} m^2, (II) 3.3×10^{-14} m^2, (III), 6.6×10^{-14} m^2, (IV), 10^{-13} m^2, and (V) 3.3×10^{-13} m^2.

3.5 DISCUSSION AND POSSIBLE ENERGY EXTRACTION IN THE URG

To assess the potential of specific HT-ATES systems, it is necessary to consider the storage capacity, i.e., the total energy stored and extracted, rather than recovery efficiencies. Herein, we refer to the storage capacity ΔE_{stor} as the total amount of energy extracted during the 10th year of operation. Figure 3.12 compares ΔE_{stor} for the vertical and the horizontal well setup for identical P_{max} constraints (i.e., all models assume $P = P_{max}$ at injection). It can be observed that ΔE_{stor} varies between values of 1–12 GWh a^{-1} and increases with reservoir permeability and thickness. Despite slightly lower recovery efficiencies, the use of the horizontal well setup leads to a significantly higher absolute storage capacity for the given permeability/thickness combination due to higher total flow rates. Especially in the critical permeability range between 10^{-14} m^2–10^{-13} m^2, the horizontal well setup offers advantageous settings. The results of Figure 3.12 are further constrained by the Q_{max} threshold limiting the maximum storage capacity of the power plant. Thus, the maximum capacity can become independent of the borehole geometry if the maximum flow rate is reached resulting in a maximum storage capacity of 12 GWh a^{-1}. At a higher Q_{max} threshold, the storage capacity could further increase.

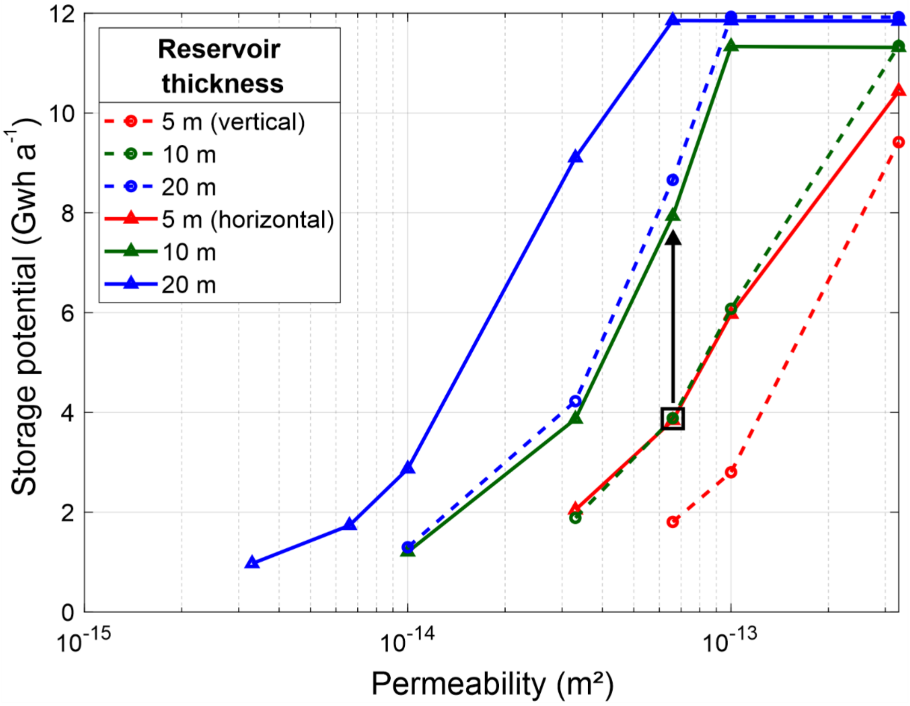

Figure 3.12: Maximum annual energy extraction (= storage capacity) as a function of reservoir permeability and thickness for both, a vertical and a horizontal well setup. The black frame marks the permeability-thickness combination of the reference case, the black arrow illustrates the increase in the storage potential for the horizontal well setup.

The possible gain in ΔE_{stor} through horizontal wells is illustrated by comparing the reference case (vertical well, black square in Figure 3.12) to its horizontal counterpart (black arrow in Figure 3.12). Under the given threshold conditions, the reference case allows the storage of 3.9 GWh a^{-1}, whereas a horizontal well reaches 7.9 GWh a^{-1}. This corresponds to an increase of about 100% in annual storage capacity.

The described higher storage capacity of the horizontal well setup is mainly of importance at low permeability and/or low reservoir thickness since it can turn uneconomic exploitation into a valuable business case. For reservoirs with very low permeability ($<10^{-14}$ m²) and thicknesses, longer horizontal well sections could thus be considered. For instance, a well with a 500 m long horizontal section would even allow the exploitation of reservoirs with permeability $\geqslant 10^{-15}$ m². However, since this also results in higher investment costs, the vertical well setup can be more economically viable for high permeabilities. The optimal well setup has always to be determined specifically for each potential site.

As the last step of this potential analysis, the assessment of ΔE_{stor} of potential HT-ATES in depleted oil fields of the URG needs to be tackled. Herein, we combine our synthetic numerical findings with the available data from oil reservoirs. This evaluation is limited to a subset of reservoirs described in Chapter 3.2 with available measurements on permeability and thicknesses consisting of 41 wells in 10 reservoirs (as shown in Table A.2). A histogram of possible storage capacity is provided in Figure 3.13 derived from the parameter range of this subset assuming a vertical/horizontal well setup and thermal conductivities of the reference case (λ_{res} = 2.5 and λ_{cap}= 1.4 $\mathrm{Wm^{-1}K^{-1}}$) as only scarce information on λ_{res} and λ_{cap} in the URG exists. As expected, the storage capacity of the horizontal wells is more favorable compared to vertical wells. Figure 3.13 indicates a maximum ΔE_{stor} for vertical wells between 4 and 6 GWh and for horizontal wells at ΔE_{stor} >10 GWh. This distribution is especially a clue for the realization of these systems with ΔE_{stor} >8 GWh being reached for approx. 70% of all horizontal wells but only 27% of the vertical wells.

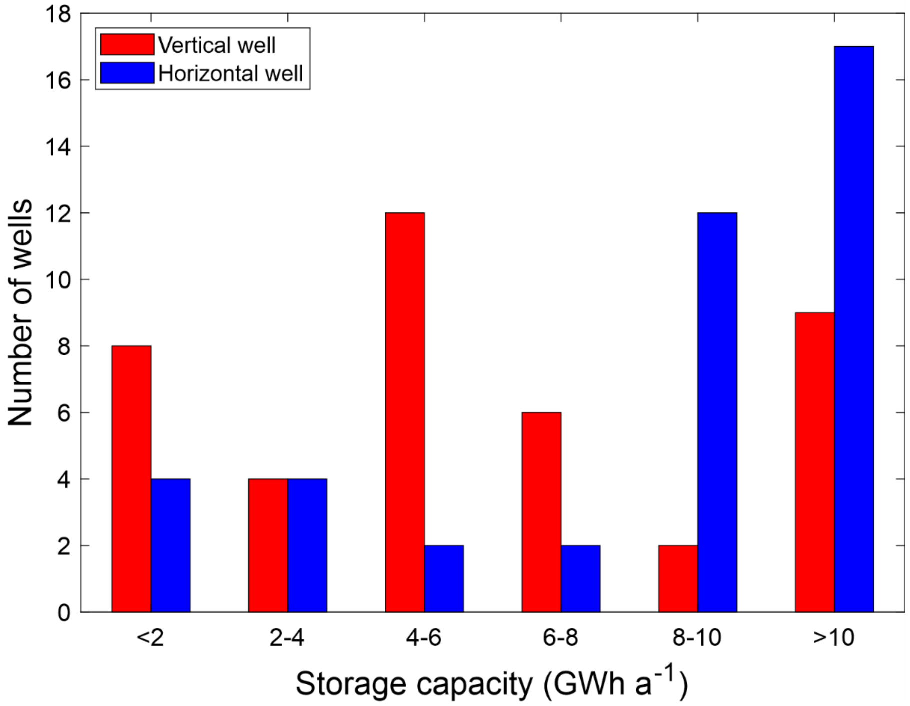

Figure 3.13: Distribution of the storage capacity for the selected subset of oil fields in the URG (for details see Table A.2). The bars illustrate the storage capacity of these oil fields for both the vertical (red) and the horizontal (blue) well setup assuming average measurements of the permeability and thickness of the respective reservoirs when operated at P_{max}.

Assuming a minimum economic threshold of ΔE_{stor} = 2 GWh as reached, for example, by the Reichstag storage system in Berlin (Kabus and Seibt, 2000), 80% of the vertical and 90% of the horizontal wells would provide sufficient reservoir conditions. Even if the minima of the underlying data are considered as representative instead of average values, a considerable number of reservoirs would still meet the assumed economic threshold (46% of the vertical and 76% of the horizontal wells).

If we assume that the selected subset of reservoirs is representative of all depleted oil reservoirs, the total potential of HT-ATES in the URG can be estimated. In the URG, 26 German and 36 French depleted oil reservoirs exist (including reservoirs with exploration activity only) and characteristically constitute stacked reservoirs with more than one reservoir layer. The exploitation of these reservoirs by horizontal wells could lead to a storage potential in the magnitude of up to 1000 GWh a^{-1} assuming average capacities of approx. 10 GWh a^{-1}. The exploited area even of horizontal wells is typically restricted to a 100 m distance from the well (see example in Figure 3.7) leading to a storage area of less than 1 km^2 assuming a lateral distance of 500 m between the boreholes. Especially in the case of the laterally extensive Meletta beds, it may be assumed that the potentially usable size of the depleted reservoir exceeds this storage area, leading to a possible realization of multiple storage doublets per reservoir. This may further scale the potential capacities of HT-ATES in the URG to the magnitude of up to 10 TWh a^{-1}. This order of magnitude compares well to the regional thermal energy demand. Taking as a basis the annual thermal energy need of Germany of 1800 TWh (BDEW, 2019), the annual thermal energy need for the 6 million inhabitants in the URG (EURES, 2008) would scale down to 135 TWh. In this context, HT-ATES would cover a significant share in a sustainable manner. However, future analyses have to focus also on a life cycle analysis considering the intrinsic energy need for operating these systems and have to quantify the economic impact. Potentially available sources of sustainable heat may include excess heat from geothermal production (i.e., from deeper reservoirs such as the Mesozoic Buntsandstein) or solar energy as well as waste heat of industrial processes. However, numerical studies and economic analyses are of limited significance and cannot replace the analysis of real systems. Therefore, the potential of this new geothermal technology needs to be quantified by scientific demonstrators.

3.6 CONCLUSIONS AND OUTLOOK

HT-ATES could potentially play an important role in storage scenarios required for a climate-neutral society, but this new technology has to prove its feasibility and meet the necessary public acceptance. In this respect, areas of former hydrocarbon production could provide both, the necessary reservoir conditions and the knowledge on these as well as the local experience of low-hazard hydrocarbon production for more than 50 years. Based on the extensive production experience, it can be expected that the storage operation in the soft, clay-rich sediments of the Tertiary rock to be mostly aseismic. Moreover, a low flow rate – much lower than required for geothermal power production – is applicable, further reducing the seismic risk, especially for densely populated areas.

Such a concept could also perfectly symbolize the transition from a hydrocarbon-based past to renewable energy in the future. As shown by this study, depleted oil reservoirs represent an important resource potential for HT-ATES systems in the URG. Despite the modest permeability and thickness of the investigated reservoirs, they could mostly (i.e., about 80% of all investigated sites) be used for HT-ATES with storage capacity, ΔE_{stor} above 2 GWh. Other promising sandstone layers and lenses occur in the Cenozoic successions of the URG, known from exploration drillings, that lack accumulation of hydrocarbons and therefore largely escaped detailed petrophysical investigations. Some of these sandstones most likely accumulated hydrocarbons in the past, but these previously accumulated hydrocarbons were probably 'flushed' away due to tectonic activities (Wirth, 1962).

The presented study could benefit from the large database of the abandoned oil reservoirs in the URG, comprising detailed petrophysical and stratigraphic information. However, the data from the hydrocarbon exploration and operation can partly not simply be transferred into a hydraulic-driven thermal storage system and seem to be most reliable for core measurements of the ambient rock. Future analyses should investigate (1) the impact of residual oil concentration in the reservoir on HT-ATES operation and efficiency, as well as (2) the influence of chemical reactions in the reservoir, e.g., dissolution/precipitation of mineral phases due to the injection of hot water and their influence on porosity/permeability. It is noteworthy to mention the applied simplifications concerning constant reservoir parameters and horizontal geometries, whereas our data compilation exhibits significant heterogeneities due to complex geological processes (Sauer et al., 1981). Herein, we quantified this impact in our sensitivity analysis, however, future applications have to investigate this effect further.

The results show that the storage capacity of HT-ATES in depleted oil reservoirs of the URG depends most sensitively on reservoir thickness, the applied injection/production flow rates, and the thermal conductivities of the reservoir caprock. The results identify the high recovery efficiency in HT-ATES in depleted oil reservoirs reaching values of >80%. Assuming the above-considered injection temperature, deeper, thus warmer, reservoirs would be even more efficient, and a further increase of the recovery factor by >5% can be expected. The numerical study demonstrated the benefit of operating a horizontal well orientation. Under these conditions, a considerable part of the reservoirs could be utilized in an economically viable manner. Not surprisingly, the deployment of advanced technologies such as directional drilling or geosteering promises optimum success. The order of magnitude of the estimated annual storage capacities of depleted oil reservoirs in the URG of up to 10 TWh represents a significant part of the thermal energy demand of the population in the URG. Furthermore, as numerical studies cannot replace the analysis of real systems, scientific demonstrators are needed for a proof of concept. For future economic use, further studies including life cycle analyses are essential.

ACKNOWLEDGEMENTS

We thank Ali Dashti (Karlsruhe Institute of Technology) and Jörg Meixner (Baden-Württemberg State Authority for Geology, Mineral Resources, and Mining) for their contributions in the early stages of this study as well as Katharina Schätzler (Karlsruhe Institute of Technology) for her assistance in the DeepStor project. The support from the Helmholtz program "Renewable Energies" under the topic "Geothermal Energy Systems" is thankfully acknowledged. The Helmholtz Climate Initiative (HI-CAM) is funded by the Helmholtz Association's Initiative and Networking Fund. The authors are responsible for the content of this publication. We further thank the EnBW Energie Baden-Württemberg AG for supporting geothermal research at KIT.

4

RISK OF SURFACE MOVEMENTS AND RESERVOIR DEFORMATION FOR HIGH-TEMPERATURE AQUIFER THERMAL ENERGY STORAGE (HT-ATES)

This chapter was published in Geothermal Energy 2024 12(4)
DOI: 10.1186/s40517-024-00283-9

ABSTRACT

High-temperature aquifer thermal energy storage (HT-ATES) systems are designed for seasonal storage of large amounts of thermal energy to meet the demand of industrial processes or district heating systems at high temperatures (> 100 °C). The resulting high injection temperatures or pressures induce thermo- and poroelastic stress changes around the injection well. This study estimates the impact of stress changes in the reservoir on ground surface deformation and evaluates the corresponding risk. Using a simplified coupled thermo-hydraulic-mechanical (THM) model of the planned DeepStor demonstrator in the depleted Leopoldshafen oil field (Upper Rhine Graben, Germany), we show that reservoir heating is associated with stress changes of up to 6 MPa, which can cause vertical displacements at reservoir depth in the order of 10^{-3} m in the immediate vicinity of the hot injection well. Both the stress changes and the resulting displacements in the reservoir are dominated by thermoelasticity, which is responsible for up to 90 % of the latter. Uplift at the surface, on the contrary, is primarily controlled by poroelasticity, resulting in displacements, which are two orders of magnitude smaller than at reservoir depth, reaching values of $<<10^{-3}$ m. Our calculations further show that the reservoir depth, elastic modulus, and injection/production rates are the dominant controlling parameters for the uplift, showing variations of up to two order of magnitudes between shallower reservoirs with low elastic moduli and deeper and more competent reservoirs. In addition, our findings demonstrate that the cyclic operation of HT-ATES systems reduces the potential for uplift compared to the continuous injection and production of conventional geothermal doublets, hydrocarbon production, or CO_2 storage. Consequently, at realistic production and injection rates and targeting reservoirs at depths of at least several hundred meters, the risk of ground surface movement associated with HT-ATES operations in depleted oil fields in, e.g., the Upper Rhine Graben is negligible.

4.1 INTRODUCTION

In the power sector, energy storage is gaining importance due to volatility of renewable energy sources (Lee, 2013; REN21, 2019). In the heat sector, seasonal variation in demand leads to large quantities of excess heat in summer, which can only be stored in the underground (Lee, 2013). Among other underground storage technologies (Yang et al., 2021), near-surface aquifer thermal energy storage (ATES) systems are widely used in the low-temperature sector. As of 2018, over 2800 systems were in operation worldwide, with an increasing trend (Fleuchaus et al., 2018). Process heat or water-based district heating with an inlet temperature of 80-130 °C require corresponding temperature levels and storage capacities for significantly larger amounts of thermal energy (Wesselink et al., 2018). So far, only a few HT-ATES systems are in operation, e.g., in Berlin and Neubrandenburg in northeast Germany (Holstenkamp et al., 2017) or in a demonstration phase, e.g., the Middenmeer project in the Netherlands (Dinkelman et al., 2022; Oerlemans et al., 2022).

Hydrocarbon reservoirs have favorable storage properties and ambient temperatures, as evidenced by decades of exploration, exploitation, and research in different geological settings, such as the Upper Rhine Graben (URG) in France, Germany, and Switzerland (Böcker, 2015; Stricker et al., 2020), clastic aquifers in the Netherlands (van Wees et al., 2017), or the Geneva basin in Switzerland (Moscariello, 2019). One challenge associated with their utilization for seasonal storage is the presence of residual hydrocarbon content. Insights can be drawn from the geothermal utilization of depleted reservoirs (Liu et al., 2015; Sui et al., 2019; Wang et al., 2016). Furthermore, compaction-induced subsidence is a well-documented phenomenon in hydrocarbon production (Geertsma, 1973; Nagel, 2001) and must also be considered for HT-ATES. In oil fields of the Upper Rhine Graben that are comparable to the targeted Leopoldshafen field, such as the Landau field, subsidence reached up to 7 mm a^{-1} during production between the 1950s and the 1990s, accumulating to about 17 cm (Fuhrmann, 2016). In addition, the risk of the reactivation of nearby faults and associated induced seismicity, which has been frequently observed for other utilizations of the subsurface, such as geothermal utilization or hydrocarbon production (Bourne et al., 2015; Zang et al., 2014), has to be addressed as well.

Concepts for ATES range from single-well systems (e.g., Jeon et al., 2015) to spatial patterns of multiple injection and production wells (e.g., Sommer et al., 2015). However, most ATES systems use the push-pull concept, in which excess heat is injected into the hot well of a doublet in summer and cold fluid is simultaneously produced from a second well. In winter, the system is operated in reverse (Jin et al., 2021; Kim et al., 2010). This concept is also used in the DeepStor demonstrator at the Karlsruhe Institute of Technology (Banks et al., 2021; Rudolph et al., 2022).

While single-well projects and multiple well patterns are prone to temporal mass unbalancing, which can cause differential vertical deformation, doublet operations ensure overall mass balancing at any time. Nevertheless, local mass imbalances between the injection and production areas remain and are investigated in this study. Previous research mainly focused on (i) uplift caused by poroelasticity for a single injection period (Birdsell and Saar, 2020), (ii) the influence of poro- and thermoelasticity on the storage efficiency (Jin et al., 2022, 2020), and (iii) the sensitivity of hydraulic parameters (e.g., the reservoir permeability) on the resulting uplift (Vidal et al., 2022).

Although these studies provide a good overview of the impact from seasonal ATES on ground surface displacements, they lack a fundamental understanding of the underlying processes and the influence of poro- and thermoelastic stress variations on the reservoir, nearby faults and resulting uplift. This is especially true for the sensitivity of other parameters, such as mechanical properties (e.g., elastic moduli), thermal properties (e.g. thermal conductivity), or the stress field. In addition, the geological and operational differences between ATES systems and other subsurface utilizations, such as deep geothermal and hydrocarbon operations, must be considered, as ATES systems are typically located at shallower depths and involve less competent rocks (Fleuchaus et al., 2018; Lee, 2010).

In this study, we use a thermo-hydraulic-mechanical (THM) model to investigate the impact of seasonal HT-ATES on the subsurface stress distribution and the resulting deformation at reservoir depth and the ground surface. We particularly focus on understanding the combined poro- and thermoelastic processes associated with the operation of HT-ATES systems in shallower depths and less competent rocks than comparable deep geothermal systems. Our objective is to perform a risk assessment of uplift for the DeepStor demonstrator, which includes a sensitivity analysis of reservoir and operational parameters.

4.2 NUMERICAL MODELING

This study uses the open-source code TIGER (THMC sImulator for GEoscientific Research; Egert et al., 2022; Gholami Korzani et al., 2020), which is based on the object-oriented framework MOOSE (Lindsay et al., 2022; Permann et al., 2020). TIGER has been successfully applied to simulate, for example, fluid flow in fractures (Egert et al., 2021), solute transport in fractured EGS reservoirs (Egert et al., 2020), heat storage (Stricker et al., 2020), and coupled mechanical processes (Egert et al., 2022). In Appendix C to this study, the results of the validation of poroelastic stress calculations in TIGER are provided. Therein, stress calculations in TIGER were compared with the analytical solution of Rudnicki (1986), following the procedure outlined in Altmann et al. (2010). For further insights into the implementation of the underlying continuum mechanics framework in MOOSE (Tensor Mechanics Module), we refer to the comprehensive documentation by INL (2023). This study extends previous heat storage simulations by considering coupled mechanical processes.

4.2.1 *Governing equations*

The equation for mass transport used to estimate the pore pressure, p, is given by the mass balance (Equation 4.1) along with the Darcy velocity, $\boldsymbol{q}$ (Equation 4.2; Bear, 1972):

$$S_m \frac{\partial p}{\partial t} + \nabla \boldsymbol{q} = Q \tag{4.1}$$

$$\mathbf{q} = \frac{\boldsymbol{k}}{\mu}(-\nabla p + \rho_f \boldsymbol{g}) \tag{4.2}$$

S_m is the mixture-specific storage coefficient of the medium; t is the time; Q is the source/sink term for injection and production, $\boldsymbol{k}$ is the permeability tensor, μ and ρ_f are the fluid dynamic viscosity and density, respectively, and $\boldsymbol{g}$ is the gravitational acceleration.

The solid and liquid phases are assumed to be in local thermodynamic equilibrium. Heat transport used to estimate temperature can be mathematically expressed using the advection-diffusion equation (Equation 4.3):

$$\rho c_p \frac{\partial T}{\partial t} - \boldsymbol{\lambda} \nabla^2 T + (\rho c_p)_f \boldsymbol{q} \nabla T = 0 \tag{4.3}$$

T is the temperature of the porous medium. ρc_p and $\boldsymbol{\lambda}$ are the heat capacity and thermal conductivity of the mixture, respectively. $(\rho c_p)_f$ represents the heat capacity of the fluid.

The deformation of a fully saturated porous medium is described by the momentum balance equation as follows for the form of effective stress (Equation 4.4; Jaeger et al., 2007):

$$\nabla \cdot (\boldsymbol{\sigma}' - \alpha p) + \rho_s \boldsymbol{g} = 0 \tag{4.4}$$

$\boldsymbol{\sigma}'$ is the effective stress tensor, α the Biot's coefficient, and ρ_s the solid rock density.

The constitutive law for stress-strain behaviour links the displacement vector $\boldsymbol{u}$, the primary variable solved for the deformation of the porous medium, to the effective stress tensor $\boldsymbol{\sigma}'$:

$$\Delta\boldsymbol{\sigma}' = \mathbb{C}(\Delta\varepsilon - \frac{1}{3}\beta_d \boldsymbol{I}\Delta T) \tag{4.5}$$

$$\varepsilon = \frac{1}{2}(\nabla\boldsymbol{u} + (\nabla\boldsymbol{u})^T) \tag{4.6}$$

$\mathbb{C}$ is the elastic material tensor, ε the strain, β_d the volumetric drained thermal expansion coefficient, $\boldsymbol{I}$ the identity matrix, and ΔT the temperature change. Here, we consider only isotropic, non-isothermal elastic deformation. Therefore, linear elasticity can be fully described by the generalized Hooke's law:

$$\mathbb{C} = \boldsymbol{\lambda}\delta_{ij}\delta_{kl} + 2\boldsymbol{\mu}\delta_{ik}\delta_{jl} \tag{4.7}$$

δ is the Kronecker delta, μ the shear modulus, and λ the Lamé constant.

4.2.2 *Numerical model*

As an example, we developed a simplified 3-D model of the potential DeepStor site to simulate coupled mechanical processes for high-temperature heat storage. The model extends over an area of 12.5 x 12.5 km from the ground surface to a depth of 2.2 km. It includes a 10-meter-thick reservoir at a depth of about 1200 m, over- and underlain by impermeable confining layers (Figure 4.1). The reservoir dips 5°to the East and resembles a typical setting within a graben block of the URG. The lateral extension of the model was chosen to avoid boundary effects, especially with regard to pressure propagation. Two vertical wells are located in the center of the model with a lateral spacing of 300 m to avoid thermal interference between them (e.g., Sommer et al., 2015). The unstructured mesh of the model consists of tetrahedral elements as well as 1D line elements to implement the borehole doublet. It was created using the Gmsh software (Geuzaine and Remacle, 2009). Element sizes vary from about 3 m along the two wells to 250 m at the upper and lower boundaries of the model. Further refinement was performed, where the highest gradients in the pressure, temperature, and displacement fields are expected, particularly around the two boreholes and above and below the near-borehole-areas in the caprock. A mesh sensitivity was performed to avoid any mesh dependency in the results. In total, the model consists of 171,346 nodes connected by 1,013,332 elements.

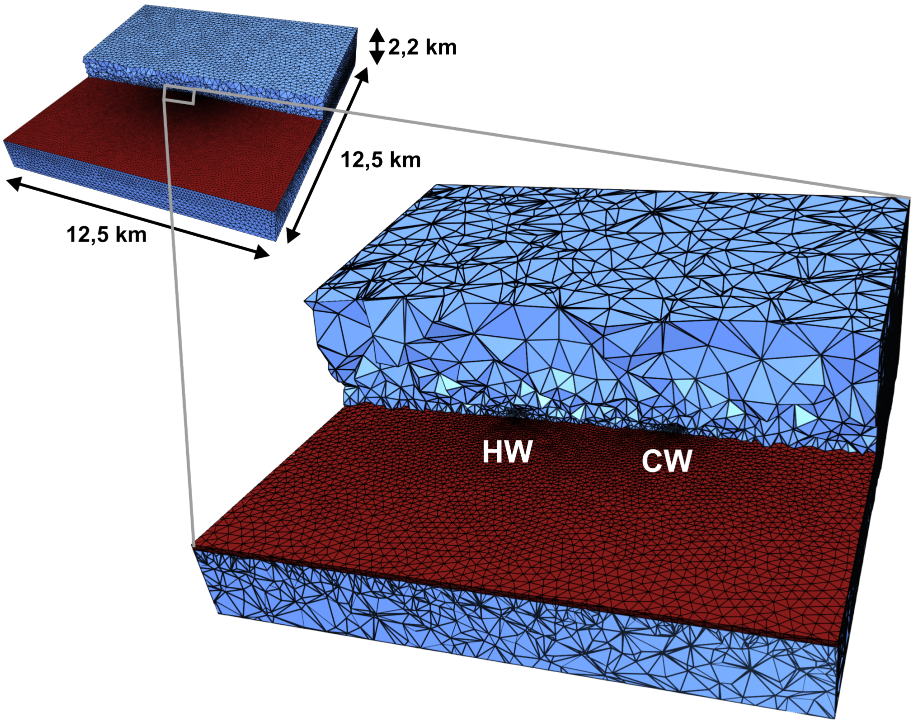

Figure 4.1: Simplified 3D mesh of the potential DeepStor demonstrator. The model consists of a 10-meter-thick reservoir (red) dipping 5°to the east, embedded into two impermeable confining layers (blue). The zoom shows the refined section of the model around the hot and cold wells (HW and CW, respectively).

Hydrostatic pore pressure is applied as a Dirichlet boundary condition at the top and bottom boundaries of the model, with the appropriate initial conditions applied to the entire model. No-flux Neumann boundary conditions are applied to the lateral boundaries of the model. Injection and production flow are implemented using time-dependent mass flux functions at the intersection of the top of the reservoir and the wells (corresponding to the beginning of the open hole section). These time-dependent functions represent simplified approximations of a real pumping operation, where an instantaneous reversal of the pumping direction is assumed at the end of each cycle. The temperature distribution within the model is based on a geothermal gradient of 50 K km^{-1} (Agemar et al., 2012) and is achieved by setting Dirichlet boundary conditions at the top and the bottom boundaries of the model and an associated initial condition applied to the entire model. To implement fluid injection at a given temperature into the two wells, nodal Dirichlet boundary conditions on top of the open-hole section are integrated and activated during the injection period of each well. No prior stress state is applied to the model, and the bottom and side boundaries of the model are fixed in normal directions by defining displacement-free Dirichlet boundary conditions (rollers). Gravity affects the pore pressure and effectives stress within the model.

A reference model (hereafter referred to as "reference case") was developed to investigate the general thermo-hydraulic-mechanical coupled behavior of the potential DeepStor demonstrator. The parameterization (Table 4.1) is based on average reservoir properties of (former) oil fields in the URG (Stricker et al., 2020).

Table 4.1: Parametrization of the reference model of the DeepStor site based on average reservoir properties of (former) oil fields in the URG, particularly the Leopoldshafen field (Banks et al., 2021; Stricker et al., 2020).

Parameter	Value
Reservoir permeability (m^2)	2.5×10^{-14}[b]
Permeability of the caprock (m^2)	10^{-18}[a]
Injection/production flow rate (Ls^{-1})	2[a]
Effective porosity of the reservoir (-)	0.15[b]
Effective porosity of the caprock (-)	0.01[a]
Thermal conductivity of the reservoir ($Wm^{-1}K^{-1}$)	2.5[b]
Thermal conductivity of the caprock ($Wm^{-1}K^{-1}$)	1.5[b]
Volumetric heat capacity of the reservoir ($MJm^{-3}K^{-1}$)	3.15[e]
Volumetric heat capacity of the caprock ($MJm^{-3}K^{-1}$)	3.30[e]
Thermal expansion coefficient (reservoir and caprock) (10^{-6} K^{-1})	10[f]
Injection temperature of the cold well (°C)	70[a]
Injection temperature of the hot well (°C)	140[a]
Young's modulus (reservoir and caprock) (GPa)	10[d]
Poisson's ratio (-)	0.3[d]
Fluid thermal conductivity ($Wm^{-1}K^{-1}$)	0.6[a]
Fluid specific heat capacity ($Jkg^{-1}K^{-1}$)	4200[a]
Fluid density (kgm^3)	1000[a]
Fluid dynamic viscosity (Pas))	4.18×10^{-4}[a]
Well diameter (m)	0.2159[a]

The data origin is marked with [a]our assumptions/simplifications, [b]data compilation of Stricker et al. (2020), [c]Scheck (1997) and Magri et al. (2005), [d]adapted from Marschall and Giger (2014) and Jahn et al. (2016), [e]Coker and Ludwig (2007), [f]Skinner (1966). The lithologies under- and overlying the reservoir were not individually parameterized; instead a homogeneous parameterization was used.

The seasonal storage operation consists of 6 months of continuous fluid injection at 140 °C into the hot well during summer (with the cold well acting as producer) and an inverted mode during winter, when water at 70 °C is injected in the cold well (with the hot well acting as producer). This seasonal storage operation is performed over a period of 10 years. In the following, the operation in summer will be referred to as “charging period”, whereas the operation in winter will be referred to as “discharge period”.

4.3 RESULTS

4.3.1 *Mechanical interaction of heat storage*

To improve the understanding of the coupled mechanical impact of one charging period (6 months), Figure 4.2 illustrates the three-dimensional distribution of the following parameters: (a) pressure, (b) temperature, (c) vertical stress, and (d) vertical strain. As the area of interest is primarily limited to the vicinity of the wells, only an excerpt with an extent of 1000 m x 1000 m x 300 m is shown, depicting the bottom surface of the reservoir in the foreground and a vertical section in the center of the model.

The pressure perturbation reaches up to 3.5 MPa at the injection and production wells, affecting a relatively large volume (Figure 4.2a). It attenuates to 0.1 MPa at a lateral distance of 800 m. Above and below the reservoir in the impermeable bedrock or caprock, this pressure perturbation nearly dissipates within 25 m (Figure 4.3a). In contrast, the temperature changes (Figure 4.2b) are confined to the vicinity of the injection well. Overall, a cylindrical volume in the reservoir is subject to temperature changes > 1 K within about 50 m around the hot well. Similar to the pressure perturbations, the thermal perturbations reach zero about 25 m above and below the reservoir (Figure 4.3b).

The vertical stress changes around the hot well are the superposition of injection-related poroelastic stress decrease and the thermoelastic stress increase. Figure 4.2c illustrates this variation as a spatially concentrated increase in the effective stress of up to ca. 1.9 MPa close to the hot well. A cylindrical volume within a distance of 50 m to the well is affected within the reservoir, resembling the observed temperature perturbations. Around this affected volume, the poroelastic stress reductions form a halo effect with extensional stresses of up to -1.2 MPa. At greater distances to the well, only the poroelastic stress decrease is remaining. In contrast, the vertical effective stress changes around the cold well are only affected by the production-related stress increase due to a decrease in pore pressure, reaching 2.3 MPa directly at the cold well. Above and below the reservoir, the vertical stress changes dissipate quickly, but do not reach zero within the same distance as pressure and temperature (Figure 4.3a). The horizontal stress changes are about four times larger in magnitude than the vertical stress changes and become negative directly above and below the reservoir before they also trend towards zero.

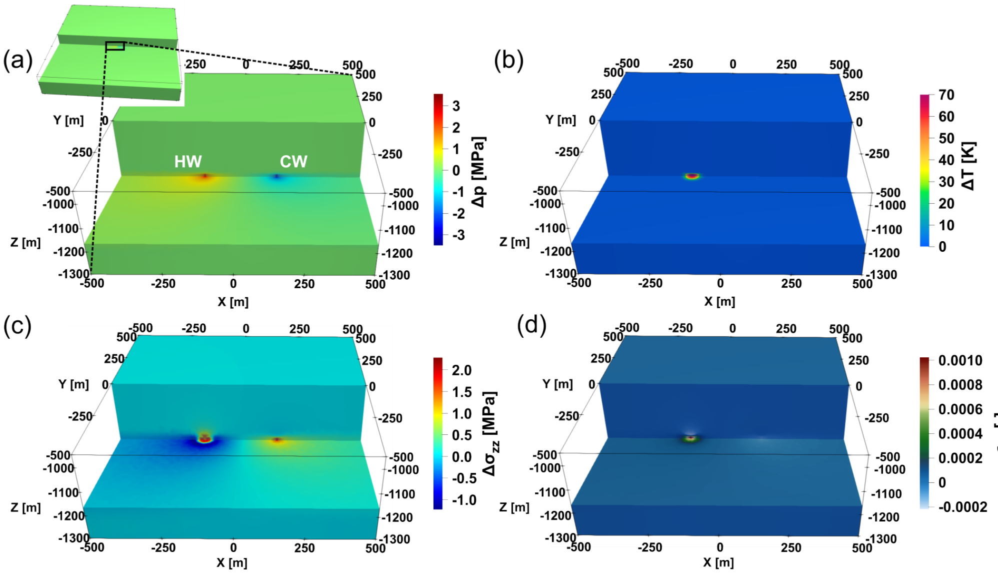

Figure 4.2: Perturbation of pressure (a), temperature (b), vertical stress (c), and vertical strain (d) in the center of the model near the well doublet (HW: hot well; CW: cold well) after one charging period (6 months). The figures have an extent of 1000 m x 1000 m x 300 m. (a) additionally shows the location of the displayed excerpt within the full model.

The superposition of poro- and thermoelasticity is also visible in the vertical strain (Figure 4.2d and Figure 4.3b), causing a vertical strain of about 10^{-3} due to the injection of hot water (pore pressure and temperature increase). At the cold well, negative strains of up to $-2x10^{-4}$ occur due to the production-related pressure reduction. However, the thermal expansion within the reservoir and the associated positive strain leads to negative strain directly above the reservoir due to the compression of the rock. At larger vertical distances from the reservoir, the vertical strain trends towards zero. The horizontal strain has a lower magnitude compared to the vertical strain and also dissipates towards zero over short vertical distances above and below the reservoir. The strain around the wells also has an impact on the porosity and permeability distribution. By applying the exponential strain-porosity relation developed in Chen et al. (2009), a relative porosity reduction of up to 0.5 % is determined around the hot well due to the occurring solid expansion, equaling an absolute change in the porosity of 0.00075 for a reservoir porosity of 0.15. These changes in porosity also have an influence on the permeability (e.g. Carman, 1937), translating in relative changes of approximately 1 % (equaling absolute changes of 2.5×10^{-16} m^2 for a reservoir permeability of 2.5×10^{-14} m^2. However, these small changes in reservoir porosity and permeability have a negligible impact on the storage operation itself as well and will thus not further be considered.

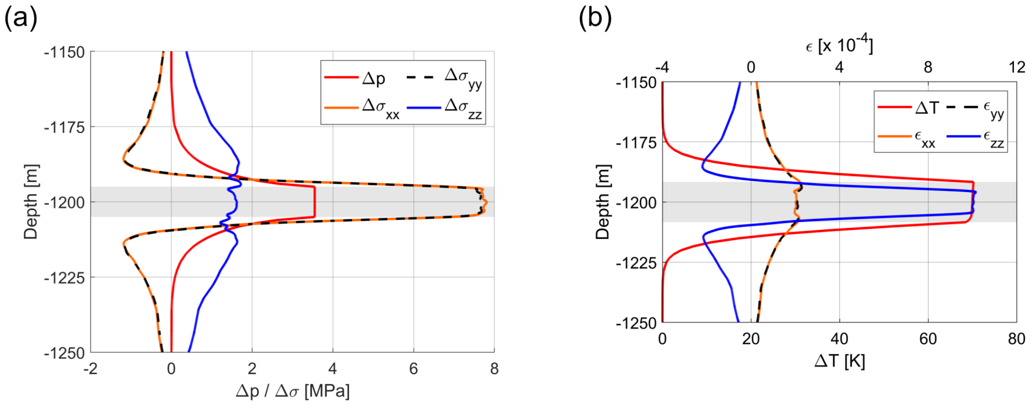

Figure 4.3: Distribution of the perturbation of pressure and the three principal stress components (a) as well as the temperature and the three principal strain components (b) above and below the reservoir (marked in grey).

To further analyze the mechanical response after one charging period, the vertical displacements (u_z) at the top of the reservoir and the ground surface were investigated. At the top of the reservoir, an injection-related u_z of up to 5.1 mm occurs, sharply limited to a radius of about 50 m around the hot well and reduces towards the model boundaries (Figure 4.4a). Only 1 % of the maximum u_z remains at a distance of about 800 m from the hot well. At the ground surface, only about 0.06 mm uplift (u_{z0}) remains, but it shows an impact on a larger area, with the uplift trending towards zero at distances greater than 3 km to the wells (Figure 4.4b). At the top of the reservoir around the cold well, a negative u_z of about -0.6 mm occurs. This negative u_z translates into an u_{z0} of ca. -0.05 mm at the ground surface, comparable to the u_{z0} above the hot well in both in magnitude and in extent.

The vertical displacements at the top of the reservoir and the ground surface are caused by the superposition of poro- and thermoelasticity, reflecting the stress and strain changes described above. To distinguish between the respective influences of poro- and thermoelasticity, a second purely poroelastic model was simulated. The comparison of this model with the reference case shows that 89 % of u_z at the top of the reservoir (about 4.6 mm) is related to thermoelasticity. However, its influence is limited to a radius of about 50 m around the hot well (difference between the black and the blue line in Figure 4.4c), resembling the thermal front of the hot water injection after six months. In contrast, poroelasticity – although it influences a larger rock volume – contributes only about 0.6 mm (or 11 %) of the total u_z at the top of the reservoir. Thus, at greater distances to the hot water injection well – and around the production well, where no temperature changes take place – u_z at reservoir depth is purely caused by poroelasticity. In contrast to the reservoir, the u_{z0} at the ground surface is strongly dominated by the poroelastic component (contributing up to ca. 92 % of u_{z0}), whereas the thermoelastic component is rather negligible (Figure 4.4d).

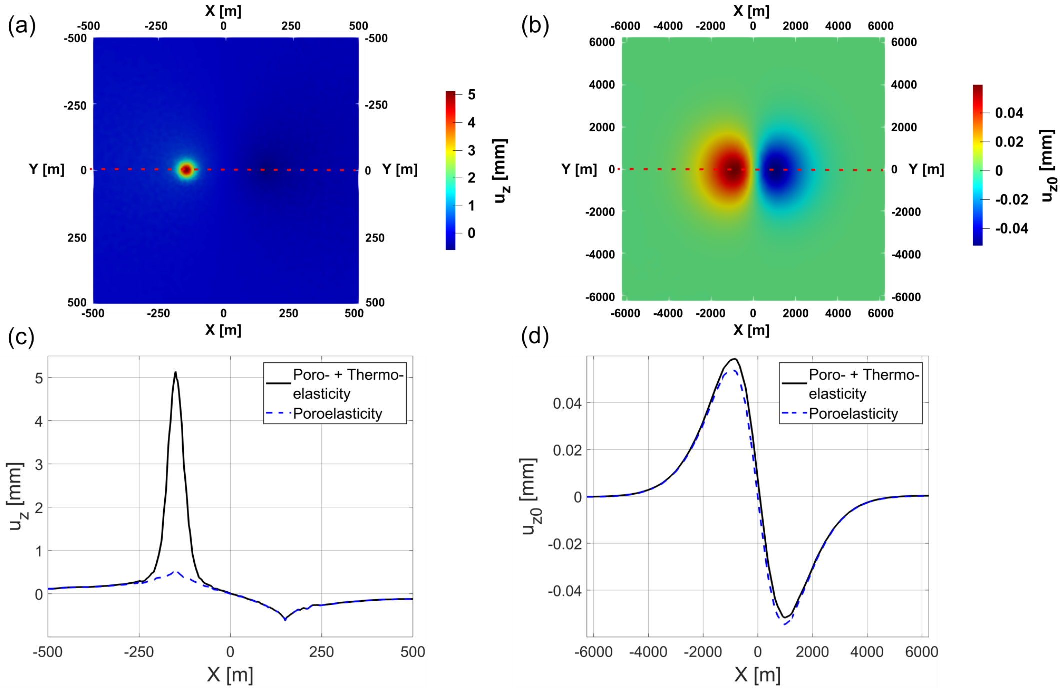

Figure 4.4: Distribution of the vertical displacement (u_z and u_{z0}, respectively) after one charging period at a) the top of the reservoir (1195 m depth) and b) the ground surface. Comparison of the displacement along the x-axis (at y = 0 m; dashed red lines in (a) and (b)) considering only poroelasticity (blue) and combining poro- and thermoelasticity (black) at the top of the reservoir (c) and the top of the model (ground surface; d). The different x-axis extents at reservoir depth (a and c) and the ground surface (b and d) correspond to the different scales of the involved physical processes at different depths.

This apparent contradiction between dominating thermoelasticity at reservoir depth and dominating poroelasticity at the ground surface can be explained by the different attenuation of the thermo- and poroelastic components of u_z from the top of the reservoir to the ground surface. Figure 4.5 illustrates that the higher thermoelastic component of u_z (red line) is caused by higher thermal vertical strain (ϵ_{zz}) above the reservoir due to strong thermal expansion of the rock matrix until about four meters above the top of the reservoir (dashed red line), where the highest u_z occurs. At greater vertical distances to the top of the reservoir, the rock matrix is compressed (negative ϵ_{zz}), subsequently resulting in a strong attenuation of the thermoelastic u_z.

In contrast, the rock (matrix and pore space) above the reservoir undergoes lower poroelastic ϵ_{zz} (dashed blue line in Figure 4.5), resulting in lower u_z (blue line). This subsequently leads to weaker compression of the overlying rock (negative ϵ_{zz}) and thus to less pronounced attenuation of the poroelastic component of u_z. In addition, the maximum of the poroelastic component of u_z (equal to the depth, where ϵ_{zz} = zero) is located further from the top of the reservoir than the maximum of the thermoelastic component (about 15 m compared to about 4 m). Because of the weaker attenuation of the poroelastic component of u_z, the poro- and thermoelastic components of u_z are equal at about 1100 m (about 90 m above the top of the reservoir), where the red and blue curve intersect. This leads to the poroelastic component being higher than the thermoelastic component in depths shallower than about 1100 m and accordingly dominating at the ground surface.

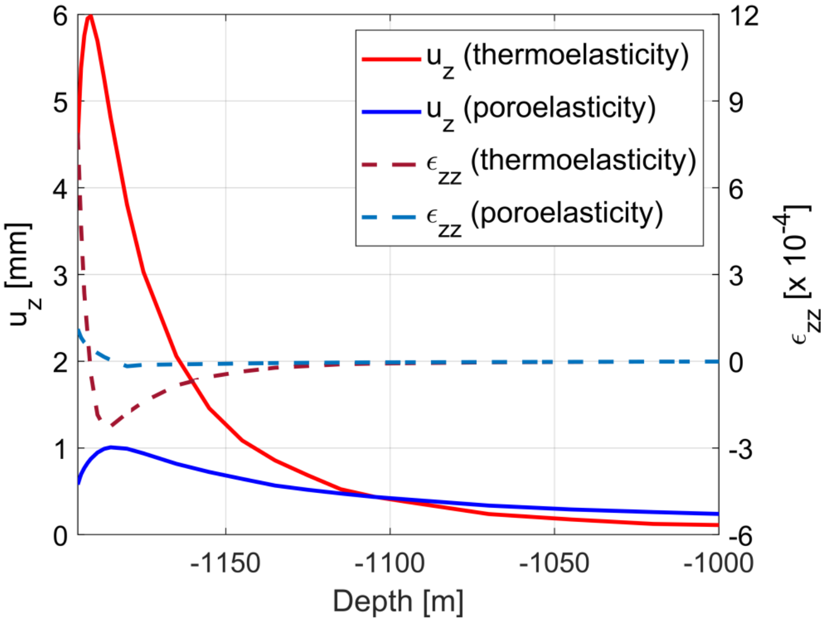

Figure 4.5: Vertical displacement (solid lines; left y-axis) and strain (dashed lines; right y-axis) variation from reservoir top at 1195 m to a depth of 1000 m.

4.3.2 *Temporal evolution*

In the following, we address the influence of seasonal charging and discharge cycles on stress changes within the reservoir, considering the different contributions of poro- and thermoelasticity. Figure 4.6a shows the vertical stress changes ($\Delta\sigma_{zz}$) after 6 months of injection into the hot well and production from the cold well (one charging period). The figure (as well as the other parts of Figure 4.6) shows an 1000 m x 1000 m excerpt at the top of the reservoir, where the most relevant changes in $\Delta\sigma_{zz}$ take place. At the hot well, the superposition of poro- and thermoelastic stress changes leads to an increase in $\Delta\sigma_{zz}$ of 1.8 MPa. Around the rock volume affected by the temperature change (sharply concentrated around the hot well with a radius of about 30 m), a halo effect of poroelastic stress reduction occurs, comprising a reduction in $\Delta\sigma_{zz}$ of 1.1 MPa, exceeding the expected reduction in $\Delta\sigma_{zz}$ for pure poroelasticity by 0.3 MPa. At greater distances from the hot well, only the pressure-induced reduction in $\Delta\sigma_{zz}$ remains and slowly dissipates towards the model boundaries. As a pressure-related reduction in the effective stress of about 0.02 MPa still occurs at a lateral distance of 1500 m, the spatial influence of poroelasticity exceeds that of thermoelasticity by nearly two orders of magnitude. At the cold well, in contrast, the production of water leads to a pressure-related increase in $\Delta\sigma_{zz}$ of ca. 2.0 MPa.

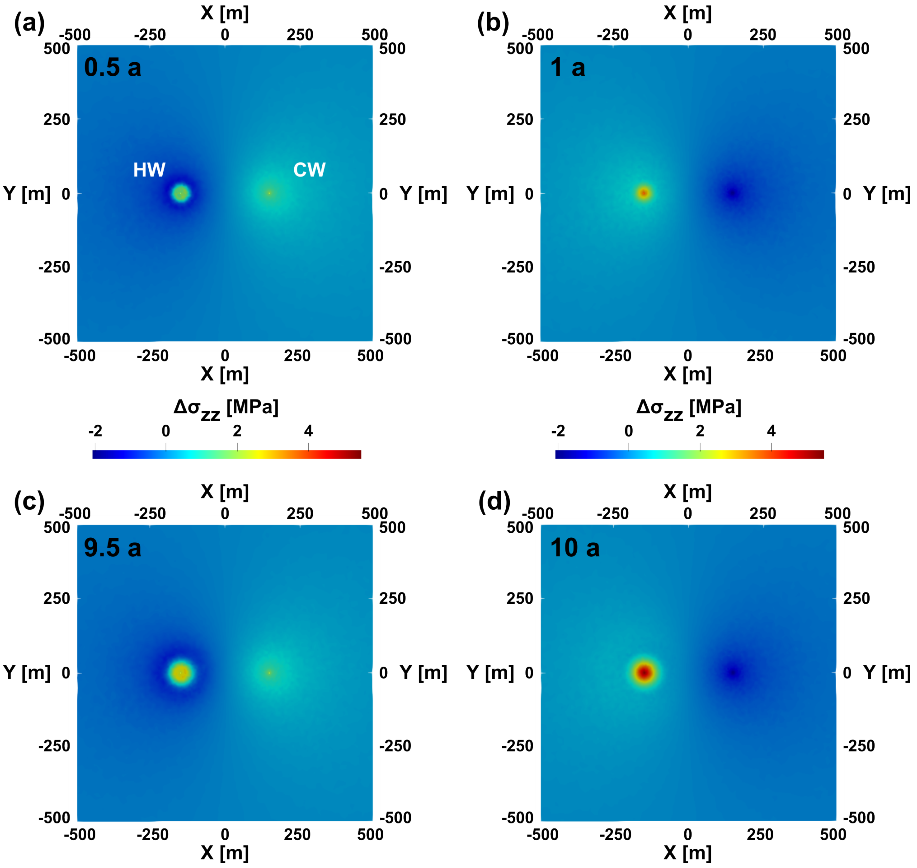

Figure 4.6: Distribution of stress changes at the reservoir top around the two wells (CW: cold well; HW: hot well) after (a) one charging period, (b) one full charging and discharge cycle, (c) the tenth charging period (i.e. after 9.5 years), and (d) the full simulation duration of ten charging and discharge cycles.

After a complete charging and discharge cycle (i.e., after 1 year), at the cold well an injection-related decrease in $\Delta\sigma_{zz}$ of -2.0 MPa occurs, equal to the production-related increase in $\Delta\sigma_{zz}$ (Figure 4.6b). At the hot well, the superposition of pressure reduction and residual heat leads to an increase in $\Delta\sigma_{zz}$ of about 3.9 MPa, significantly exceeding the reduction in $\Delta\sigma_{zz}$ around the cold well. At a distance of 35 m, still a stress increase of about 1 MPa occurs, representing the heat remaining in the reservoir after the discharge period.

After the tenth charging period (i.e., after 9.5 years), the heating of the reservoir over time leads to an increase in $\Delta\sigma_{zz}$ from 1.8 MPa (after the first charging period) to 2.3 MPa, and the radius of the affected rock volume increases from 30 m to 45 m. The stress reduction halo around the thermoelastically affected rock mass moves further away from the hot well (70 m compared to 45 m) and its absolute reductions in $\Delta\sigma_{zz}$ compared to pure poroelasticity increase from 0.3 MPa to 0.35 MPa. No changes occur at the cold well compared to the first cycle, as it is not influenced by thermoelasticity.

After the full simulation duration of ten charging and discharge cycles, a strong effect of reservoir heating is visible. The superposition of the production-related increase in effective stress and the stress increase due to thermal expansion of the rock matrix leads to a total increase in $\Delta\sigma_{zz}$ of 5.5 MPa (compared to 3.9 MPa after the first year; Figure 4.6d). In addition, a growing rock mass is affected by this increase in $\Delta\sigma_{zz}$, e.g., the distance in which a stress increase of 1 MPa can be observed increases from about 35 m to about 50 m. At the cold well, no changes occur compared to the situation after 1 year.

The changes in $\Delta\sigma_{zz}$ over time at the top of the reservoir caused by cyclic heat storage also impact u_z. Figure 4.7a illustrates the response of u_z to the cyclic changes of $\Delta\sigma_{zz}$ at the upper end of the open hole section of the hot well. The poroelastic component (blue curve in Figure 4.7a) stays constant over time because the increase and decrease in pore pressure due to injection and production do not change, resulting in equal changes in (effective) stress and strain and thus also in u_z. However, this does not apply to the thermoelastic component of u_z (red curve in Figure 4.7a). It can be observed that u_z at the end of each charging period (local maxima of u_z) decreases from 4.6 mm after the first period to 4.2 mm after the tenth period. In contrast, the remaining u_z after each subsequent discharge period (local minima of u_z) increases from 1.3 mm after the first period to 2.1 mm after the tenth period.

The decrease of u_z at the end of each charging period over time can be explained by the gradual heating of the reservoir. With each charging period, this heating causes the temperature front to propagate further into the cap rock above and below. As a result, the temperature gradient between the reservoir boundaries and the cap rock above and below decreases. This leads to lower thermal strains (Figure 4.7b) and consequently reduced u_z at the upper end of the open hole section of the hot well over time. The increase in u_z after each discharge period can also be explained by the gradual heating of the reservoir due to diffusive heat losses around the hot well, as water with a temperature exceeding the ambient reservoir temperature is stored (e.g. Kim et al., 2010; Stricker et al., 2020). Figure 4.7b further shows that the temperature front propagating away from the reservoir (and thus also the moving thermal strain front) leads to a flattening of the strain rate (orange curves in Figure 4.7b) over time. This causes an accumulation of strain and thus an increasing maximum of u_z (black curves in Figure 4.7b). In addition, the maximum of u_z moves further away from the reservoir as a consequence of the moving thermal strain front.

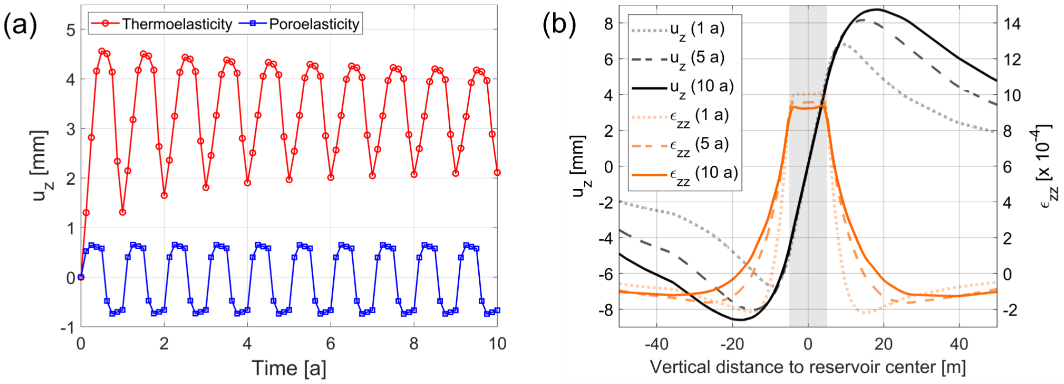

Figure 4.7: (a) Development of the vertical displacement at the intersection between the top of the reservoir and the hot well over time. Blue curve: poroelastic component, red curve: thermoelastic component. (b) Distribution of the vertical displacement (black curves) and strain (orange curves) around the reservoir (highlighted area in light grey) over time (for combined poro- and thermoelasticity).

4.4 RISK ASSESSMENT OF UPLIFT AT THE GROUND SURFACE

The results presented in chapter 3.1 have shown that the uplift at the ground surface (u_{z0}) is predominantly influenced by poroelasticity and subordinately by thermoelasticity. Therefore, parameters that influence either the hydraulics in the reservoir (such as the reservoir permeability or the injection/production flow rate) or the mechanical response of the rock (such as the Young's modulus or the Poisson's ratio) are very likely to have the strongest influence on u_{z0}. In the following, we focus on these parameters, complemented by the injection temperature difference, the thermal expansion coefficient, and the reservoir depth (Table 4.2).

Figure 4.8 shows the results of the performed parameter sensitivity analysis. The strongest influence is exerted by the reservoir depth (dashed black line), with an increase in u_{z0} of about one order of magnitude for a reduction in reservoir depth from 1600 m to 400 m. A decrease in the Young's modulus (green line) from 25 GPa to 2.5 GPa also leads to an increase in u_{z0} of nearly one order of magnitude. The injection/production flow rate (red line) has a linear influence on u_{z0}, with a fivefold increase in u_{z0} for an increase in the flow rate from 1 to 5 Ls^{-1}. The large influence of these three parameters is related to not only their relative impact (slope of the curves) but also the large potential variation of the parameters themselves. The other four parameters do not exert a significant influence on u_{z0}.

Table 4.2: Selected ranges of identified geological and operational parameters to determine their influence on the uplift at the ground surface (u_{z0}).

Parameter	Range	
	Min	Max
Reservoir permeability[b] (m^2)	1.0×10^{-14}	5.0×10^{-14}
Injection/production flow rate[a] (Ls^{-1})	1	5
Young's modulus[c,d,e] (GPa)	2.5	25
Poisson's ratio[c,d] (-)	0.25	0.35
Injection temperature difference[a] (K)	30	90
Thermal expansion coefficient[f] (10^{-6} K^{-1})	8	12
Reservoir depth[b] (m)	400	1600

The data origin is marked with [a]our own assumptions/simplifications, [b]data compilation of Stricker et al. (2020), [c]Marschall and Giger (2014), [d]Jahn et al. (2016), [e]Egert et al. (2018), and [f]Skinner (1966).

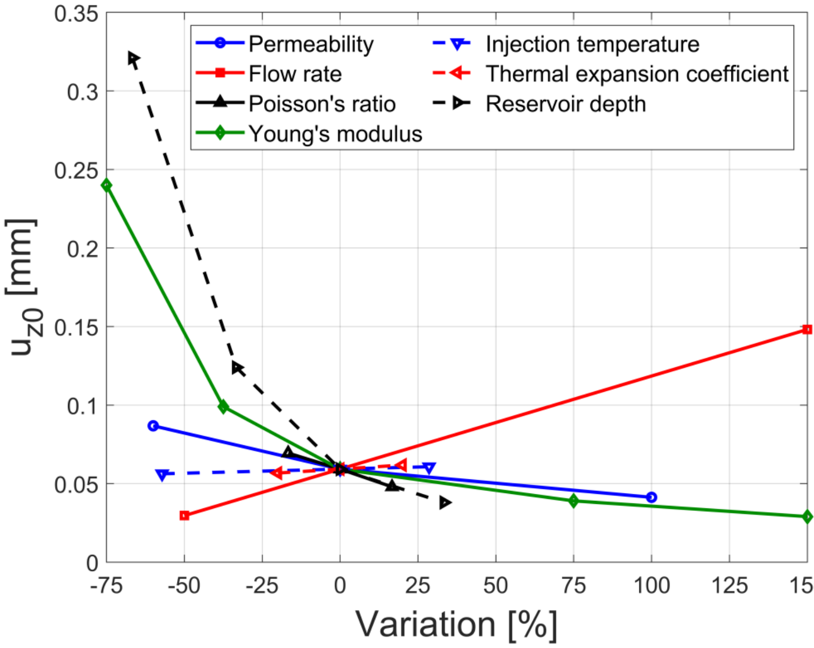

Figure 4.8: Sensitivity analysis on the parameter influence on u_{z0} after the first charging period at the hot well. The shown changes refer to the reference case.

Due to the strong non-linearity of the relationship between both reservoir depth and Young's modulus with u_{z0}, high values of u_{z0} (superimposed by the linear influence of the flow rate) can be expected for shallow reservoirs with low Young's moduli. To investigate this behavior more thoroughly, we simulated a range of models that vary the reservoir depth between 400 m and 1600 m (shallow and deep oil reservoir in the URG, respectively; Stricker et al., 2020) and the Young's modulus ranging between 2.5 GPa (weak claystone; Jahn et al., 2016; Marschall and Giger, 2014) and 25 GPa (strong sandstone; Egert et al., 2018). All other parameters used in these simulations were the same as in the reference case. Figure 4.9 illustrates the strong dependency of u_{z0} on the two parameters with variations between 0.02 mm for a deep reservoir with a high Young's modulus (comparable to the parametrization of a (medium) deep geothermal system) and 1.18 mm for a shallow reservoir with a low Young's modulus, comprising a variation in u_{z0} of nearly two orders of magnitude. The curved shapes of the isolines in Figure 4.9 further illustrate the non-linear relationship between the two varied parameter and u_{z0}.

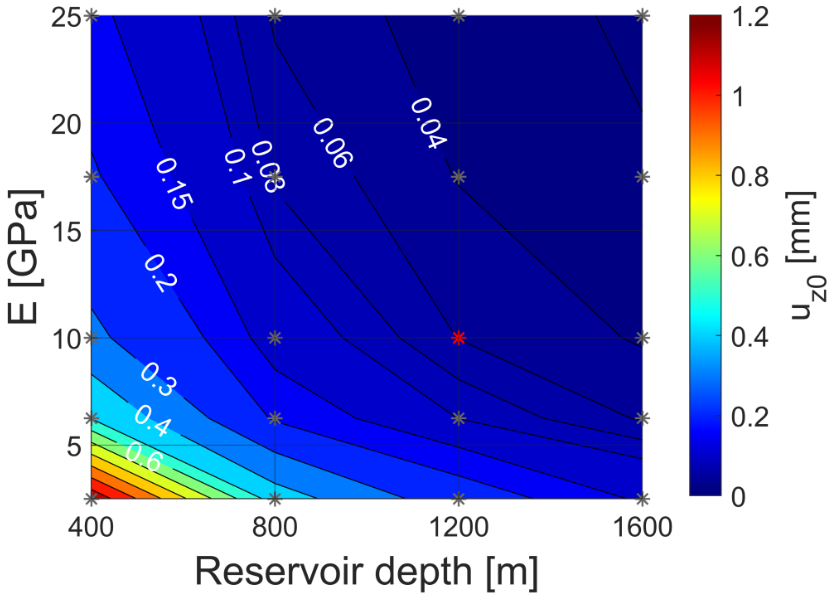

Figure 4.9: Contours of the maximum uplift after one charging period for different reservoir depths and Young's moduli (E). The grey asterisks show the simulations, intermediate results are interpolated. The red asterisk represents the reference case.

The strong variations in u_{z0} observed in HT-ATES are caused by the superposition of two processes. First, the poroelastic component of u_{z0} decreases with depth, because the dominant poroelastic component of u_z (ca. 0.6 mm for all reservoir depths) is attenuated towards the ground surface as the path length increases. This finding aligns with earlier results by Birdsell and Saar (2020), but contradicts the results of Vidal et al. (2022), who simulated counterintuitively increasing vertical displacements towards the ground surface due to their choice of boundary conditions. This is particularly evident in the employment of zero vertical displacement boundary conditions at the lateral boundaries of the model by Vidal et al. (2022) in addition to rollers only (as used in this study and also, for instance, in Birdsell and Saar (2020)). In addition, the limited lateral extent of the model (200 m in contrast to approximately 6 km in this study) may influence the results. An optimized choice thereof may lead to different results in alignment with this study or the results of Birdsell and Saar (2020). Second, an increase in the Young's modulus leads to a lower u_z in the reservoir, varying between 0.2 mm for a Young's modulus of 25 GPa and 2.9 mm for a Young's modulus of 2.5 GPa (both for the depth of the reference case of 1200 m). This variation in u_z at reservoir depth propagates towards the ground surface and contributes to the described variation of u_{z0}. Consequently, this means that heat storage operations in rather shallow and mechanically incompetent rocks pose much smaller risk for ground surface deformation than deep geothermal operations in more competent reservoir rocks, such as granite or sandstone (Békési et al., 2019; Frey et al., 2022; Heimlich et al., 2015).

Although the thermoelastic component of u_{z0} increases by one order of magnitude from 0.003 to 0.025 mm for a reduction of the reservoir depth from 1600 m to 400 m, this increase remains negligible compared to the increase in the poroelastic component from 0.035 to 0.30 mm. This indicates that the contribution of the poroelastic component on u_{z0} is one order of magnitude higher than the thermoelastic component irrespective of the reservoir depth, matching previous observations of Vidal et al. (2022). Therefore, it can be concluded that the high injection temperatures of HT-ATES systems do not pose a significant additional risk factor regarding uplift.

Ground surface movements around a seasonal heat storage site may be monitored using the same methods as those used for oil production or geothermal utilization, such as global navigation satellite systems (GNSS) or interferometric satellite radar data (InSAR) (Fuhrmann, 2016; Heimlich et al., 2015). However, even the highest simulation results of u_{z0} (ca. 1 mm) for very shallow reservoirs with low Young's moduli are approximately one order of magnitude smaller than observations in the vicinity of the Landau oilfield in the URG, where ground surface movements of up to 7 mma^{-1} occurred and accumulated over several decades of production to ca. 17 cm (Fuhrmann, 2016). This is because, unlike the continuous injection and/or production of deep geothermal, hydrocarbon exploitation, and CO_2 storage, seasonal heat storage involves cyclical injection and production, which prevents the accumulation of uplift over time.

In summary, the operation of HT-ATES systems in depleted oil reservoirs in the Upper Rhine Graben is expected to only have a minor influence on u_{z0}, with a very low risk for damage to structures at the ground surface, such as buildings. More significant u_{z0} of more than 1 mm (albeit with very low differential displacements) can only occur for very shallow and mechanically weak reservoir (and surrounding) rocks, and can be avoided by selecting a suitable reservoir.

In addition, the high sensitivity of u_{z0} to injection and production flow rates does not pose a significant risk to HT-ATES operations, as the flow rates in these systems are usually much smaller (i.e. < 5 Ls^{-1}) than in deep geothermal systems with up to > 100 Ls^{-1} (Evans et al., 2012).

4.5 CONCLUSIONS

As part of a risk assessment, we used coupled thermo-hydraulic-mechanical modeling to investigate the (geo-)mechanical sensitivity of HT-ATES systems to poro- and thermoelastic stress development. Our modeling results show that the displacements caused by the cyclic heat storage operation occur close to the hot well at reservoir depth, reaching up to 6 mm. Towards the ground surface, the displacements are strongly attenuated by two orders of magnitude. While the displacements in the reservoir are dominated by small-scale thermoelasticity, the related uplift and subsidence at the ground surface are predominantly related to poroelasticity due to the stronger attenuation of the thermoelastic component.

The primary factors influencing ground surface deformation in HT-ATES systems in shallow depleted oil reservoirs in settings such as continental rift systems (e.g. the Upper Rhine Graben; URG) are reservoir depth, Young's modulus, and injection/production flow rates. In contrast to deep geothermal reservoirs, shallow, soft reservoirs with high injection and production flow rates are likely to cause greater ground surface deformation. Therefore, the impact of ground surface deformation can be reduced by choosing suitable reservoir conditions and operational framework. For example, HT-ATES systems typically use lower flow rates than deep geothermal systems. In addition, the cyclic operation of an HT-ATES has a smaller impact on ground surface deformation than typical continental shallow oil production or CO_2 storage in comparable depths as no significant accumulation of uplift or subsidence occurs over time. Ground surface monitoring systems can be used to investigate ground movements at a particular storage site. The highest impact is to be expected in the area above the boreholes, allowing for a relatively simple monitoring layout.

Former oil reservoirs in the URG, such as the planned scientific demonstrator project DeepStor, are considered to be ideal for use as HT-ATES systems. They are expected to be too shallow to pose a high risk of induced seismicity (due to limited hydraulically connection to larger critically stressed faults) and simultaneously deep enough to avoid a high risk of uplift or subsidence. However, future investigations of HT-ATES systems should aim to assess their specific risk of fault reactivation and induced seismicity due to the cyclically stress changes. Beyond purely elastic modeling, more sophisticated modeling approaches, such as damage or phase-field modeling may be considered, particularly to analyze the influence on changes in porosity and permeability. Further studies may also investigate the risk of damaging the cementations of the wells due to the cyclic mechanical loading.

ACKNOWLEDGEMENTS

This work was partly supported by the German Federal Ministry for Economic Affairs and Climate Action (BMWK) and the Project Management Jülich (PtJ) under the grant agreement number 03EE4008C associated with the INSIDE project (https://inside-geothermie.de/en/inside-en/). This study is part of the subtopic "Geoenergy" in the program "MTET - Materials and Technologies for the Energy Transition" of the Helmholtz Association. The authors are responsible for the content of this publication.

5

RISK ASSESSMENT OF FAULT REACTIVATION AND INDUCED SEISMICITY FOR HIGH-TEMPERATURE HEAT STORAGE (HT-ATES) AT THE DEEPSTOR DEMONSTRATOR IN THE UPPER RHINE GRABEN

This chapter is in preparation for submission to Geothermics.

ABSTRACT

A risk assessment of fault reactivation and induced seismicity has been conducted for the planned high-temperature aquifer thermal energy storage (HT-ATES) demonstrator DeepStor in the depleted Leopoldshafen oil field (Upper Rhine Graben, Germany). We employed a thermo-hydraulic numerical model and semi-analytical stress calculations to show that injection-induced stress changes only lead to a minor de-stabilization of faults in the vicinity of the HT-ATES doublet, whereas the heating of the reservoir over time results in counteracting thermoelastic stress changes, stabilizing the fault.

We have followed two approaches to investigate the hazard of fault failure. In the first one, we modeled an unstressed fault, with a risk assessment based on the slip tendency distribution at the fault In the second, we used a nearly critically stressed fault and focused on the sensitivity of changes in the Coulomb stress at the fault. Depending on the friction angle of the fault, critical slip tendencies may be reached for 10 % (friction angle of 30°) to 54 % (friction angle of 20°) of the conducted simulations, highlighting that potential risks are associated with rather unfavorable reservoir properties and operational choices. For both approaches, the orientation and gradients of the stress field exert a significant influence on potential failure. However, the risk of fault reactivation and induced seismicity in the studied HT-ATES systems is minor.

5.1 INTRODUCTION

To address global warming, greenhouse gas emissions have to be reduced across all sectors by reducing fossil fuel consumption and increasing the share of renewable energy sources (IPCC, 2022). The increasing share of renewable energies, however, leads to a mismatch between peak energy demand in winter (especially for heating) and the highest renewable energy supply in summer (Dinçer and Rosen, 2011; IEA, 2023). In this context, the demand for energy storage is expected to rise (Lee, 2013; REN21, 2022). Subsurface heat storage, specifically aquifer thermal energy storage (ATES), can provide the required storage capacities for large-scale energy storage (Lee, 2013). The majority of ATES systems (around 3000 worldwide, predominantly in the Netherlands), however, operate in shallow aquifers with low injection temperatures of less than 30 °C, mainly covering the heat demand of greenhouses or domestic heating (Fleuchaus et al., 2018). To expand their applicability to district heating networks and industrial processes, ATES systems require higher operating temperatures, necessitating higher storage depths and reservoir temperatures (Wesselink et al., 2018). However, only a small number of high-temperature (HT) ATES systems are currently in operation (Holstenkamp et al., 2017) or in demonstration phases (Dinkelman et al., 2022; Oerlemans et al., 2022), underscoring the need for further research in this area.

Eight research institutions from Germany, Switzerland, and the USA are presently collaborating within the VESTA project to address the challenges of HT-ATES (Bremer et al., 2022). One of the pilot projects within VESTA is the proposed large-scale Helmholtz infrastructure DeepStor, which aims to provide a scientific proof of concept for the utilization of former oil reservoirs for HT-ATES, acting as a bridging technology towards sustainable subsurface utilization (Banks et al., 2021; Rudolph et al., 2022). The infrastructure will be located in the Upper Rhine Graben, approximately 10 km north of Karlsruhe, at one of the campuses of the Karlsruhe Institute of Technology (Bremer et al., 2022). It will be strategically positioned directly atop Germany's largest geothermal anomaly (Baillieux et al., 2013).

Previous research on HT-ATES has primarily addressed aspects such as its technical feasibility (e.g. Stricker et al., 2020, see Chapter 3), recovery efficiency (e.g. Gao et al., 2019) and the hazard of potential surface movements (Birdsell and Saar, 2020; Stricker et al., 2024; Vidal et al., 2022, see Chapter 4). Unlike for other forms of subsurface utilization, such as geothermal heat and power production (Buijze et al., 2019; Zang et al., 2014), hydrocarbon production (Suckale, 2009; van Wees et al., 2014; van der Baan and Calixto, 2017), waste water injection (Keranen et al., 2013) or CO_2 storage (Rutqvist et al., 2016; Vilarrasa et al., 2019), there is a lack of research investigating the potential hazard of induced seismicity associated with HT-ATES operations.

Several potential mechanisms were identified as root causes of induced seismicity, which may also have implications for the operation of HT-ATES systems and warrant further investigation (Buijze et al., 2019; Doglioni, 2018; Gaucher et al., 2015). These include:

(i) Reservoir compaction due to fluid removal (i.e. production), which can result in the reactivation of faults and subsequent seismicity.

(ii) Pore pressure increase (and associated poroelastic stressing) due to fluid injection, which reduces the effective normal stress on the fault, making it more prone to failure.

(iii) Thermoelastic stress changes due to fluid injection with a different temperature than the ambient reservoir temperature.

In contrast to other forms of subsurface utilization, HT-ATES systems are typically associated with smaller pressure perturbations (e.g. Birdsell et al., 2021), increasing instead of decreasing temperatures (Wesselink et al., 2018), and do not require extensive flow paths in the subsurface (i.e. targeting shallower sedimentary aquifers instead of fault systems; Fleuchaus et al., 2020). These factors suggest that the potential hazard of induced seismicity from HT-ATES operations may be lower than from other forms of subsurface utilization. However, it is still important to conduct specific risk assessments of storage systems that consider the specific framework conditions and their influence on the physical processes associated to HT-ATES.

This study presents a specific risk analysis for HT-ATES operations, focusing on the DeepStor project in the Upper Rhine Graben near Karlsruhe. An available subsurface model, derived from a seismic survey, is the basis for the thermo-hydraulic model employed in this study. Building upon the simulation results, a semi-analytical approach is employed to calculate the stress changes on a fault plane positioned near the planned well doublet of the DeepStor project. To assess the influence of various reservoir and operational parameters on the risk of fault reactivation and induced seismicity, a parameter sensitivity and a Monte Carlo analysis are conducted.

5.2 THE DEEPSTOR HIGH-TEMPERATURE HEAT STORAGE (HT-ATES) DEMONSTRATOR

5.2.1 *Geology of the study area*

The study area is located in the central segment of the Upper Rhine Graben (URG). The URG is a 300 km long, NNE-SSW-trending continental rift system. Since the onset of the graben formation 47 Ma ago, it has accumulated up to 3.5 km of Cenozoic sediments (Geyer et al., 2011). A comprehensive review of the URG's geological development can be found in Grimmer et al. (2017) and references therein.

A wide range of Cenozoic sediments in the URG have been explored and exploited for oil production since the 1930s (LBEG, 2022; Reinhold et al., 2016). These reservoir rocks include Late Eocene to Early Oligocene lacustrine-brackish and marine sandstones from the Pechelbronn Group (Reinhold et al., 2016), Early Oligocene brackish-marine sandstones from the Froidefontaine Formation (Böcker, 2015), and Late Oligocene lacustrine-fluviatile sandstones from the Niederrödern Formation (Sauer et al., 1981). The depths of these reservoir rocks range from the surface to approximately 2000 m (Sauer et al., 1981).

The target rocks of this study are water-bearing sandstones in the marine upper Meletta beds (part of the Froidefontaine formation) at the rim of the abandoned Leopoldshafen oil field. The upper Meletta beds typically comprise 5-15 m thick fine-grained, calcareous sand layers deposited during short regression phases (Pirkenseer et al., 2011). Low-permeable clay-rich beds are interbedded with these sand layers (Sauer et al., 1981). The former oil reservoir is located in a graben block between two normal faults. To the west, it is bounded by the Leopoldshafen fault, which acted as structural trap for the oil reservoir. The Stutensee fault forms the eastern boundary of the graben block. Additionally, several antithetic faults compartmentalize the graben block (Wirth, 1962).

The Cenozoic graben filling sediments are strongly influenced by deep-reaching thermal anomalies caused by fault-controlled convective fluid flow within the crystalline basement and Mesozoic sediments (Bächler et al., 2003; Baillieux et al., 2013), leading to elevated geothermal gradients between 35 K km^{-1} and 58 K km^{-1}, locally reaching up to 100 K km^{-1} (Agemar et al., 2012; Sauer et al., 1981). These elevated gradients result in temperatures of up to 140 °C in 2 km depth (Baillieux et al., 2013; Pribnow and Schellschmidt, 2000), creating very favorable conditions for geothermal utilization (e.g. Bresee, 1992; Maurer et al., 2020) and HT-ATES (e.g. Stricker et al., 2020).

5.2.2 *The DeepStor infrastructure*

The DeepStor demonstrator is a planned scientific infrastructure for investigating high-temperature aquifer thermal energy storage (HT-ATES). It will be constructed approximately 10 km north of Karlsruhe at one of the campuses of the Karlsruhe Institute of Technology. The demonstrator aims to demonstrate the feasibility of heat storage at temperatures exceeding 100 °C in former oil reservoirs, utilizing Germany's largest temperature anomaly. The Cenozoic sandstones of the Meletta beds are envisaged as the target reservoir formation (Bremer et al., 2022). A primary objective of the DeepStor demonstrator is to validate previously conducted numerical studies (Banks et al., 2021; Stricker et al., 2020) by investigating reservoir properties using experimental approaches. Additionally, the demonstrator aims to provide proof-of-concept for HT-ATES in Cenozoic sandstone reservoirs, enabling knowledge transfer to future projects (Bremer et al., 2022).

5.3 NUMERICAL MODELING

5.3.1 *Governing equations*

The equations used in the thermo-hydraulic modeling of this study and their derivations are presented in detail in textbooks so that we only give a brief overview here. The thermal transport equation, which is used to estimate the temperature, T, can be expressed as follows (Gholami Korzani et al., 2020; Kohl and Hopkirk, 1995):

$$\rho c_p \frac{\partial T}{\partial t} = \nabla \cdot (\boldsymbol{\lambda} \cdot \nabla T) - (\rho c_p)_f \boldsymbol{q} \nabla T \tag{5.1}$$

ρc_p and $\boldsymbol{\lambda}$ are the bulk volumetric heat capacity and thermal conductivity of the porous rock, respectively. $(\rho c_p)_f$ represents the volumetric heat capacity of the fluid. The advective velocity, $\boldsymbol{q}$, is a result of fluid flow in pores or fractures, which strongly affects the temperature distribution (e.g. Guillou-Frottier et al., 2013). Fluid flow can be described by the Darcy flow equation (Bear and Cheng, 2010):

$$\mathbf{q} = \frac{\boldsymbol{k}}{\mu}(-\nabla p + \rho_f \boldsymbol{g}) \tag{5.2}$$

$\boldsymbol{k}$ is the permeability tensor, μ is the fluid dynamic viscosity, ρ_f is the fluid density, and $\boldsymbol{g}$ is the gravitational acceleration.

The TNO in-house modeling framework ROSIM was deployed for the numerical simulation. ROSIM enables the construction of static 3D geological subsurface models and integrates the thermo-hydraulic solver DoubletCalc3D, which implements the governing equations above (Dinkelman et al., 2022; Lipsey et al., 2016). DoubletCalc3D is a single phase flow simulation tool that enables the numerical simulation of pressure and temperature evolution of geothermal doublet and ATES systems. It employs a staggered coupling approach, combining a steady state solution for the pressure and flow field with a transient solution of the temperature field. Both the flow and the temperature field are solved using a finite volume formulation (Lipsey et al., 2016; Pluymaekers et al., 2016).

5.3.2 *Conceptual model*

The conceptual model of our study has been derived from the interpretation of a 3D seismic survey, encompassing the area of interest, a graben block between two major normal faults (Leopoldshafen and Stutensee faults). The graben block is further compartmentalized by several antithetic faults. We built the conceptual model using the Petrel® software to assess the influence of the HT-ATES operation in the DeepStor project on the fault of interest (Leopoldshafen fault). This model encompasses an excerpt of the interpreted seismic survey, spanning approximately 5.5 km x 6.5 km (Figure 5.1). The lateral extent of the model was chosen to minimize boundary effects on the area surrounding the fault of interest. The antithetic faults within the graben block were excluded due to their negligible influence on the pressure and temperature field. Vertically, the model extends approximately 500 m, encompassing the 10 m-thick reservoir in the Meletta layers as well as confining layers above and below. Two vertical wells are positioned adjacent to the Leopoldshafen fault, with varying distances ranging from 10 m to 1000 m. This study solely considers vertical wells to simulate the maximum pressure build-up on the fault of interest, which represents the highest risk of de-stabilization or reactivation compared to inclined or horizontal wells.

In this study, a structured hexahedral mesh was created using Petrel®, followed by further refinement in ROSIM. The mesh resolution ranges from 2 m to 150 m, both for its lateral and vertical extent. The refinement focuses on the vicinity of the wells and the reservoir layer, as in these parts of the model the most significant gradients in pressure and temperature are expected to occur. A mesh sensitivity analysis was conducted to ensure that the simulation results are independent of the mesh resolution. In total, the mesh consists of 145,926 elements.

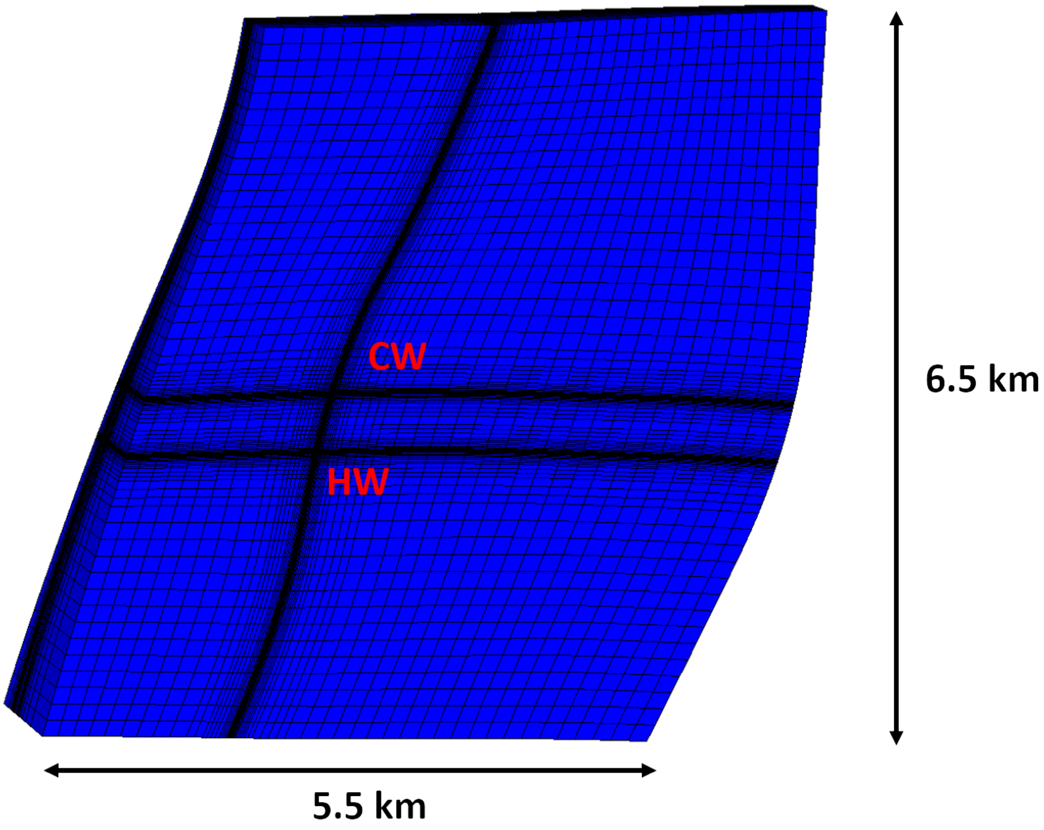

Figure 5.1: Simplified numerical model of the study area to assess the influence of the planned HT-ATES doublet of the DeepStor demonstrator (HW: hot well; CW: cold well) on its risk of the reactivation of a nearby fault and associated induced seismicity.

Hydrostatic pore pressure is calculated by solving for a steady-state solution at each timestep for mass balanced well fluxes. At the sides, top, and bottom of the model, zero-flow Neumann boundary conditions are imposed. Injection and production flow are implemented as functions with constant values (Neumann boundary conditions) for each injection and production cycle, ensuring mass conservation. To solve for heat transport, the pressure solution in conjunction with Equation **??** provides the relevant thermal flow rates to solve Equation 5.1. The initial temperature distribution is determined by the geothermal gradient of 50 K km^{-1} and the surface temperature of 10 °C.

A reference model (henceforth referred to as the "reference case") was developed to illustrate the influence of the operation of the planned DeepStor HT-ATES system on the stress distribution at a neighboring fault, assuming a strike-slip stress regime (Allgaier et al., 2023; Lempp et al., 2010; Meixner et al., 2016). The parametrization (Table 5.1) is based on the characterization of petrophysical and geological data from (former) oil fields within the URG (Stricker et al., 2020). The storage operation consists of two phases, each lasting six months.

Initially, during the summer ("charging period"), heated water at 140 °C is injected into the hot well, while the cold well acts as a producer. Subsequently, during the winter ("discharging period"), the operation is reversed, with water at 70°C (equaling the undisturbed reservoir temperature) being injected into the cold well (while the hot well becomes the producer).

Table 5.1: Parametrization of the reference case model of the DeepStor site based on average reservoir properties of (abandoned) oil fields in the URG, particularly the Leopoldshafen field (Banks et al., 2021; Stricker et al., 2020).

Parameter	**Value**
Reservoir permeability [m^2]	3×10^{-14}[b]
Permeability of the caprock [m^2]	10^{-18}[a]
Injection/production flow rate [Ls^{-1}]	3[a]
Effective porosity of the reservoir [-]	0.2[b]
Effective porosity of the caprock [-]	0.01[a]
Injection temperature of the cold well [°C]	70[a]
Injection temperature of the hot well [°C]	140[a]
Fluid density [kgm^{-3}]	1060[a]
Rock density [kgm^{-3}]	2425[f]
Distance between the fault and the wells [m]	100[a]
Young's modulus [GPa]	10[d]
Poisson's ratio [-]	0.3[d]
Friction angle of the fault [°]	30[a]
Thermal expansion coefficient [10^{-5} K^{-1}]	1[e]
Azimuth of the maximum horizontal stress [°]	150[f]
Gradient of the minimum horizontal stress [$MPakm^{-1}$]	16[f]
Gradient of the maximum horizontal stress [x lithostatic stress]	1.21[f]

The data origin is marked with [a]our assumptions/simplifications, [b]data compilation of Stricker et al. (2020), [c]Millero et al. (1980), [d]adapted from Marschall and Giger (2014) and Jahn et al. (2016), [e]Skinner, 1966, [f]adapted from Cornet et al. (2007), Dorbath et al. (2010), Lempp et al. (2010), Meixner et al. (2014), Meixner et al. (2016), and Allgaier et al. (2023).

5.3.3 *Assessment of the risk for fault reactivation*

The coupling scheme between the thermo-hydraulic numerical modeling and the semi-analytical calculations of stress changes on faults using MACRIS (Candela et al., 2022; van Wees et al., 2019) is briefly described here. The changes in the pressure and temperature fields obtained from the numerical simulations in ROSIM/DoubletCalc3D are used as input for the MACRIS calculations. To calculate stress changes resulting from either pore pressure or temperature changes, the point source solution of a small finite volume in an elastic half-space is adopted as Green's function (Mindlin, 1936; Okada, 1992). For this purpose, the fault is subdivided into sub-vertical line segments (termed "pillars"), on which the stress calculation is performed. An octree calculation algorithm (Barnes and Hut, 1986) is utilized to subdivide or merge the reservoir grid cells based on their proximity to the fault. Each node of the octree (merged or subdivided grid cells) represents a point source and contributes to the stress changes on the fault pillars, which stem from pore pressure and temperature variations within the model. In cases where these changes lead to an excess in Coulomb stress (CS) on the fault and the stresses exceed the Mohr-Coulomb failure criterion, the seismic moment can be calculated if stresses exceed the Mohr-Coulomb failure criterion (van Wees et al., 2018), enabling the estimation of the magnitudes of any resulting seismic events (van Wees et al., 2014).

$$CS = \tau - \mu\sigma'_n \tag{5.3}$$

τ is the shear stress, μ the friction coefficient, and σ'_n the effective normal stress acting on the surface of interest (in our case a fault). Considering the influence of injection and production, we must account for the influence of pore pressure changes (i.e. effective stresses) on the stress state (e.g. Jaeger et al., 2007).

Two approaches have been employed to evaluate the risk of fault reactivation, each relying on distinct assumptions regarding the representation of the initial stress state and stress changes. The first approach considers slip tendency (Morris et al., 1996; Worum et al., 2004). It is assumed that the fault is not critically stressed before the commencement of HT-ATES operations, accounting solely for the prevailing far-field stress state. Failure occurs when the slip tendency, T_s, exceeds the friction coefficient, μ.

$$T_s = \frac{\tau}{\sigma'_n} \geq \mu \tag{5.4}$$

In the second approach, we assume a fault that is initially nearly critically stressed, which implies that failure occurs when the Coulomb stress exceeds a specified threshold.

The seismic moment density (per m fault length in strike direction), $M0_m$, (van Wees et al., 2018) and magnitude, M_L, (van Wees et al., 2014) associated with potential failure can be calculated as follows:

$$M0_m = \Delta\sigma \frac{l^2}{\sqrt{\pi}} \tag{5.5}$$

$\Delta\sigma$ is the average excess Coulomb stress and l the rupture length.

$$M_L = \frac{2}{3} \log M_0 - 6.07 \tag{5.6}$$

M_0 is the seismic moment (product of moment density and fault length in strike direction).

5.4 REFERENCE CASE

Figure 5.2 shows the results of the thermo-hydraulic numerical simulations at the top of the reservoir following a single charging period for the reference case. The temperature distribution (Figure 5.2a) highlights the heating effect surrounding the hot injection well with an injection temperature of 140 °C. The temperature perturbation is restricted to the immediate vicinity of the hot well, dissipating over a distance of 100 m (the distance between the well and the fault; dashed white line) to only approximately 3.5 K. In contrast, the pressure perturbations (Figure 5.2b) influence a much larger area around the wells, exerting a significant influence on the fault, where changes of approximately 1.9 MPa are reached (black dashed line). Due to the dependence of water density and viscosity on temperature, the pressure changes around the hot well influence a greater volume, albeit with lower relative pressure fluctuations.

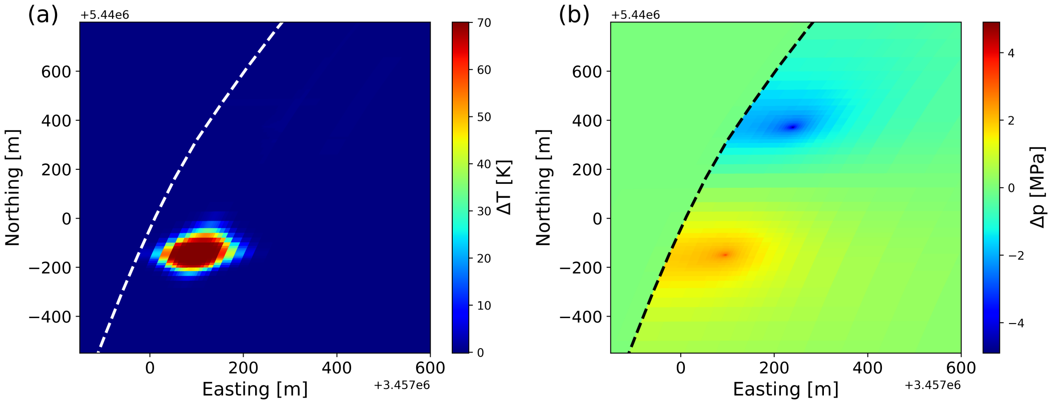

Figure 5.2: Distribution of temperature (a) and pressure (b) changes at the top of the reservoir after one charging period of six months for the reference case. The dashed white and black lines, respectively, represent the fault next to the well doublet at a distance of 100 m.

The pressure and temperature perturbations induced by heat storage lead to poroelastic and thermoelastic stress changes, respectively. Figure 5.3 depicts the changes in normal, shear, and Coulomb stress on the fault pillar adjacent to the hot well across four stages of the storage operation. As described above, after one charging period of six months, the hot water injection leads to a temperature increase of 3.5 K and a pressure increase of 1.9 MPa at the fault. This leads to a normal stress decrease in the reservoir (grey background) of up to -1.4 MPa (blue line in Figure 5.3a and c), whereas the shear stress (green line) exhibits only minor changes of -0.2 MPa. Consequently, the porothermoelastic stress changes result in a maximum Coulomb stress increase of 0.6 MPa (red line). Above and (to a lesser extent) below the reservoir, negative Coulomb and positive normal stress variations arise from the heating of the confining layers. Nonetheless, due to the large distance between the heated zone to the fault, this thermoelastic effect is far less significant than the superposition of poro- and thermoelasticity in the reservoir (e.g. 0.5 MPa compared to -1.4 MPa for the normal stress).

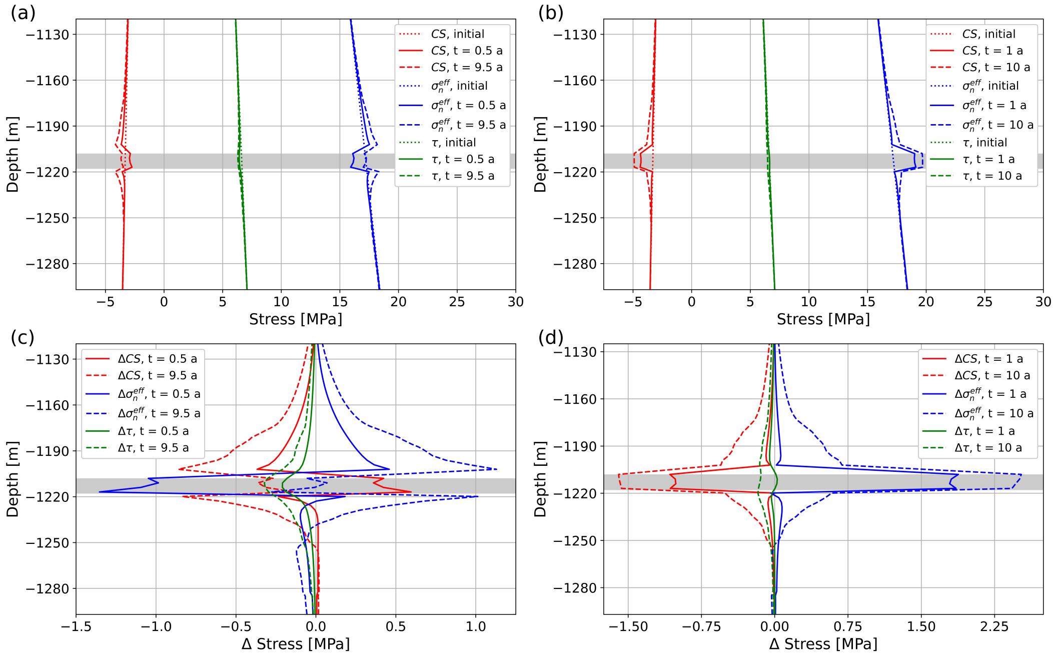

Figure 5.3: Stress changes at the investigated fault next to the hot well at reservoir depth (grey background) and above/below: the upper row presents absolute stress values (a) after the first and the tenth injection period (i.e. after 0.5 and 9.5 years, respectively), and (b) after one and ten full injection and production periods (i.e. after one and ten years, respectively). In the lower row, the relative stress changes are displayed for the same injection periods (c) and full injection and production periods (d).

After completing one full charging and discharging period of one year (represented by solid lines in Figure 5.3b and d), the combination of poroelasticity (induced by a production-related pressure decrease of -2.1 MPa) and thermoelasticity (originating from residual heating at the fault of 3 K) leads to a decrease in the Coulomb stress and an increase in the normal stress, reaching up to -1.1 MPa and 1.9 MPa, respectively. Shear stress variations remain negligible. The heating-induced effects on Coulomb and normal stress above and below the reservoir have largely dissipated during the discharging period.

After the tenth and final charging period (after 9.5 years; dashed lines in Figure 5.3a and c), the cumulative effects of heating become visible both within the reservoir and particularly above and below. Whereas the pressure changes are similar to the first charging period, a temperature increase of approximately 46 K occurs at the fault. Consequently, the thermoelastic effect due to continuous heating throughout ten charging cycles (represented by the difference between solid and dashed lines) results in near-zero stress changes for both Coulomb and normal stress, indicating that the previously dominating effect of injection-induced poroelasticity has been nearly counteracted by the increasing influence of thermoelasticity. For the shear stress changes, in contrast, the heating effect results in increasing absolute values (-0.2 MPa to -0.3 MPa), however, remaining relative small. Above and below the reservoir, the gradual heating of the confining layers exerts a substantial impact, particularly on normal stress changes, which increase from 0.5 MPa to 1.1 MPa. Moreover, these stress changes extend to a larger rock volume, reaching up to 40 m from the reservoir boundary.

Upon completion of the full simulation duration of ten charging and discharging periods (spanning ten years; dashed lines in Figure 5.3b and d), the residual heating becomes distinctly noticeable compared to after one charging and discharging period (43 K compared to 3 K). In the reservoir, this results in Coulomb stress changes increasing from -1.1 MPa to -1.4 MPa and normal stress changes increasing from 1.9 MPa to 2.5 MPa, with analogous effects in the confining layers above and below. Shear stress variations remain rather small.

According to the methodology outlined in Chapter 5.3.3, the hazard of fault reactivation and subsequent induced seismicity can be estimated from the calculated stress changes. Assuming a specific stress field, under which the fault is not critically stressed before the heat storage operation, the reduction in normal stress and the minor decrease in shear stress after one charging period lead to an increase in the slip tendency from 0.39 to 0.41. Under the additional assumption of a friction angle of 30°, the calculated slip tendencies are far below the associated value of 0.58. Consequently, the charging periods induce a minor destabilizing effect on the fault, resulting in a rather insignificant hazard of fault reactivation for the parametrization of the reference case. The heating of the reservoir and the confining layers above and below results in an increase in the normal stress, thereby exerting a stabilizing influence, reducing the hazard of fault reactivation and induced seismicity. This stabilizing effect similarly applies during the discharging periods, where the substantial increase in normal stress (with negligible changes in shear stress) leads to a slip tendency reduction, ultimately stabilizing the fault.

Assuming an already nearly critically stressed fault before the storage operation, even minor stress changes (e.g. the occurring changes in the Coulomb stress of 0.6 MPa after one charging period) could lead to lead to fault reactivation and induce seismicity. The reduction of Coulomb stresses over time due to reservoir heating to -0.4 MPa after the tenth charging period mitigates the hazard associated with subsequent charging periods and stabilizes the fault.

5.5 SENSITIVITY ANALYSIS

5.5.1 *Parameter sensitivity*

The findings of the reference case display the response of the DeepStor project's targeted reservoir to HT-ATES operations. The petrophysical properties of reservoir rocks in depleted hydrocarbon reservoirs in the URG exhibit substantial variations, ranging over multiple orders of magnitudes (e.g. Stricker et al., 2020). Additionally, the orientation of the stress field as well as the gradients and magnitudes of the principal stresses are subject to significant uncertainties (e.g. Cornet et al., 2007; Dorbath et al., 2010). Furthermore, the influence of operational decisions, such as the injection/production flow rate or the placement of the well doublet relative to subsurface faults, must also be considered. We therefore conducted a sensitivity analysis aiming to identify critical subsurface conditions that correspond to the risk of fault reactivation and induced seismicity. We focused on various reservoir parameters, operational conditions, and the stress field (Table 5.2), with parameter ranges based on assumptions and literature data. We investigated the influence of these parameters on both failure approaches, considering changes in the slip tendency and the Coulomb stress on a fault near the planned DeepStor doublet (see Chapter 5.3.3).

The sensitivity of the varied nine parameters on the slip tendency (a) and changes in the Coulomb stress (b) is depicted in Figure 5.4. The strongest influence on the slip tendency stems from alterations in the stress state: An increase of 13 % and 17 % in the orientation and gradient of the maximum horizontal stress (dashed black and green lines in Figure 5.4a), respectively, as well as a decrease of 19 % in the gradient of the minimum horizontal stress (dashed blue line) induce increases in the slip tendency of 13 %, 23 %, and 40 %, respectively. These variations in the slip tendency are primarily attributed to the influence of the stress state on the initial slip tendency. Conversely, changes in the distance between the wells and the fault, the injection and production flow rate, and the reservoir permeability exert a significant but smaller influence on the changes in the stress distribution caused by the heat storage operation: A 67 % decrease in the reservoir permeability (red line) and a 67 % increase in the injection/production flow rate (blue line) only translate into an increase in the slip tendency of 14 % and 3 %, respectively. The influence of the considered mechanical rock properties (Young's modulus and Poisson's ratio) and the thermal expansion coefficient on the slip tendency is rather negligible.

Table 5.2: Selected ranges of geological and operation parameters to determine their influence on the risk for fault reactivation and induced seismicity associated to HT-ATES operation.

Parameter	**Reference case**	**Range**	
		Min	**Max**
Reservoir permeability[b] [m^2]	3.0×10^{-14}	1.0×10^{-14}	5.0×10^{-14}
Injection/production flow rate[a] [Ls^{-1}]	3	1	5
Distance between the fault and the wells[a] [m]	100	10	1000
Young's modulus[c] [GPa]	10	2.5	25
Poisson's ratio[c] [-]	0.3	0.25	0.35
Thermal expansion coefficient[d] [10^{-6} K^{-1}]	10	8	12
Gradient of the minimum horizontal stress[e] [MPa km^{-1}]	16	13	23
Gradient of the maximum horizontal stress[e] [x lithostatic stress gradient]	1.21	1	1.42
Azimuth of the maximum horizontal stress[e] [°]	150	130	170

The data origin is marked with [a]our assumptions/simplifications, [b]data compilation of Stricker et al. (2020), [c]Marschall and Giger (2014), Jahn et al. (2016), and Egert et al. (2018), [d]Skinner (1966), [e]adapted from Cornet et al. (2007), Dorbath et al. (2010), Lempp et al. (2010), Meixner et al. (2014), Meixner et al. (2016), and Allgaier et al. (2023). For comparison, the parametrization of the base case is displayed.

The most pronounced influence on changes in the Coulomb stress stems from the reservoir permeability with a 185 % increase in the Coulomb stress for a permeability reduction of 67 % (red line in Figure 5.4b). Additionally, alterations in the orientation (dashed black line) and gradients (dashed blue and green lines) of the horizontal stresses, the flow rate (blue line), and the distance between the wells and the fault (green line) result in substantial increases in the Coulomb stress. In line with changes in the slip tendency, the variation of the considered mechanical rock properties (Young's modulus and Poisson's ratio) and the thermal expansion coefficient exerts the smallest influence on the Coulomb stress. For this reason, these three parameters were not further considered in this study.

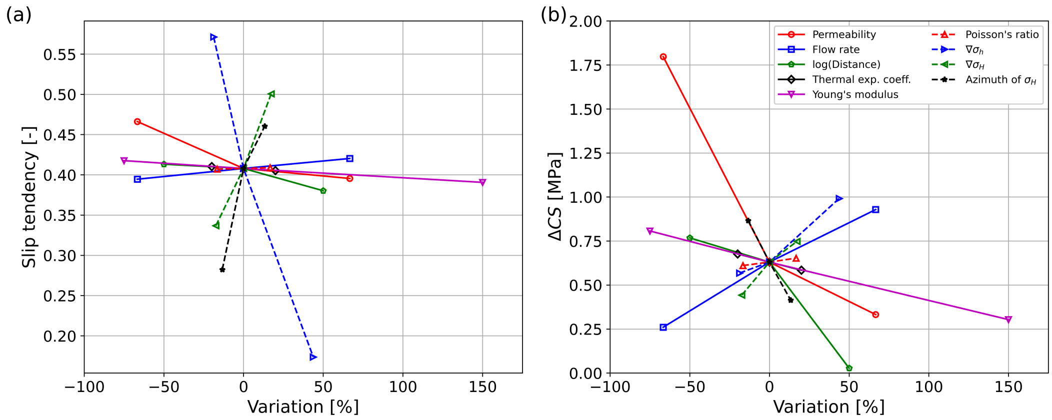

Figure 5.4: Sensitivity analysis examining the influence of each parameter (variation ranges listed in Table 5.2) on (a) the slip tendency, and (b) the changes in the Coulomb stress at a fault near the well doublet. The presented changes are relative to the reference case.

The diverging and apparently contradicting influence of the varied parameters on the slip tendency and the Coulomb stress can be explained by the different impacts of the parameter changes on incremental and absolute stresses. The slip tendency equals the ratio between absolute shear stress and effective normal stress (Equation 5.4), whereas the changes in the Coulomb stress are related to the changes in the shear and normal stresses (Equation 5.3). For the former, the influence of the magnitude of the initial stress field is most significant; for the latter, stress changes due to the heat storage operation play the largest role. This explains, for instance, why changes in the permeability (red lines) and the flow rate (blue lines) exert a larger influence on the changes in the Coulomb stress than in the slip tendency.

The apparent contradictions between the influence of the minimum horizontal stress gradient (dashed blue lines) and the orientation of the maximum horizontal stress (dashed black lines) on the slip tendency and the Coulomb stress changes can be explained similarly. The influence of these two parameters on the slip tendency is straightforward as the storage-induced stress changes are negligible compared to the variation in absolute stresses related to the initial stress field. On the one hand, an increase in the orientation of the maximum horizontal stress leads to a decrease in the effective normal stress and a small increase in the shear stress (apart for orientations approaching the fault strike). This results in an increase in the slip tendency. On the other hand, an increase in the minimum horizontal stresses leads to an increase in the effective normal stress and a decrease in the shear stress. Consequently, this results in a decrease in the slip tendency.

However, the influence of both incremental and absolute stresses has to be considered for the changes in the Coulomb stress. Whereas the changes in the effective normal stress are independent of the stress field, the shear stress changes strongly depend on the (initial) absolute effective normal stress. Consequently, as the Coulomb stress changes linearly depend on the shear stress changes, the size of the Coulomb stress changes correlates with the initial normal stress. This leads to a negative correlation between the orientation of the maximum horizontal stress and the Coulomb stress changes despite the positive correlation with the slip tendency, and to an opposite effect for the minimum horizontal stress gradient.

5.5.2 *Monte Carlo analysis*

The results of the parameter sensitivity analysis demonstrate the individual influence of each investigated parameter on the hazard of fault reactivation and subsequent induced seismicity. However, to comprehensively understand the influence of subsurface uncertainties, particularly the potential risks arising from the combination of multiple parameter uncertainties, it is insufficient to examine the influence of individual parameters in isolation. Therefore, we conducted a Monte Carlo analysis involving 1000 realizations to assess the effect of parameter uncertainties in a probabilistic framework. Herein, the most sensitive parameters identified through the sensitivity analysis were varied according to specific probability distributions (Table 5.3) based on the previously employed ranges (Table 5.2).

Since a separate mesh must be created for each variation of the distance between the wells and the fault in the ROSIM numerical simulation, eight discrete values for the distance, between 10 and 1000 m, were employed for the Monte Carlo analysis instead of a probabilistic distribution. One of these values was randomly selected for each realization. For the other five parameters, a normal distribution was applied based on the ranges used for the parameter analysis. If deemed appropriate due to underlying physical limitations or constraints identified in the literature research, limits were imposed on the resulting normally distributed values.

The histograms in Figure 5.5 depict normalized distributions of slip tendency following one charging period, highlighting the influence of each parameter variation. Each bar represents the normalized frequency of slip tendency for the corresponding parameter interval (or the discrete value for the distance between the wells and the fault). The color of each bar indicates the friction angle associated with the resulting slip tendency of the respective realization, which must be exceeded for failure (hereafter referred to as “critical friction angle”).

Table 5.3: Parameter distribution used in the Monte Carlo analysis to assess the risk of fault reactivation and induced seismicity. A normal distribution with the respective mean values μ and standard deviations σ was employed for each parameter except for the distance between the wells and the fault. If necessary, constraints were applied to the distributions to ensure that the parameter values remained within physically plausible ranges or conformed to limitations identified in the literature review. The abbreviation N/A illustrates that constraints were not applicable.

Parameter	**Distribution**	**Limits**
Distance between wells and fault [m]	10, 25, 50, 75, 100, 250, 500, 1000	N/A
Injection/production flow rate [Ls^{-1}]	$\mu = 3,\ \sigma = 1.25$	≥ 0.5
Reservoir permeability [m^2]	$\mu = 30,\ \sigma = 12.5$	≥ 5
Gradient of the minimum horizontal stress [MPa km^{-1}]	$\mu = 16,\ \sigma = 2$	[13, 23]
Gradient of the maximum horizontal stress [x lithostatic stress gradient]	$\mu = 1.21,\ \sigma = 0.1$	[0.9, 1.42]
Azimuth of the maximum horizontal stress^e [°]	$\mu = 150,\ \sigma = 15$	N/A

In accordance with the results of the parameter sensitivity analysis, the strongest influence is exerted by the variation of the azimuth of the maximum horizontal stress (i.e. the orientation of the stress field; Figure 5.5d) and the variation of the minimum horizontal stress gradient (e). The variation of the maximum horizontal stress gradient (f) also results in a significant but less pronounced influence on the critical failure angles. However, due to the application of a normal distribution to the parameter variation, the bars representing the lower and upper end of the ranges are less representative (due to a lower amount of realizations compared to bars representing average values).

In contrast, the variation of the distance between the fault and the well (a), the flow rate (b), and the permeability (c) does not result in a significant influence on the slip tendency. However, this does not imply that the variation of these parameters is inconsequential – as demonstrated otherwise by the parameter sensitivity analysis (Figure 5.4a) – but rather that the influence of the stress orientation and magnitudes outweighs that of the other investigated parameters.

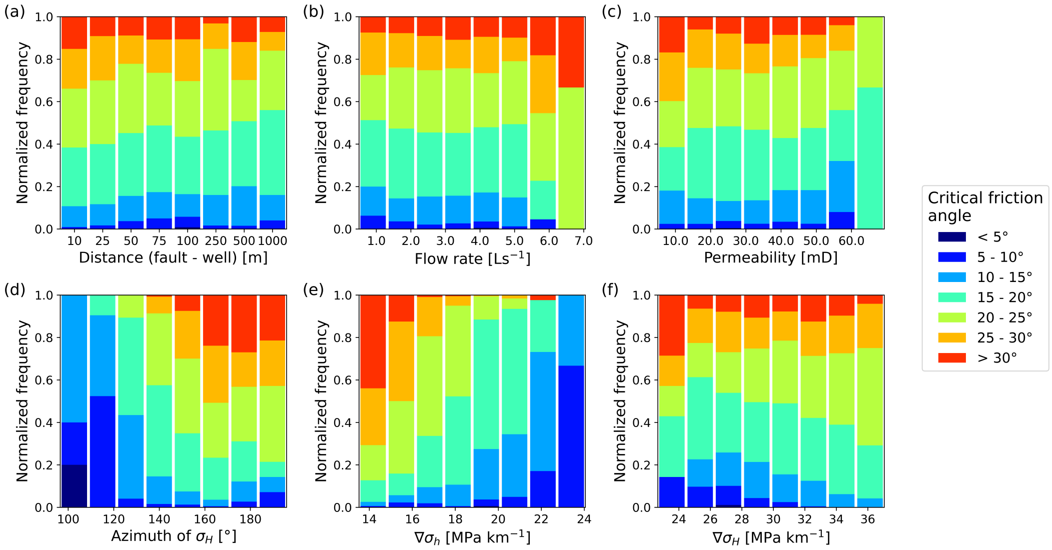

Figure 5.5: Normalized frequency distribution of the slip tendency for all six varied parameters in the Monte Carlo analysis. The color of the bars in the histograms represents the friction angles, which the slip tendency of the respective simulation would exceed, resulting in fault failure.

Figure 5.6 displays the dependency of the slip tendency on the azimuth of the maximum horizontal stress, demonstrating the strong influence of the stress field orientation on fault slip potential. Furthermore, the color-coding of the scatter plot underscores the association between the magnitude of the minimum horizontal stress and the slip tendency, with higher slip tendencies observed for lower stress gradients. The grey dashed vertical line in Figure 5.6 represents the orientation of the fault, with a strike of 192.5°. It becomes apparent that the slip tendency shows a positive correlation with increasing values of the orientation of the azimuth of the maximum horizontal stress (approaching the fault strike). This underlines similar observations of Allgaier et al. (2023), who investigated the slip and dilation tendency of the Leopoldshafen fault from a structural geology point of view. It also corroborates the assertion made in Chapter 5.5.1 that changes in the fault strike exert a comparable influence on the slip tendency as changes in the stress field orientation. The angle between fault strike and stress field orientation is the primary determinant of slip potential. Therefore, it is not necessary to independently vary the fault strike and the orientation of the stress field.

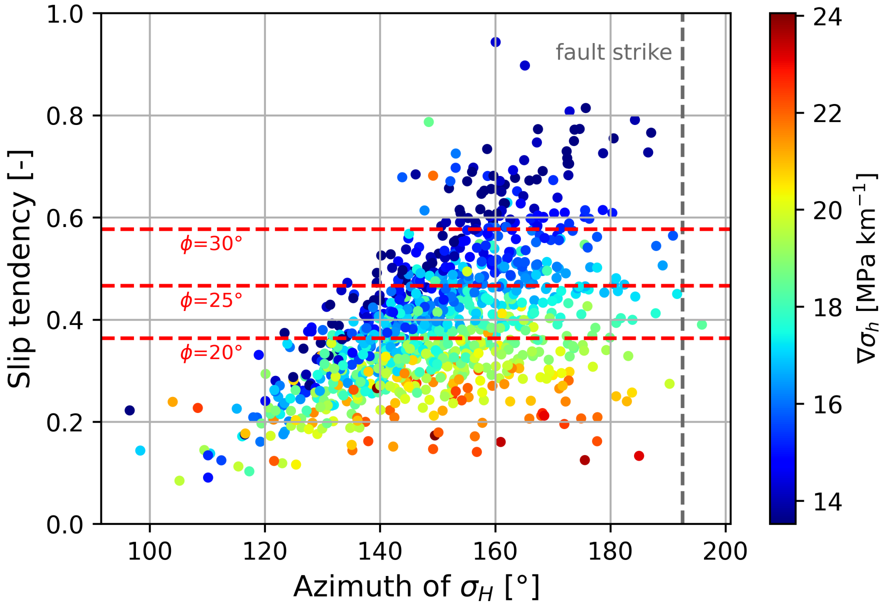

Figure 5.6: The dependency of the slip tendency on the azimuth of the maximum horizontal stress is depicted for the simulations conducted in the Monte Carlo analysis. The data points are color-coded according to the gradient of the minimum horizontal stress. The red dashed lines represent the friction coefficients that the slip tendency must exceed for failure, considering the respective friction angles. The fault strike is given by the dashed grey line. The results of five outliers (with slip tendencies > 1.0) are excluded from this figure.

In the following, we quantify the risk of fault reactivation assuming that the fault is not already critically stressed. This implies that failure occurs when the slip tendency exceeds the friction coefficient for specific friction angles depicted by the three red dashed horizontal lines in Figure 5.6. For a friction angle of 20° (corresponding to a friction coefficient of 0.36; lower red line), 54.0 % of the simulation results have critical slip tendencies exceeding the failure threshold, this decreases to 25.8 % of the simulation results for a friction angle of 25° (corresponding to a friction coefficient of 0.47; middle red line) and further to 10.1 % of the simulations results for a friction angle of 30° (corresponding to a friction coefficient of 0.58; upper red line).

A comparison of these Monte Carlo analysis results with the simulation of the base case (representing average properties for a depleted oil reservoir in the URG), which results in a slip tendency of approximately 0.41, demonstrates that a substantial risk of fault reactivation due to a HT-ATES operation at the DeepStor site can only be anticipated for an unfavorable alignment of geological and operational parameters, especially requiring very low friction coefficients.

Figure 5.7 illustrates the frequency distributions for changes in the Coulomb stress induced by the variation of the six investigated parameters in the Monte Carlo analysis. The largest sensitivities on the resulting Coulomb stresses are attributed to the distance between the wells and the fault (a), the flow rate (b), the reservoir permeability (c), and the azimuth of the maximum horizontal stress (d). The stress gradients, in contrast, exhibit less influence (Figure 5.7e and f). Analogous to the findings from the Monte Carlo analysis on the slip tendency, this does not imply that these two parameters lack any influence but rather that the influence of the other four parameters surpasses theirs. Moreover, the apparent decrease in the Coulomb stress for low values of the maximum horizontal stress stems from a limited number of data points (due to the employed normal distribution) and is therefore statistically insignificant.

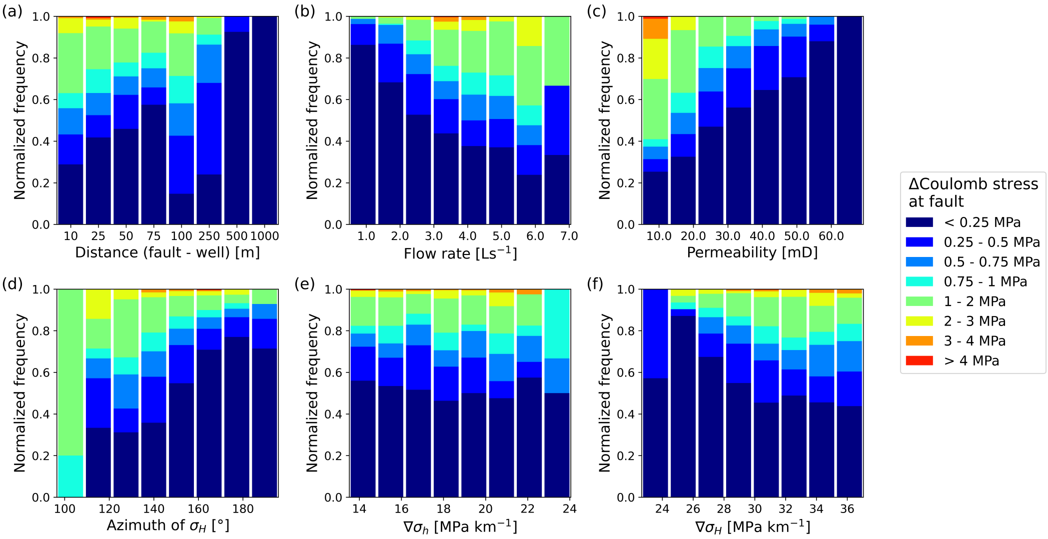

Figure 5.7: Normalized frequency distribution of the changes in Coulomb stress at the fault located adjacent to the hot well, considering all six parameters varied in the Monte Carlo analysis.

Contrary to an expected monotonic increase in the Coulomb stress with decreasing distances between the well doublet and the fault, the global maximum occurs at a distance of 100 m, followed by a local minimum at a distance of 75 m and further increasing stresses towards a distance of 10 m. This apparently paradoxical phenomenon can be attributed to the superimposed effects of poro- and thermoelastic stress changes and their varying contribution at different distances. The reduction in the distance between the wells and the fault from 1000 m to 100 m leads to increasing stress changes driven by the amplified pore pressure changes caused by water injection. At a distance of 75 m and smaller, the faults are mostly situated within the reservoir zone that is heated by the injected hot water. The larger thermoelastic stresses at this distance cause smaller total stress changes. For distances progressively smaller than 75 m, the poroelastic stress changes increase again due to the larger pressures close to the well. The thermoelastic influence is similar for all these distances (the heat front reaches the fault equally in those cases), therefore the Coulomb stress changes increase with distances smaller than 75 m.

Additionally, the deviations from the respective trends for the dependency of the Coulomb stress on the flow rate (negative correlation) and the permeability (positive correlation) are associated with the normal distribution of the parameter variation, which yields a lower absolute amount of data points at the respective lower and upper limits. Consequently, these deviations are solely of statistical origin without any additional implications.

The results of the above-described Monte Carlo analysis revealed the sensitivity of uncertainties in subsurface and operational parameters to changes in the Coulomb stress, emphasizing the significant impact of the distance between the well doublet and a fault of interest, the injection/production flow rate, the reservoir permeability, and the orientation of the stress field relative to the fault strike are influential.

Several key conclusions can be drawn from the findings of the sensitivity analysis: Unlike cold water injection employed in conventional geothermal utilization, which has been linked to induced seismicity (e.g. Martínez-Garzón et al., 2014), hot water injection during HT-ATES exhibits a mechanical stabilizing effect, corroborating the hypothesis proposed earlier in this study (Chapter 5.4). This stabilizing effect is reflected in a reduced hazard of induced seismicity for comparable pressure changes in the reservoir. Furthermore, the typically lower flow rates employed in HT-ATES systems compared to conventional geothermal operations and higher reservoir permeabilities may further minimize the hazard due to reduced pressure changes in the reservoir. Uncertainties in the reservoir permeability (e.g. investigated in the literature review of the petrophysical properties of depleted hydrocarbon reservoirs in the URG by Stricker et al. (2020)) may be partially mitigated by an appropriate selection of the injection/production flow rate.

Unlike conventional geothermal operations, which often target fault zones due to their enhanced permeability (Anyim and Gan, 2020; Seithel et al., 2019), the hazard of induced seismicity associated with HT-ATES systems can be mitigated by maintaining a sufficient distance to faults that may potentially be reactivated. Uncertainties regarding subseismic faults (e.g. smaller antithetic faults within the targeted graben block that cannot be identified in seismic data and remain undetected before well drilling) have to be considered as well (e.g. Damsleth et al., 1998; Maerten et al., 2006). Additionally, as demonstrated by the results of the Monte Carlo analysis presented above and the results of Allgaier et al. (2023), the angle between the orientation of the fault and the stress field plays a crucial role. Risks of fault reactivation increase when the azimuth of the maximum horizontal stress approaches the fault orientation, which can be expected for faults that have recently been active (Twiss and Moores, 2007).

Furthermore, in contrast to geothermal production, hydrocarbon production or carbon capture and storage, which are all frequently linked to induced seismicity arising from the buildup of reservoir pressure (Keranen et al., 2013; Kraft et al., 2009; Zoback and Gorelick, 2012) or reservoir compaction induced by pressure reduction during production (Zoback and Zinke, 2002; van Thienen-Visser and Breunese, 2015), the cyclicity of HT-ATES operations leads to a less significant build-up in reservoir pressure, thereby reducing the hazard of induced seismicity.

The parameter sensitivity and the Monte Carlo analysis above have demonstrated that uncertainties in the stress field and the fault strike exert a substantial influence on the risk for fault reactivation and induced seismicity. To address these uncertainties, well-established methods for measuring stress magnitudes and orientations, such as well logging (e.g. borehole breakout investigations) or well testing (e.g. hydraulic fracturing or leak-off tests) should be implemented during or after well drilling (e.g. Bell, 1996; Moos and Zoback, 1990).

5.6 CONCLUSIONS

The main concept of the DeepStor project is the proof of concept of the utilization of former hydrocarbon reservoirs (such as in the Upper Rhine Graben; URG) for high-temperature aquifer thermal energy storage (HT-ATES). Given the proximity of these storage systems to populated areas, a comprehensive assessment of potential hazards associated with their operation is paramount. The primary objective of this study is to evaluate the (geo-)mechanical stability of the DeepStor demonstrator, specifically focusing on quantifying the risk of fault reactivation and induced seismicity. To achieve this, thermo-hydraulic (TH) modeling was coupled with semi-analytical stress calculations.

Our findings reveal that HT-ATES operations induce stress changes of several MPa at a fault near the well doublet, primarily driven by injection-associated poroelasticity. These stress changes lead to a slight destabilization of the fault but pose only a minor hazard for fault reactivation and subsequent induced seismicity for average reservoir parameterizations. Over time, the reservoir heating and corresponding thermoelastic stress changes effectively stabilize the fault, consequently reducing the associated hazards.

To quantify the potential risks associated with the DeepStor demonstrator, two approaches were employed, both incorporating a Monte Carlo analysis to account for parameter uncertainties. In the first approach, an unstressed fault was assumed, and the risk of fault reactivation (and the associated risk of induced seismicity) was assessed based on the slip tendency distribution at the fault. The stress (and fault) orientation and magnitudes proved to be the most influential parameters for this approach, primarily affecting the initial slip tendency.

In the second approach, we assumed a nearly critically stressed fault and assessed the sensitivity of changes in the Coulomb stress at the fault that could potentially lead to failure. For this approach, the reservoir permeability, the injection/production flow rate, the distance between the wells and the fault, as well as the orientation of the stress field emerge as the most influential factors. Consequently, both the initial stress state and stress changes induced by the heat storage operation play significant roles in this scenario.

The identified risks can be significantly mitigated by an appropriate operational framework for the HT-ATES system. This includes strategically positioning the wells at a reasonable distance from any known faults, considering the fault orientation, and selecting flow rates that align with the reservoir transmissivity. Considering this appropriate operational framework, we conclude that HT-ATES systems exhibit a lower risk of induced seismicity than conventional geothermal systems due to (i) the stabilizing effect of reservoir heating in contrast to cold water injection as the primary cause for thermoelastically induced seismicity, (ii) lower flow rates and associated pressure changes, and (iii) the absence of active targeting of fault systems to prevent their reactivation. Unlike geothermal production, hydrocarbon production or carbon capture and storage, cyclic loading and unloading of the reservoir during the storage operation minimizes induced seismicity caused by pressure buildup or reservoir compaction.

The risk assessment performed in this study demonstrates that no substantial risks of fault reactivation and induced seismicity are anticipated during the operation of the proposed DeepStor demonstrator. By summarizing the findings of previous research on the risks of HT-ATES systems in former oil reservoirs in the URG (Stricker et al., 2024) and this study, it can be concluded that the operation of these systems should not be associated with significant risks of induced seismicity, surface uplift or subsidence. Future studies should explore appropriate monitoring strategies for both surface movements and induced seismicity. Additionally, further investigations into the DeepStor demonstrator (or HT-ATES systems in general) may also focus on assessing the impact of cyclic mechanical loading on well cementation.

ACKNOWLEDGEMENTS

This study is part of the subtopic "Geoenergy" in the program "MTET - Materials and Technologies for the Energy Transition" of the Helmholtz Association. The authors are responsible for the content of this publication.

6

CONCLUSIONS

Addressing the significant share of fossil fuel consumption and CO_2 emissions associated with heating and cooling is a critical hurdle in the transition to renewable energy systems. This challenge is further amplified by the seasonal mismatch between renewable energy availability in summer and the predominant heating demand in winter. While low-enthalpy deep geothermal energy can significantly contribute to heating needs in Central Europe, the seasonal fluctuations pose another obstacle to reliable renewable heating provision. High-temperature aquifer thermal energy storage (HT-ATES) systems, capable of storing excess summer heat in the subsurface, could enable deep geothermal energy sources to fulfill peak heating demand, particularly in winter, without relying on supplementary fossil fuel-based systems like gas boilers. Depleted hydrocarbon reservoirs in the Upper Rhine Graben (URG), a region with a rich history of exploration and exploitation of hydrocarbons and more recently also geothermal energy, coupled with elevated subsurface temperatures stemming from Germany's largest heat anomaly, present an ideal location for the implementation of HT-ATES systems.

The research presented in this thesis addressed two critical aspects of HT-ATES: 1) evaluating the feasibility of repurposing depleted hydrocarbon reservoirs, specifically oil reservoirs in the URG, as HT-ATES systems; and 2) assessing the (geo-)mechanical risks (e.g. ground surface movements and induced seismicity) associated with HT-ATES in these reservoirs, considering the specific geological and operational conditions that distinguish HT-ATES from other forms of subsurface utilization. To address the latter, I also pursued a deeper understanding of the underlying (geo-)mechanical processes in the subsurface. Additionally, due to the cyclic nature of HT-ATES operations compared to deep geothermal or hydrocarbon production, the investigation of their seasonal operation was a significant focus of this thesis. To achieve these objectives, coupled numerical models were integrated with legacy subsurface data from hydrocarbon exploration in the URG and semi-analytical stress calculation schemes. These approaches yielded novel insights into the coupled thermo-hydraulic and (geo-)mechanical behavior of the subsurface during HT-ATES operation. The principal findings of this thesis, encompassing Chapters 3 to 5 are summarized in the following section.

6.1 MAJOR FINDINGS OF THE RESEARCH

Extensive research has been conducted on numerical investigations of ATES systems, primarily assessing their storage performance, optimal well spacing, and the influence of reservoir heterogeneity. However, HT-ATES systems operating with high injection temperatures in deep reservoirs have received limited attention. The first study (Chapter 3) aimed to quantitatively evaluate the suitability and storage potential of HT-ATES in depleted hydrocarbon reservoirs in the URG through thermo-hydraulic numerical simulations. Employing available geological and petrophysical data from previous hydrocarbon exploration in the URG, a simplified numerical model was constructed to represent depleted oil reservoirs in the region. Simulations for an HT-ATES system with a well doublet and seasonal injection-production cycles resulted in annual storage capacities of up to 12 GWh, and recovery efficiencies exceeding 80 %. A sensitivity analysis identified various reservoir properties (permeability and thickness), injection-production flow rates, and the drilling configuration as the most influential parameters. Notably, the utilization of horizontal well paths significantly enhanced storage efficiency and potential by enabling larger flow rates for the same reservoir transmissivity compared to vertical wells. In conclusion, approximately 80 % of the investigated depleted oil fields in the URG could be converted into HT-ATES systems with annual storage capacities exceeding 2 GWh, resembling the operational storage site at the Reichstag building in Berlin, Germany.

To ensure the successful and safe realization of HT-ATES projects, it is crucial to evaluate potential risks alongside their theoretical potential. However, both in general and specifically for high-temperature systems, (geo-)mechanical risks associated with heat storage operations have received limited attention in previous research. This gap is particularly evident in studies examining the impact of HT-ATES on ground surface movements and induced seismicity. As ATES systems are typically located at shallower depths and involve mechanically less competent rocks compared to other forms of subsurface utilization (such as deep geothermal and hydrocarbon production), their unique geological and operational characteristics must be considered. For HT-ATES systems, in particular, the influence of elevated injection temperatures on (geo-)mechanical hazards demands thorough investigation. In Chapters 4 and 5, I addressed these research gaps by assessing the risks of HT-ATES for ground surface movements and induced seismicity, respectively.

In the second study (Chapter 4), I employed coupled thermo-hydraulic-mechanical (THM) numerical simulations to assess the impact of stress changes arising from the operation of HT-ATES systems in former oil reservoirs on ground surface movements. Reservoir heating induced stress changes around the hot injection well in the order of several MPa, resulting in vertical displacements within the reservoir on the mm-scale. These stress changes and the resulting displacements were primarily attributed to thermoelasticity, contributing up to 90 % of the total displacements. Conversely, ground surface movements were primarily governed by poroelasticity and additionally attenuated by two orders of magnitude. This transition from dominating thermoelasticity at reservoir depth to dominating poroelasticity at the ground surface stemmed from the stronger attenuation of the thermoelastic component of vertical displacements due to increased compression of the overlying rock matrix. A sensitivity analysis revealed that reservoir depth, elastic modulus, and injection/production flow rates were the primary controlling parameters for ground surface movements. Additionally, this study demonstrated that the cyclic operation of HT-ATES systems prevented cumulative uplift at the surface, in stark contrast to continuous injection and production (with cumulative pressure changes) associated with deep geothermal operations, hydrocarbon extraction, or CO_2 storage. In conclusion, only negligible ground surface movements were anticipated for HT-ATES operations in depleted hydrocarbon reservoirs in the URG.

Deviating from the coupled THM numerical simulations used in Chapter 4, in the third study of this thesis (Chapter 5) I employed a coupling scheme between thermo-hydraulic numerical simulations of the planned DeepStor simulator and semi-analytical stress calculations along a specific fault plane to evaluate the risk of HT-ATES systems for fault reactivation and induced seismicity. The results demonstrated that – mirroring the findings of Chapter 4 – stress changes of several MPa occur at a fault near the well doublet for an average reservoir parametrization, primarily stemming from poroelasticity induced by water injection. Notably, these stress changes pose only a minor hazard for fault reactivation and subsequent induced seismicity. Moreover, contrary to cold water injection, which often triggers induced seismicity in deep geothermal operations, hot water injection exhibited a stabilizing effect on the analyzed fault. Parameter sensitivity and Monte Carlo analyses revealed that stress field (and fault) orientation and magnitudes, operational parameters like injection/production flow rates, and the distance between wells and nearby faults significantly influence the risk of induced seismicity. However, these risks may be effectively mitigated through a well-defined operational framework that considers these operational and subsurface boundary conditions. In conclusion, I derived in Chapter 5 that HT-ATES systems pose a lower risk for fault reactivation compared to other forms of subsurface utilization, particularly due to the cyclic storage operation, which effectively minimizes induced seismicity stemming from pressure buildup or reservoir compaction.

The findings of the two risk assessments conducted in Chapter 4 and 5 can be summarized as follows: The targeted reservoirs for HT-ATES in depleted hydrocarbon reservoirs in the URG are too deep to pose a significant risk for ground surface movements, whereas at the same time shallow enough to maintain limited hydraulic connections to critically stressed faults so that the likelihood of induced seismicity is minimized. However, as discussed in the preceding paragraphs, potential risks may arise under specific subsurface and operational boundary conditions. These risks can be effectively addressed by implementing the following strategies, which should also be considered in the scope of approval procedures of future HT-ATES projects:

1. Maintaining a sufficient distance between the HT-ATES well doublet and nearby faults to minimize poroelastic stress changes and associated risks for induced seismicity, also taking into account fault orientation relative to the stress field.

2. Selecting injection/production flow rates that align with the reservoir transmissivity, thereby controlling poroelastic stress changes in the reservoir and their influence on both ground surface movements and induced seismicity.

3. Targeting reservoirs at sufficiently large depths with high elastic moduli, further reducing the impact of HT-ATES on ground surface deformation.

6.2 OUTLOOK

The present work has highlighted the suitability and substantial potential of depleted hydrocarbon reservoirs in the URG for HT-ATES utilization. Expanding the scope beyond depleted oil fields to include other promising sandstone formations could further increase this potential. Additionally, utilizing a broader data basis and incorporating similar geological formations, such as aquifers in the North German Basin or the Malm aquifer in the Bavarian Molasse Basin, could format promising research direction for assessing the potential of HT-ATES beyond the URG.

Aside from the risks explored in this thesis, HT-ATES in depleted hydrocarbon reservoirs may face additional limitations. By focusing on water-bearing compartments at the periphery of depleted oil reservoirs, I only conducted numerical simulations assuming one-phase flow, neglecting the potential influence of residual oil concentrations on HT-ATES operation and its efficiency. Incorporating multi-phase flow (including gas phases) into numerical simulations would provide a more comprehensive assessment of the influence of residual oil and whether it poses a significant challenge. In future research, numerical simulations should also take into account the coupled interactions between the wellbore and the reservoir, e.g. building on the work of Gholami Korzani et al. (2019) and Esmaeilpour et al. (2021).

The examination of chemical reactions within the reservoir triggered by hot water injection represents another research area worth investigating in future studies. This particularly applies to the effects of dissolution and precipitation processes on reservoir porosity and permeability. However, reservoir porosity and permeability are not solely influenced by chemical reactions; they also respond to strain changes induced by poro- and thermoelasticity. To account for these complex interactions, more sophisticated modeling approaches beyond purely elastic modeling (as conducted in this thesis), such as damage or phase-field modeling, could be considered. Additionally, advanced studies should address the potential for well cement degradation due to the cyclic mechanical loading during HT-ATES operation.

In all three studies of this thesis, homogeneous reservoir (and cap rock) parameterizations were assumed and uncertainties were only represented by sensitivity analyses. However, previous studies have shown the substantial impact of heterogeneities, particularly concerning geologic layering (Bridger and Allen, 2014). This underscores the need to address heterogeneities in both geological and parameterization aspects (e.g. reservoir permeability) of the storage system in future HT-ATES research. Furthermore, as numerical studies cannot replace the analysis of real systems, scientific demonstrators are needed for a proof of concept. For future economic use, further studies including life cycle analyses are essential.

REFERENCES

AGEB (2022). *Anwendungsbilanzen zur Energiebilanz Deutschland: Endenergieverbrauch nach Energieträgern und Anwendungszwecken*. URL: `https://ag-energiebilanzen.de/wp-content/uploads/2023/01/AGEB_21p2_V3_20221222.pdf`.

Aadnoy, B. S., Bell, J. S. et al. (1998). 'Classification of drilling-induced fractures and their relationship to in-situ stress directions'. In: *The Log Analyst* 39.06.

Agemar, T., Schellschmidt, R. and Schulz, R. (2012). 'Subsurface temperature distribution in Germany'. In: *Geothermics* 44, pp. 65–77. ISSN: 03756505. DOI: `10.1016/j.geothermics.2012.07.002`.

Agemar, T., Weber, J. and Schulz, R. (2014). 'Deep Geothermal Energy Production in Germany'. In: *Energies* 7.7, pp. 4397–4416. DOI: `10.3390/en7074397`.

AlBahrani, H., Al-Qahtani, A., Marhoon, Z. and Hamid, O. (2018). 'A Newly Developed Process for Wellbore Geometry Analysis from a Geomechanical Perspective'. In: *SPE Kingdom of Saudi Arabia Annual Technical Symposium and Exhibition*. Vol. 192210-MS.

AlBahrani, H. and Morita, N. (2020). 'Understanding the Concurrence of Drilling Induced Fractures and Breakouts and Its Implications on Drilling Performance Using a 3D FEM and Field Imaging Data'. In: *International Petroleum Technology Conference*. IPTC.

Albukhari, T. M., Beshish, G. K., Abouzbeda, M. M. and Madi, A. (2018). 'Geomechanical Wellbore Stability Analysis for the Reservoir Section in JNC186 Oil Field'. In: *ISRM 1st International Conference on Advances in Rock Mechanics - Tunirock 2018*. Ed. by E. Hamdi, pp. 179–193.

Alizadeh, M., Movahed, Z., Junin, R. and Mohsin, R. (2015). 'Finding the Drilling Induced Fractures and Borehole Breakouts Directions Using Image Logs'. In: *Journal of Advanced Research in Applied Mechanics* 10.1, pp. 9–30.

Allgaier, F., Busch, B. and Hilgers, C. (2023). 'Fault leakage and reservoir charging in the Upper Rhine Graben, Germany – Assessment of the Leopoldshafen fault bend'. In: *Marine and Petroleum Geology* 156, p. 106428. ISSN: 02648172. DOI: `10.1016/j.marpetgeo.2023.106428`.

Allouche, E. N., Ariaratnam, S. T. and Lueke, J. S. (2000). 'Horizontal Directional Drilling: Profile of an Emerging Industry'. In: *Journal of Construction Engineering* *and Management* 126.1, pp. 68–76. ISSN: 0733-9364. DOI: `10.1061/(ASCE)0733-9364(2000)126:1(68)`.

Altmann, J. B., Müller, T. M., Müller, B. I., Tingay, M. R. and Heidbach, O. (2010). 'Poroelastic contribution to the reservoir stress path'. In: *International Journal of Rock Mechanics and Mining Sciences* 47.7, pp. 1104–1113. DOI: `10.1016/j.ijrmms.2010.08.001`.

Andersson, O., Hellsröm, G. and Nordell, B. (2003). 'Heating and cooling with UTES in Sweden - current situation and potential market development'. In: *Futurestock 2003*. Warsaw: Warsaw University of Technology. ISBN: 9788372074355.

Andersson, O. (2007). 'AQUIFER THERMAL ENERGY STORAGE (ATES)'. In: *Thermal Energy Storage for Sustainable Energy Consumption*. Ed. by H. Ö. Paksoy. Vol. 234. NATO Science Series. Dordrecht: Springer Netherlands, pp. 155–176. ISBN: 978-1-4020-5288-0. DOI: `10.1007/978-1-4020-5290-3{\textunderscore}8`.

Anyim, K. and Gan, Q. (2020). 'Fault zone exploitation in geothermal reservoirs: Production optimization, permeability evolution and induced seismicity'. In: *Advances in Geo-Energy Research* 4.1, pp. 1–12. ISSN: 22079963. DOI: `10.26804/ager.2020.01.01`.

Ashena, R., Elmgerbi, A., Rasouli, V., Ghalambor, A., Rabiei, M. and Bahrami, A. (2020). 'Severe wellbore instability in a complex lithology formation necessitating casing while drilling and continuous circulation system'. In: *Journal of Petroleum Exploration and Production Technology* 10.4, pp. 1511–1532. ISSN: 2190-0558. DOI: `10.1007/s13202-020-00834-3`.

Azzola, J., Valley, B., Schmittbuhl, J. and Genter, A. (2019). 'Stress characterization and temporal evolution of borehole failure at the Rittershoffen geothermal project'. In: *Solid Earth* 10.4, pp. 1155–1180. DOI: `10.5194/se-10-1155-2019`.

BDEW (2019). *Energy Market Germany 2019*. URL: `https://www.bdew.de/media/documents/Pub_20190603_Energy-Market-Germany-2019.pdf`.

BDEW (2021). *Wärmewende*. URL: `https://www.bdew.de/presse/pressemappen/waermewende/`.

Bächler, D., Kohl, T. and Rybach, L. (2003). 'Impact of graben-parallel faults on hydrothermal convection—-Rhine Graben case study'. In: *Physics and Chemistry of the Earth, Parts A/B/C* 28.9-11, pp. 431–441. ISSN: 14747065. DOI: `10.1016/S1474-7065(03)00063-9`.

Bagala, S., McWilliam, I., O'Rourke, T. and Liu, C. (2010). 'Real - Time Geomechanics: Applications to Deepwater Drilling'. In: *SPE Deepwater Drilling and Completions Conference*. Vol. 137071.

Baillieux, P., Schill, E., Abdelfettah, Y. and Dezayes, C. (2014). 'Possible natural fluid pathways from gravity pseudo-tomography in the geothermal fields of Northern Alsace (Upper Rhine Graben)'. In: *Geothermal Energy* 2.1, p. 226. DOI: `10.1186/s40517-014-0016-y`.

Baillieux, P., Schill, E., Edel, J.-B. and Mauri, G. (2013). 'Localization of temperature anomalies in the Upper Rhine Graben: insights from geophysics and neotectonic activity'. In: *International Geology Review* 55.14, pp. 1744–1762. ISSN: 0020-6814. DOI: `10.1080/00206814.2013.794914`.

Bakr, M., van Oostrom, N. and Sommer, W. (2013). 'Efficiency of and interference among multiple Aquifer Thermal Energy Storage systems; A Dutch case study'. In: *Renewable Energy* 60, pp. 53–62. ISSN: 09601481. DOI: `10.1016/j.renene.2013.04.004`.

Banks, J., Poulette, S., Grimmer, J., Bauer, F. and Schill, E. (2021). 'Geochemical Changes Associated with High-Temperature Heat Storage at Intermediate Depth: Thermodynamic Equilibrium Models for the DeepStor Site in the Upper Rhine Graben, Germany'. In: *Energies* 14.19, p. 6089. DOI: `10.3390/en14196089`.

Bär, K., Reinsch, T. and Bott, J. (2020). 'P3 - PetroPhysical Property Database - a global compilation of lab measured rock properties'. In: *Earth System Science Data Open Access Discussions, in review*. DOI: `10.5194/essd-2020-15`.

Bär, K., Rühaak, W., Welsch, B., Schulte, D., Homuth, S. and Sass, I. (2015). 'Seasonal High Temperature Heat Storage with Medium Deep Borehole Heat Exchangers'. In: *Energy Procedia* 76, pp. 351–360. ISSN: 18766102. DOI: `10.1016/j.egypro.2015.07.841`.

Barnes, J. and Hut, P. (1986). 'A hierarchical O(N log N) force-calculation algorithm'. In: *Nature* 324, pp. 446–449.

Barton, C. A., Zoback, M. D. and Burns, L. (1988). 'In-situ stress orientation and magnitude at the Fenton Geothermal Site, New Mexico, determined from wellbore breakouts'. In: *Geophysical Research Letters* 15.5, pp. 467–470. DOI: `10.1029/gl015i005p00467`.

Bauer, D., Marx, R., Nußbicker-Lux, J., Ochs, F., Heidemann, W. and Müller-Steinhagen, H. (2010). 'German central solar heating plants with seasonal heat storage'. In: *Solar Energy* 84.4, pp. 612–623. ISSN: 0038092X. DOI: `10.1016/j.solener.2009.05.013`.

Bear, J. (1972). *Dynamics of fluids in porous media*. Environmental science series. New York: American Elsevier. ISBN: 9780444001146.

Bear, J. and Cheng, A. H.-D. (2010). *Modeling Groundwater Flow and Contaminant Transport*. Vol. 23. Theory and Applications of Transport in Porous Media. Dordrecht: Springer Science+Business Media B.V. ISBN: 978-1-4020-6681-8. DOI: `10.1007/978-1-4020-6682-5`. URL: `http://site.ebrary.com/lib/alltitles/docDetail.action?docID=10359873`.

Békési, E., Fokker, P. A., Martins, J. E., Limberger, J., Bonté, D. and van Wees, J.-D. (2019). 'Production-Induced Subsidence at the Los Humeros Geothermal Field Inferred from PS-InSAR'. In: *Geofluids* 2019, pp. 1–12. ISSN: 14688115. DOI: `10.1155/2019/2306092`.

Bell, J. S. (1996). 'In situ stresses in sedimentary rocks: Measurement techniques'. In: *Geoscience Canada* 23.2, pp. 85–100.

Bergant, A., Simpson, A. R. and Tijsseling, A. S. (2006). 'Water hammer with column separation: A historical review'. In: *Journal of Fluids and Structures* 22.2, pp. 135–171. ISSN: 08899746. DOI: `10.1016/j.jfluidstructs.2005.08.008`.

Berger, J.-P., Reichenbacher, B., Becker, D., Grimm, M., Grimm, K., Picot, L., Storni, A., Pirkenseer, C. and Schaefer, A. (2005). 'Eocene-Pliocene time scale and stratigraphy of the Upper Rhine Graben (URG) and the Swiss Molasse Basin (SMB)'. In: *International Journal of Earth Sciences* 94.4, pp. 711–731. ISSN: 1437-3254. DOI: `10.1007/s00531-005-0479-y`.

Biot, M. A. (1962). 'Mechanics of Deformation and Acoustic Propagation in Porous Media'. In: *Journal of Applied Physics* 33.4, pp. 1482–1498. ISSN: 0021-8979. DOI: `10.1063/1.1728759`.

Birdsell, D. T., Adams, B. M. and Saar, M. O. (2021). 'Minimum transmissivity and optimal well spacing and flow rate for high-temperature aquifer thermal energy storage'. In: *Applied Energy* 289, p. 116658. ISSN: 03062619. DOI: `10.1016/j.apenergy.2021.116658`.

Birdsell, D. T. and Saar, M. O. (2020). *Modeling Ground Surface Deformation at the Swiss HEATSTORE Underground Thermal Energy Storage Sites*. DOI: `10.3929/ethz-b-000421353`.

Blumenroeder, J. (1962). 'Le pétrole en Alsace'. In: *Abh. Geol. Landesamt Baden-Württemberg* 4, pp. 41–62.

Böcker, J. (2015). 'Petroleum system and thermal history of the Upper Rhine Graben: Implications from organic geochemical analyses, oil-source rock correlations and numerical modelling'. Dissertation. Aachen: RWTH Aachen.

Böcker, J., Littke, R. and Forster, A. (2017). 'An overview on source rocks and the petroleum system of the central Upper Rhine Graben'. In: *International Journal of Earth Sciences* 106.2, pp. 707–742. ISSN: 1437-3254. DOI: `10.1007/s00531-016-1330-3`.

Boigk, H. (1981). *Erdöl und Erdölgas in der Bundesrepublik Deutschland: Erdölprovinzen, Felder, Förderung, Vorräte, Lagerstättentechnik*. Stuttgart: Enke. ISBN: 3432912714.

Bourne, S. J., Oates, S. J., Bommer, J. J., Dost, B., van Elk, J. and Doornhof, D. (2015). 'A Monte Carlo Method for Probabilistic Hazard Assessment of Induced Seismicity due to Conventional Natural Gas Production'. In: *Bulletin of the Seismological Society of America* 105.3, pp. 1721–1738. ISSN: 0037-1106. DOI: `10.1785/0120140302`.

Bremer, J., Nitschke, F., Bauer, F., Schill, E., Kohl, T., Kaymacki, E., Koelbel, T., El-Alfy, A., Ollinger, D., Meier, P., Pei, L., Blöcher, G., Klein, S., Hahn, F., Atkinson, T., McLing, T., Jin, W., Zhang, Y., Dobson, P., Rutqvist, J., Hörbrand, T. and Jahrfeld, T. (2022). 'VESTA - Very-High-Temperature Heat Aquifer Storage'. In: *Proceedings of the European Geothermal Congress 2022*.

Bresee, J. C., ed. (1992). *Geothermal energy in Europe: The Soultz Hot Dry Rock Project*. Montreux: Gordon and Breach Science Publ. ISBN: 9782881245237. URL: `http://www.loc.gov/catdir/enhancements/fy0653/91036197-d.html`.

Bretan, P., Yielding, G., Mathiassen, O. M. and Thorsnes, T. (2011). 'Fault-seal analysis for CO 2 storage: an example from the Troll area, Norwegian Continental Shelf'. In: *Petroleum Geoscience* 17.2, pp. 181–192. ISSN: 1354-0793. DOI: `10.1144/1354-079310-025`.

Bridger, D. W. and Allen, D. M. (2014). 'Influence of geologic layering on heat transport and storage in an aquifer thermal energy storage system'. In: *Hydrogeology Journal* 22.1, pp. 233–250. ISSN: 1431-2174. DOI: `10.1007/s10040-013-1049-1`.

Brudy, M. and Kjorholt, H. (1992). 'Stress orientation on the Norwegian continental shelf derived from borehole failures observed in high-resolution borehole imaging logs'. In: *Tectonophysics* 337, pp. 65–84. ISSN: 00401951.

Bruss, D. (2000). 'Zur Herkunft der Erdöle im mittleren Oberrheingraben und ihre Bedeutung für die Rekonstruktion der Migrationsgeschichte und der Speichergesteinsdiagenese'. Dissertation. Jülich: Forschungszentrum Jülich / Universität Erlangen-Nürnberg.

Buijze, L., van Bijsterveldt, L., Cremer, H., Paap, B., Veldkamp, H., Wassing, B. B., van Wees, J.-D., van Yperen, G. C., Heege, J. H. ter and Jaarsma, B.

(2019). 'Review of induced seismicity in geothermal systems worldwide and implications for geothermal systems in the Netherlands'. In: *Netherlands Journal of Geosciences* 98. ISSN: 0016-7746. DOI: `10.1017/njg.2019.6`.

Burgess, T. and van de Slijke, P. (1991). 'Horizontal Drilling Comes of Age'. In: *Oil Field Review* 2.3, pp. 22–23.

Burkhardt, J. A. (1961). 'Wellbore Pressure Surges Produced by Pipe Movement'. In: *Journal of Petroleum Technology* 13.06, pp. 595–605. ISSN: 0149-2136. DOI: `10.2118/1546-G-PA`.

Candela, T., Goncalves Machado, C., Leeuwenburgh, O. and Heege, J. ter (2022). 'A physics-informed optimization workflow to manage injection while constraining induced seismicity: The Oklahoma case'. In: *Frontiers in Earth Science* 10. DOI: `10.3389/feart.2022.1053951`.

Carman, P. C. (1937). 'Fluid flow through granular beds'. In: *Transactions, Institution of Chemical Engineers, London* 15, pp. 150–166.

Caron, E. (2012). 'Réalisation d'une base de données porosité-perméabilité dans le fossé rhénan'. Bachelorthesis. Lille: Université Lille Nord de France.

Carslaw, H. S. and Jaeger, J. C. (1959). *Conduction of heat in solids*. 2. ed. Oxford science publications. Oxford: Clarendon Press. ISBN: 978-0198533030.

Ceccato, A., Viola, G., Tartaglia, G. and Antonellini, M. (2021). 'In–situ quantification of mechanical and permeability properties on outcrop analogues of offshore fractured and weathered crystalline basement: Examples from the Rolvsnes granodiorite, Bømlo, Norway'. In: *Marine and Petroleum Geology* 124, p. 104859. ISSN: 02648172. DOI: `10.1016/j.marpetgeo.2020.104859`.

Chen, Y., Zhou, C. and Jing, L. (2009). 'Modeling coupled THM processes of geological porous media with multiphase flow: Theory and validation against laboratory and field scale experiments'. In: *Computers and Geotechnics* 36.8, pp. 1308–1329. ISSN: 0266352X. DOI: `10.1016/j.compgeo.2009.06.001`.

Clauser, C. and Villinger, H. (1990). 'Analysis of conductive and convective heat transfer in a sedimentary basin, demonstrated for the Rheingraben'. In: *Geophysical Journal International* 100.3, pp. 393–414. ISSN: 0956-540X. DOI: `10.1111/j.1365-246X.1990.tb00693.x`.

Coker, A. K. and Ludwig, E. E. (2007). *Ludwig's applied process design for chemical and petrochemical plants: Volume 1*. 4th ed. Amsterdam and Boston: Elsevier Gulf Professional. ISBN: 978-0-7506-7766-0. URL: `http://search.ebscohost.com/login.aspx?direct=true&scope=site&db=nlebk&db=nlabk&AN=186120`.

Colmenares, L. and Zoback, M. (2002). 'A statistical evaluation of intact rock failure criteria constrained by polyaxial test data for five different rocks'. In: *International Journal of Rock Mechanics and Mining Sciences* 39.6, pp. 695–729. DOI: `10.1016/S1365-1609(02)00048-5`.

Cornet, F. H., Bérard, T. and Bourouis, S. (2007). 'How close to failure is a granite rock mass at a 5km depth?' In: *International Journal of Rock Mechanics and Mining Sciences* 44.1, pp. 47–66. DOI: `10.1016/j.ijrmms.2006.04.008`.

Cornet, F. H. (2015). *Elements of crustal geomechanics*. 1. publ. Cambridge: Cambridge Univ. Press. ISBN: 978-0-521-87578-3. URL: `https://permalink.obvsg.at/AC12283941`.

Coulomb, C. (1773). 'Application des règles de maxima et minima à quelques problèmes de statique relatifs à l´Architecture'. In: *Mémoires de Mathématiques et de Physiques présentés à l´Académie Royale des Sciences* 7, pp. 343–382.

Damsleth, E., Sangolt, V. and Aamodt, G. (1998). 'Sub-seismic Faults Can Seriously Affect Fluid Flow in the Njord Field off Western Norway - A Stochastic Fault Modeling Case Study'. In: *1998 SPE Annual Technical Conference and Exhibition*.

Davis, R. O. and Selvadurai, A. P. S. (1996). *Elasticity and geomechanics*. 1. publ. Cambridge u.a.: Cambridge Univ. Pr. ISBN: 9780521498272. URL: `http://media.obvsg.at/AC01554720-3401`.

Derer, C. E. (2003). 'Tectono-sedimentary evolution of the northern Upper Rhine Graben (Germany), with special regards to the early syn-rift stage'. Dissertation. Bonn: Universität Bonn.

Dickinson, J. S., Buik, N., Matthews, M. C. and Snijders, A. (2009). 'Aquifer thermal energy storage: theoretical and operational analysis'. In: *Géotechnique* 59.3, pp. 249–260. ISSN: 0016-8505. DOI: `10.1680/geot.2009.59.3.249`.

Dinçer, İ. and Rosen, M. A. (2011). *Thermal energy storage: Systems and applications*. 2nd ed. Hoboken, N.J: Wiley. ISBN: 978-0-470-97073-7. URL: `http://e-res.bis.uni-oldenburg.de/redirect.php?url=http://lib.myilibrary.com/detail.asp?id=281756`.

Dinkelman, D., Carpentier, S., Koenen, M., Oerlemans, P., Godschalk, B., Peters, E., Bos, W., Vrijlandt, M. and van Wees, J.-D. (2022). 'High-temperature aquifer thermal energy storage performance in Middenmeer, the Netherlands: thermal monitoring and model calibration'. In: *Proceedings of the European Geothermal Congress 2022*.

Doglioni, C. (2018). 'A classification of induced seismicity'. In: *Geoscience Frontiers* 9.6, pp. 1903–1909. ISSN: 16749871. DOI: `10.1016/j.gsf.2017.11.015`.

Dorbath, L., Evans, K., Cuenot, N., Valley, B., Charléty, J. and Frogneux, M. (2010). 'The stress field at Soultz-sous-Forêts from focal mechanisms of induced seismic events: Cases of the wells GPK2 and GPK3'. In: *Comptes Rendus Geoscience* 342.7-8, pp. 600–606. ISSN: 16310713. DOI: `10.1016/j.crte.2009.12.003`.

Drijver, B., van Aarssen, M. and Zwart, B. de (2012). 'High-temperature aquifer thermal energy storage (HT-ATES): sustainable and multi-usable'. In: *Innostock 2012 - the 12th International Conference on Energy Storage*. Ed. by L. F. Cabeza. Lleida. ISBN: 9788493879334.

Dupriest, F. E., Elks, W. C., Ottesen, S., Pastusek, P. E., Zook, J. R. and Aphale, C. R. (2010). 'Borehole Quality Design and Pracices to Maximize Drill Rate Performance'. In: *SPE Annual Technical Conference and Exhibition*. Vol. 134580.

Durst, H. (1991). 'Aspects of exploration history and structural style in the Rhine Graben area'. In: *Generation, accumulation, and production of Europe's hydrocarbons*. Ed. by A. Spencer. Vol. 1, pp. 247–261.

EURES (2008). *Regionalprofil Oberrhein - 2008: Statistische Daten, Analyse der wirtschaftlichen Lage und des Arbeitsmarktes*. Ed. by T. Schoder. URL: `https://www.eures-t-oberrhein.eu/fileadmin/user_upload/Downloads/de/Regionalprofil_2008_dt.pdf`.

Egert, R., Gaucher, E., Savvatis, A., Goblirsch, P. and Kohl, T. (2022). 'Numerical determination of long-term alterations of THM characteristics of a Malm geothermal reservoir during continuous exploitation'. In: *Proceedings of the European Geothermal Congress 2022*.

Egert, R., Korzani, M. G., Held, S. and Kohl, T. (2020). 'Implications on large-scale flow of the fractured EGS reservoir Soultz inferred from hydraulic data and tracer experiments'. In: *Geothermics* 84, p. 101749. ISSN: 03756505. DOI: `10.1016/j.geothermics.2019.101749`.

Egert, R., Nitschke, F., Gholami Korzani, M. and Kohl, T. (2021). 'Stochastic 3D Navier–Stokes Flow in Self–Affine Fracture Geometries Controlled by Anisotropy and Channeling'. In: *Geophysical Research Letters* 48.9. ISSN: 0094-8276. DOI: `10.1029/2020GL092138`.

Egert, R., Seithel, R., Kohl, T. and Stober, I. (2018). 'Triaxial testing and hydraulic–mechanical modeling of sandstone reservoir rock in the Upper Rhine Graben'. In: *Geothermal Energy* 6.1. DOI: `10.1186/s40517-018-0109-0`.

Ekstrom, M. P., Dahan, C. A., Chen, M. Y., Lloyd, P. M. and Rossi, D. J. (1987). 'Formation imaging with microelectrical scanning arrays'. In: *Log Analyst* 28, pp. 294–306.

Ellis, D. and Singer, J. (2007). *Well logging for earth scientists*. Dordrecht London: Springer. ISBN: 978-1-4020-4602-5.

Esmaeilpour, M., Gholami Korzani, M. and Kohl, T. (2021). 'Performance Analyses of Deep Closed-loop U-shaped Heat Exchanger System with a Long Horizontal Extension'. In: *Proceedings of the 46th Workshop on Geothermal Reservoir Engineering*.

European Commission (2016). *Communication from the commission to the European parliament, the council, the European economic and social committee and the committee of the regions: An EU Strategy on Heating and Cooling*. Brussels, Belgium. URL: `https://eur-lex.europa.eu/legal-content/EN/TXT/PDF/?uri=CELEX:52016DC0051`.

Evans, D., Graham, C., Armour, A. and Bathurst, P. (2003). *The Millenium Atlas: petroleum geology of the central and northern North Sea*. London: The Geological Society of London.

Evans, K. F., Zappone, A., Kraft, T., Deichmann, N. and Moia, F. (2012). 'A survey of the induced seismic responses to fluid injection in geothermal and CO2 reservoirs in Europe'. In: *Geothermics* 41, pp. 30–54. ISSN: 03756505. DOI: `10.1016/j.geothermics.2011.08.002`.

Fjær, E., Holt, R. M., Horsrud, P., Raaen, A. M. and Risnes, R. (2008). *Petroleum related rock mechanics*. 2. ed. Vol. 53. Developments in petroleum science. Amsterdam u.a.: Elsevier. ISBN: 9780444502605. URL: `https://permalink.obvsg.at/AC07917548`.

Fleuchaus, P., Godschalk, B., Stober, I. and Blum, P. (2018). 'Worldwide application of aquifer thermal energy storage – A review'. In: *Renewable and Sustainable Energy Reviews* 94, pp. 861–876. ISSN: 13640321. DOI: `10.1016/j.rser.2018.06.057`.

Fleuchaus, P., Schüppler, S., Bloemendal, M., Guglielmetti, L., Opel, O. and Blum, P. (2020). 'Risk analysis of High-Temperature Aquifer Thermal Energy Storage (HT-ATES)'. In: *Renewable and Sustainable Energy Reviews* 133, p. 110153. ISSN: 13640321. DOI: `10.1016/j.rser.2020.110153`.

Fleuchaus, P., Schüppler, S., Stemmle, R., Menberg, K. and Blum, P. (2021). 'Aquiferspeicher in Deutschland'. In: *Grundwasser* 26.2, pp. 123–134. ISSN: 1430-483X. DOI: `10.1007/s00767-021-00478-y`.

Fraunhofer ISI (2017). *Baseline scenario of the heating and cooling demand in buildings and industry in the 14 MSs until 2050*. Karlsruhe. URL: `https://heatroadmap.eu/wp-content/uploads/2018/11/HRE4_D3.3andD3.4.pdf`.

Frey, M., Bär, K., Stober, I., Reinecker, J., van der Vaart, J. and Sass, I. (2022). 'Assessment of deep geothermal research and development in the Upper Rhine Graben'. In: *Geothermal Energy* 10.1. DOI: `10.1186/s40517-022-00226-2`.

Fuhrmann, T. (2016). 'Surface Displacements from Fusion of Geodetic Measurement Techniques Applied to the Upper Rhine Graben Area'. PhD thesis. Karlsruhe: Karlsruhe Institute of Technology. DOI: `10.5445/IR/1000056073`.

Fulda, C., Hartmann, A. and Gorek, M. (2010). 'High resolution electrical imaging while drilling'. In: *SPWLA 51st Annual Logging Symposium*. SPWLA.

Gaillot, P., Brewer, T., Pezard, P. and Yeh, E.-C. (2007). 'Borehole Imaging Tools - Principles and Applications'. In: *Scientific Drilling* 5. DOI: `10.2204/iodp.sd.5.07s1.2007`.

Gallant, C., Zhang, J., Wolfe, C., Freeman, J., Al-Bazali, T. and Reese, M. (2007). 'Wellbore Stability Considerations for Drilling High-Angle Wells Through Finely Laminated Shale: A Case Study From Terra Nova'. In: *SPE Annual Technical Conference and Exhibition*. SPE.

Gambolati, G., Teatini, P. and Ferronato, M. (2005). 'Anthropogenic Land Subsidence'. In: *Encyclopedia of Hydrological Sciences*. Ed. by M. G. Anderson and J. J. McDonnell. Wiley. ISBN: 9780471491033. DOI: `10.1002/0470848944.hsa164b`.

Ganguly, S., Mohan Kumar, M. S., Date, A. and Akbarzadeh, A. (2017). 'Numerical investigation of temperature distribution and thermal performance while charging-discharging thermal energy in aquifer'. In: *Applied Thermal Engineering* 115, pp. 756–773. ISSN: 13594311. DOI: `10.1016/j.applthermaleng.2017.01.009`.

Gao, L., Zhao, J., An, Q., Liu, X. and Du, Y. (2019). 'Thermal performance of medium-to-high-temperature aquifer thermal energy storage systems'. In: *Applied Thermal Engineering* 146, pp. 898–909. ISSN: 13594311. DOI: `10.1016/j.applthermaleng.2018.09.104`.

Gao, L., Zhao, J., An, Q., Wang, J. and Liu, X. (2017). 'A review on system performance studies of aquifer thermal energy storage'. In: *Energy Procedia* 142, pp. 3537–3545. ISSN: 18766102. DOI: `10.1016/j.egypro.2017.12.242`.

Gaston, D., Newman, C., Hansen, G. and Lebrun-Grandié, D. (2009). 'MOOSE: A parallel computational framework for coupled systems of nonlinear equations'.

In: *Nuclear Engineering and Design* 239.10, pp. 1768–1778. ISSN: 00295493. DOI: `10.1016/j.nucengdes.2009.05.021`.

Gaucher, E., Schoenball, M., Heidbach, O., Zang, A., Fokker, P. A., van Wees, J.-D. and Kohl, T. (2015). 'Induced seismicity in geothermal reservoirs: A review of forecasting approaches'. In: *Renewable and Sustainable Energy Reviews* 52, pp. 1473–1490. ISSN: 13640321. DOI: `10.1016/j.rser.2015.08.026`.

GeORG-Projektteam (2013). *Geopotenziale des tieferen Untergrundes im Oberrheingraben, Fachlich-Technischer Abschlussbericht des Interreg-Projekts GeORG, Teil 3: Daten, Methodik, Darstellungsweise.* Ed. by G. Sokol and E. Nitsch. Freiburg i. Br.

Geertsma, J. (1973). 'Land Subsidence Above Compacting Oil and Gas Reservoirs'. In: *Journal of Petroleum Technology* 25.06, pp. 734–744. ISSN: 0149-2136. DOI: `10.2118/3730-PA`.

Gens, A., Garitte, B., Olivella, S. and Vaunat, J. (2009). 'Applications of multiphysical geomechanics in underground nuclear waste storage'. In: *Revue européenne de génie civil* 13.7-8, pp. 937–962. ISSN: 17747120. DOI: `10.3166/EJECE.13.937-962`.

Geuzaine, C. and Remacle, J.-F. (2009). 'Gmsh: A 3-D finite element mesh generator with built-in pre- and post-processing facilities'. In: *International Journal for Numerical Methods in Engineering* 79.11, pp. 1309–1331. ISSN: 00295981. DOI: `10.1002/nme.2579`.

Geyer, O. F., Gwinner, M. P. and Simon, T. (2011). *Geologie von Baden-Württemberg*. 5., völlig neu bearbeitete Auflage. Stuttgart: Schweizerbart. ISBN: 978-3-510-65267-9.

Gholami Korzani, M., Held, S. and Kohl, T. (2020). 'Numerical based filtering concept for feasibility evaluation and reservoir performance enhancement of hydrothermal doublet systems'. In: *Journal of Petroleum Science and Engineering*, p. 106803. ISSN: 09204105. DOI: `10.1016/j.petrol.2019.106803`.

Gholami Korzani, M., Nitschke, F., Held, S. and Kohl, T. (2019). 'The Development of a Fully Coupled Wellbore-Reservoir Simulator for Geothermal Application'. In: *Proceedings of the Geothermal Research Council Annual Meeting, GRC 2019*.

Gillen, M. E., Moody, B. and Dymmock, S. (2018). 'New LWD Technology Provides High-Resolution Images in Oil- and Water-Based Muds for Improved Decision Making in Real Time'. In: *Offshore Technology Conference*. OTC.

Gradstein, F. M., Anthonissen, E., Brunstad, H., Charnock, M., Hammer, O., Hellem, T. and Lervik, K. S. (2010). 'Norwegian Offshore Stratigraphic Lexicon

(NORLEX)'. In: *Newsletters on Stratigraphy* 44.1, pp. 73–86. ISSN: 0078-0421. DOI: `10.1127/0078-0421/2010/0005`.

Grandarovski, G. (1971). *Possibilites d'injection en couches profondes d'effluents industriels: Etude de quelques réservoirs sableux et gréseux dans les formations tertiaires du Nord de l'Alsace*. Strasbourg.

Grimmer, J. C., Ritter, J. R. R., Eisbacher, G. H. and Fielitz, W. (2017). 'The Late Variscan control on the location and asymmetry of the Upper Rhine Graben'. In: *International Journal of Earth Sciences* 106.3, pp. 827–853. ISSN: 1437-3254. DOI: `10.1007/s00531-016-1336-x`.

Guéguen, Y. and Palciauskas, V. (1994). *Introduction to the physics of rocks*. Princeton, NJ: Princeton Univ. Press. ISBN: 978-0-691-03452-2. URL: `https://permalink.obvsg.at/AC00960121`.

Guillou-Frottier, L., Carrė, C., Bourgine, B., Bouchot, V. and Genter, A. (2013). 'Structure of hydrothermal convection in the Upper Rhine Graben as inferred from corrected temperature data and basin-scale numerical models'. In: *Journal of Volcanology and Geothermal Research* 256, pp. 29–49. ISSN: 03770273. DOI: `10.1016/j.jvolgeores.2013.02.008`.

Hasnain, S. M. (1998). 'Review on sustainable thermal energy storage technologies, Part I: heat storage materials and techniques'. In: *Energy Conversion and Management* 39.11, pp. 1127–1138. ISSN: 01968904. DOI: `10.1016/S0196-8904(98)00025-9`.

Hayavi, M. T. and Abdideh, M. (2017). 'Determination of safe mud pressure window for different well trajectories and stress regimes during drilling operations'. In: *Geomechanics for Energy and the Environment* 12, pp. 14–20. ISSN: 23523808. DOI: `10.1016/j.gete.2017.07.002`.

Heimlich, C., Gourmelen, N., Masson, F., Schmittbuhl, J., Kim, S.-W. and Azzola, J. (2015). 'Uplift around the geothermal power plant of Landau (Germany) as observed by InSAR monitoring'. In: *Geothermal Energy* 3.1. DOI: `10.1186/s40517-014-0024-y`.

Hillis, R. R. and Nelson, E. J. (2005). 'In situ stresses in the North Sea and their applications: petroleum geomechanics from exploration to development'. In: *6th Petroleum Geology Conference*. Ed. by A. G. Doré and B. A. Vining, pp. 551–564.

Hillis, R. R. and Reynolds, S. D. (2000). 'The Australian stress map'. In: *Journal of the Geological Society* 157.5, pp. 915–921.

Hintze, M., Plasse, B., Bär, K. and Sass, I. (2018). 'Preliminary studies for an integrated assessment of the hydrothermal potential of the Pechelbronn Group in the northern Upper Rhine Graben'. In: *Advances in Geosciences* 45, pp. 251–258. DOI: `10.5194/adgeo-45-251-2018`.

Holgate, N. E., Jackson, C. A.-L., Hampson, G. J. and Dreyer, T. (2013). 'Sedimentology and sequence stratigraphy of the Middle–Upper Jurassic Krossfjord and Fensfjord formations, Troll Field, northern North Sea'. In: *Petroleum Geoscience* 19.3, pp. 237–258. ISSN: 1354-0793. DOI: `10.1144/petgeo2012-039`.

Holstenkamp, L., Meisel, M., Neidig, P., Opel, O., Steffahn, J., Strodel, N., Lauer, J. J., Vogel, M., Degenhart, H., Michalzik, D., Schomerus, T., Schönebeck, J. and Növig, T. (2017). 'Interdisciplinary Review of Medium-deep Aquifer Thermal Energy Storage in North Germany'. In: *Energy Procedia* 135, pp. 327–336. ISSN: 18766102. DOI: `10.1016/j.egypro.2017.09.524`.

Holzer, T. L. and Galloway, D. L. (2005). 'Impacts of land subsidence caused by withdrawal of underground fluids in the United States'. In: *Humans as Geologic Agents*. Ed. by J. Ehlen, W. C. Haneberg and R. A. Larson. Geological Society of America. ISBN: 9780813741161. DOI: `10.1130/2005.4016(08)`.

IEA (2017). *Energy Technology Perspectives 2017: Catalyzing Energy Technology Transformations*. Paris, France.

IEA (2023). *World Energy Outlook 2023*. Paris, France. URL: `https://www.iea.org/reports/world-energy-outlook-2023`.

INL (2023). *MOOSE Framework - Tensor Mechanics Module*. URL: `https://mooseframework.inl.gov/modules/tensor_mechanics/index.html`.

IPCC (2022). *Climate Change 2022: Mitigation of Climate Change: Contribution of Working Group III to the Sixth Assessment Report of the Intergovernmental Panel on Climate Change*. Ed. by P.R. Shukla, J. Skea, R. Slade, A. Al Khourdajie, R. van Diemen, D. McCollum, M. Pathak, S. Some, P. Vyas, R. Fradera, M. Belkacemi, A. Hasija, G. Lisboa, S. Luz, J. Malley. Cambridge University Press, Cambridge, UK and New York, NY, USA. DOI: `10.1017/9781009157926`. URL: `https://www.ipcc.ch/report/ar6/wg3/`.

IPCC (2023). *Climate Change 2023: Synthesis Report. Contribution of Working Groups I, II and III to the Sixth Assessment Report of the Intergovernmental Panel on Climate Change*. Ed. by Core Writing Team, H. Lee and J. Romero. Geneva, Switzerland. DOI: `10.59327/IPCC/AR6-9789291691647`.

Jaeger, J. C., Cook, N. G. W. and Zimmerman, R. W. (2007). *Fundamentals of rock mechanics*. 4. ed. Malden, MA: Blackwell Publ. ISBN: 978-0-632-05759-7. URL: `http://www.loc.gov/catdir/enhancements/fy0802/2006036480-b.html`.

Jahn, S., Mrugalla, S. and Stark, L. (2016). *F+E Endlagerung. Methodik und Anwendungsbezug eines Sicherheits- und Nachweiskonzeptes für ein HAW-Endlager im Tonstein. Endlagerstandortmodell SÜD (AnSichtT) Teil II: Zusammenstellung von Gesteinseigenschaften für den Langzeitsicherheitsnachweis*. Hannover, Germany.

Jantschik, R., Strauß, C. and Weber, R. (1996). 'Sequence-Stratigraphy as a Tool to Improve Reservoir Management of the Eich/Königsgarten Oil Field (Upper Rhine Graben, Germany)'. In: *SPE European Petroleum Conference*.

Jeon, J.-S., Lee, S.-R., Pasquinelli, L. and Fabricius, I. L. (2015). 'Sensitivity analysis of recovery efficiency in high-temperature aquifer thermal energy storage with single well'. In: *Energy* 90, pp. 1349–1359. ISSN: 03605442. DOI: `10.1016/j.energy.2015.06.079`.

Jin, W., Atkinson, T., Neupane, G. and McLing, T. (2022). 'Influence of mechanical deformation and mineral dissolution/precipitation on reservoir thermal energy storage'. In: *56th US Rock Mechanics/Geomechanics Symposium*.

Jin, W., Podgorney, R. and McLing, T. (2020). 'THM coupled numerical analysis on the geothermal energy storage & extraction in porous fractured reservoir'. In: *54th US Rock Mechanics/Geomechanics Symposium*.

Jin, W., Podgorney, R. and McLing, T. (2021). 'Geothermal battery optimization using stochastic hydro-thermal simulations and machine learning algorithms'. In: *55th US Rock Mechanics/Geomechanics Symposium*.

Johnsen, J. R., Rutledal, H. and Nilsen, D. E. (1995). 'Jurassic reservoirs; field examples from the Oseberg and Troll fields: Horda Platform area'. In: *Petroleum Exploration and Exploitation in Norway - Proceedings of the Norwegian Petroleum Society Conference, 9-11 December 1991, Stavanger, Norway*. Vol. 4. Norwegian Petroleum Society Special Publications. Elsevier, pp. 199–234. ISBN: 9780444815965. DOI: `10.1016/S0928-8937(06)80043-3`.

Kabus, F., Richlak, U., Wolfgramm, M., Gehrke, D., Beuster, H. and Seibt, A. (2008). 'Aquiferspeicherung in Neubrandenburg - Betriebsmonitoring über drei Speicherzyklen'. In: *Conference Proceedings Der Geothermiekongress 2008*, pp. 383–392.

Kabus, F. and Seibt, P. (2000). 'Aquifer thermal energy storage for the Berlin Reichstag building - New seat of the German parliament'. In: *Proceedings World Geothermal Congress 2000*.

Kastner, O., Norden, B., Klapperer, S., Park, S., Urpi, L., Cacace, M. and Blöcher, G. (2017). 'Thermal solar energy storage in Jurassic aquifers in Northeastern Germany: A simulation study'. In: *Renewable Energy* 104, pp. 290–306. ISSN: 09601481. DOI: `10.1016/j.renene.2016.12.003`.

Keranen, K. M., Savage, H. M., Abers, G. A. and Cochran, E. S. (2013). 'Potentially induced earthquakes in Oklahoma, USA: Links between wastewater injection and the 2011 Mw 5.7 earthquake sequence'. In: *Geology* 41.6, pp. 699–702. ISSN: 0091-7613. DOI: `10.1130/G34045.1`.

Kim, J., Lee, Y., Yoon, W. S., Jeon, J. S., Koo, M.-H. and Keehm, Y. (2010). 'Numerical modeling of aquifer thermal energy storage system'. In: *Energy* 35.12, pp. 4955–4965. ISSN: 03605442. DOI: `10.1016/j.energy.2010.08.029`.

Kirsch, C. (1898). 'Die Theorie der Elastizität und die Bedürfnisse der Festigkeitslehre'. In: *Zeitschrift des Vereines Deutscher Ingenieure* 42, pp. 797–807.

Kohl, T., Bächler, D. and Rybach, L. (2000). 'Steps towards a comprehensive thermo-hydraulic analysis of the HDR test site Soultz-sous-Forêts.' In: *Proc. World Geothermal Congress 2000*, pp. 3459–3464.

Kohl, T. and Hopkirk, R. J. (1995). '"FRACure" — A simulation code for forced fluid flow and transport in fractured, porous rock'. In: *Geothermics* 24.3, pp. 333–343. ISSN: 03756505. DOI: `10.1016/0375-6505(95)00012-F`.

Kohl, T., Andenmatten, N. and Rybach, L. (2003). 'Geothermal resource mapping—example from northern Switzerland'. In: *Geothermics* 32.4-6, pp. 721–732. ISSN: 03756505. DOI: `10.1016/S0375-6505(03)00066-X`.

Kraft, T., Mai, P. M., Wiemer, S., Deichmann, N., Ripperger, J., Kästli, P., Bachmann, C., Fäh, D., Wössner, J. and Giardini, D. (2009). 'Enhanced Geothermal Systems: Mitigating Risk in Urban Areas'. In: *Eos, Transactions, American Geophysical Union* 90.32, pp. 273–280.

Kristiansen, T. G. (2004). 'Drilling Wellbore Stability in the Compacting and Subsiding Valhall Field'. In: *IADC/SPE Drilling Conference 2004*. Society of Petroleum Engineers. DOI: `10.2118/87221-ms`.

Kristiansen, T. G. and Plischke, B. (2010). 'History Matched Full Field Geomechanics Model of the Valhall Field Including Water Weakening and Re-Pressurisation'. In: *SPE EUROPEC/EAGE Annual Conference and Exhibition*.

LBEG (2009). *Erdöl und Erdgas in der Bundesrepublik Deutschland 2009*. Hannover.

LBEG (2018). *Erdöl und Erdgas in der Bundesrepublik Deutschland (2018)*. Hannover.

LBEG (2022). *Die Erdölförderung Deutschlands von 1874 bis 2021: nach Feldern in Tabellenform*. Hannover, Germany. URL: `https://www.lbeg.niedersachsen.de/download/72477/Erdoelfoerderung_1874-2021.pdf`.

Lake, L. (2006). *Petroleum engineering handbook*. Richardson, TX: Society of Petroleum Engineers. ISBN: 978-1-55563-114-7.

Lee, K. S. (2010). 'A Review on Concepts, Applications, and Models of Aquifer Thermal Energy Storage Systems'. In: *Energies* 3.6, pp. 1320–1334. DOI: `10.3390/en3061320`.

Lee, K. S. (2013). *Underground thermal energy storage*. Green energy and technology. London: Springer. ISBN: 978-1-4471-4273-7. URL: `http://www.loc.gov/catdir/enhancements/fy1502/2012942260-b.html`.

Lempp, C., Witthaus, M., Röckel, T., Hecht, C. and Herold, M. (2010). 'Geomechanical behaviour of pelitic rocks with diagenetically caused different strengths becoming effective in deep geothermal boreholes'. In: *Zeitschrift der Deutschen Gesellschaft für Geowissenschaften* 161.4, pp. 379–400. ISSN: 1860-1804. DOI: `10.1127/1860-1804/2010/0161-0379`.

Li, G. (2016). 'Sensible heat thermal storage energy and exergy performance evaluations'. In: *Renewable and Sustainable Energy Reviews* 53, pp. 897–923. ISSN: 13640321. DOI: `10.1016/j.rser.2015.09.006`.

Li, Q., Bornemann, T., Rasmus, J., Wang, H., Hodenfield, K. and Lovell, J. (2001). 'Real-time logging-while-drilling image: Techniques and applications'. In: *SPWLA 42nd Annual Logging Symposium*. SPWLA.

Li, X., El Mohtar, C. S. and Gray, K. E. (2020). 'Modeling Progressive Wellbore Breakouts with Dynamic Wellbore Hydraulics'. In: *SPE Journal* 25.02, pp. 541–557. ISSN: 1086-055X. DOI: `10.2118/199887-PA`.

Lindsay, A. D. et al. (2022). '2.0 - MOOSE: Enabling massively parallel multiphysics simulation'. In: *SoftwareX* 20, p. 101202. ISSN: 23527110. DOI: `10.1016/j.softx.2022.101202`.

Lindsay, G., Ong, S., Morris, S. and Lofts, J. (2007). 'Wellbore Stress Indicators While Drilling: A Comparison of Induced Features from Wireline and LWD High-Resolution Electrical Images'. In: *SPE/IADC Drilling Conference and Exhibition 2007*. SPE.

Lipsey, L., Pluymaekers, M., Goldberg, T., van Oversteeg, K., Ghazaryan, L., Cloetingh, S. and van Wees, J.-D. (2016). 'Numerical modelling of thermal convection in the Luttelgeest carbonate platform, the Netherlands'. In: *Geothermics* 64, pp. 135–151. ISSN: 03756505. DOI: `10.1016/j.geothermics.2016.05.002`.

Liu, J., Li, R. and Sun, Z. (2015). 'Exploitation and Utilization Technology of Geothermal Resources in Oil Fields'. In: *Proceedings World Geothermal Congress 2015*.

Løseth, T. M., Ryseth, A. E. and Young, M. (2009). 'Sedimentology and sequence stratigraphy of the middle Jurassic Tarbert Formation, Oseberg South area (northern North Sea)'. In: *Basin Research* 21.5, pp. 597–619. ISSN: 0950091X. DOI: `10.1111/j.1365-2117.2009.00421.x`.

Maerten, L., Gillespie, P. and Daniel, J.-M. (2006). 'Three-dimensional geomechanical modeling for constraint of subseismic fault simulation'. In: *AAPG Bulletin* 90.9, pp. 1337–1358. ISSN: 0149-1423. DOI: `10.1306/03130605148`.

Magri, F., Bayer, U., Clausnitzer, V., Jahnke, C., Diersch, H.-J., Fuhrmann, J., Möller, P., Pekdeger, A., Tesmer, M. and Voigt, H. (2005). 'Deep reaching fluid flow close to convective instability in the NE German basin—results from water chemistry and numerical modelling'. In: *Tectonophysics* 397.1-2, pp. 5–20. ISSN: 00401951. DOI: `10.1016/j.tecto.2004.10.006`.

Magri, F., Bayer, U., Tesmer, M., Möller, P. and Pekdeger, A. (2008). 'Salinization problems in the NEGB: results from thermohaline simulations'. In: *International Journal of Earth Sciences* 97.5, pp. 1075–1085. ISSN: 1437-3254. DOI: `10.1007/s00531-007-0209-8`.

Major, M., Poulsen, S. E. and Balling, N. (2018). 'A numerical investigation of combined heat storage and extraction in deep geothermal reservoirs'. In: *Geothermal Energy* 6.1, p. 540. DOI: `10.1186/s40517-018-0089-0`.

Marschall, P. and Giger, S. (2014). *Technischer Bericht 14-02. SGT Etappe 2: Vorschlag weiter zu untersuchender geologischer Standortgebiete mit zugehörigen Standortarealen für die Oberflächenanlage: Geologische Grundlagen Dossier IV Geomechanische Unterlagen*. Wettingen, Switzerland.

Marsily, G. de (1993). *Quantitative hydrogeology: Groundwater hydrology for engineers*. 5. [print.] San Diego, Calif. u.a.: Acad. Press. ISBN: 9780122089152. URL: `https://permalink.obvsg.at/AC01376753`.

Martínez-Garzón, P., Kwiatek, G., Sone, H., Bohnhoff, M., Dresen, G. and Hartline, C. (2014). 'Spatiotemporal changes, faulting regimes, and source parameters of induced seismicity: A case study from The Geysers geothermal field'. In: *Journal of Geophysical Research: Solid Earth* 119.11, pp. 8378–8396. ISSN: 2169-9313. DOI: `10.1002/2014JB011385`.

Maurer, V., Gaucher, E., Grunberg, M., Koepke, R., Pestourie, R. and Cuenot, N. (2020). 'Seismicity induced during the development of the Rittershoffen geothermal field, France'. In: *Geothermal Energy* 8.1. DOI: `10.1186/s40517-020-0155-2`.

Meixner, J., Schill, E., Gaucher, E. and Kohl, T. (2014). 'Inferring the in situ stress regime in deep sediments: an example from the Bruchsal geothermal site'. In: *Geothermal Energy* 2.1. DOI: `10.1186/s40517-014-0007-z`.

Meixner, J., Schill, E., Grimmer, J. C., Gaucher, E., Kohl, T. and Klingler, P. (2016). 'Structural control of geothermal reservoirs in extensional tectonic settings: An example from the Upper Rhine Graben'. In: *Journal of Structural Geology* 82, pp. 1–15. ISSN: 01918141. DOI: `10.1016/j.jsg.2015.11.003`.

Meng, M., Zamanipour, Z., Miska, S., Yu, M. and Ozbayoglu, E. M. (2019). 'Dynamic Wellbore Stability Analysis Under Tripping Operations'. In: *Rock Mechanics and Rock Engineering* 52.9, pp. 3063–3083. ISSN: 0723-2632. DOI: `10.1007/s00603-019-01745-4`.

Meyer, N., Holehouse, S., Kirkwood, A., Zurcher, D., Chemali, R., Lofts, J. and Page, G. (2005). 'Improved LWD density images and their handling for thin bed definition and for hole shape visualization'. In: *SPWLA 46th Annual Logging Symposium*. SPWLA.

Millero, F. J., Chen, C.-T., Bradshaw, A. and Schleicher, K. (1980). 'A new high pressure equation of state for seawater'. In: *Deep Sea Research Part A. Oceanographic Research Papers* 27.3-4, pp. 255–264. ISSN: 01980149. DOI: `10.1016/0198-0149(80)90016-3`.

Mindlin, R. D. (1936). 'Force at a Point in the Interior of a Semi–Infinite Solid'. In: *Physics* 7.5, pp. 195–202. ISSN: 0148-6349. DOI: `10.1063/1.1745385`.

Moore, J., Chang, C., McNeill, L., Thu, M. K., Yamada, Y. and Huftile, G. (2011). 'Growth of borehole breakouts with time after drilling: Implications for state of stress, NanTroSEIZE transect, SW Japan'. In: *Geochemistry, Geophysics, Geosystems* 12.4, pp. 1–15. DOI: `10.1029/2010gc003417`.

Moos, D. and Zoback, M. D. (1990). 'Utilization of observations of well bore failure to constrain the orientation and magnitude of crustal stresses: application to continental, Deep Sea Drilling Project, and Ocean Drilling Program boreholes'. In: *Journal of Geophysical Research: Solid Earth* 95.B6, pp. 9305–9325.

Morris, A., Ferrill, D. A. and Brent Henderson, D. (1996). 'Slip-tendency analysis and fault reactivation'. In: *Geology* 24.3, p. 275. ISSN: 0091-7613. DOI: `10.1130/0091-7613(1996)024{\textless}0275:STAAFR{\textgreater}2.3.CO;2`.

Moscariello, A. (2019). 'Exploring for geo-energy resources in the Geneva Basin (Western Switzerland): opportunities and challenges'. In: *Swiss Bull. angew. Geol.* 24.2, pp. 105–124. URL: `https://archive-ouverte.unige.ch/unige:131617`.

Munns, J. W. (1985). 'The Valhall Field: a geological overview'. In: *Marine and Petroleum Geology* 2.1, pp. 23–43. ISSN: 02648172. DOI: `10.1016/0264-8172(85)90046-7`.

NASA, METI, AIST and Japan Spacesystems (2019). *ASTER Global Digital Elevation Model V003*. DOI: `10.5067/ASTER/ASTGTM.003`.

NLfB (1963). *Bericht über den Erdölbohr- und Förderverlauf im Jahre 1962 in Westdeutschland*. Hannover.

NPD (2022). *The Norwegian National Data Repository for Petroleum Data: Diskos Well Database*. URL: `https://www.npd.no/en/diskos/wells/`.

Nagel, N. B. (2001). 'Compaction and subsidence issues within the petroleum industry: From wilmington to ekofisk and beyond'. In: *Physics and Chemistry of the Earth, Part A: Solid Earth and Geodesy* 26.1-2, pp. 3–14. ISSN: 14641895. DOI: `10.1016/S1464-1895(01)00015-1`.

Nitschke, F., Ystroem, L., Bauer, F. and Kohl, T. (2023). 'Geochemical Constraints on the Operations of High Temperature Aquifer Energy Storage (HT-ATES) in Abandoned Oil Reservoirs'. In: *Proceedings of the 48th Workshop on Geothermal Reservoir Engineering*.

Nordell, B., Snijders, A. and Stiles, L. (2015). 'The use of aquifers as thermal energy storage (TES) systems'. In: *Advances in Thermal Energy Storage Systems*. Elsevier, pp. 87–115. ISBN: 9781782420880. DOI: `10.1533/9781782420965.1.87`.

Nur, A. and Byerlee, J. D. (1971). 'An exact effective stress law for elastic deformation of rock with fluids'. In: *Journal of Geophysical Research* 76.26, pp. 6414–6419. ISSN: 0148-0227. DOI: `10.1029/JB076i026p06414`.

O'Sullivan, M. J., Pruess, K. and Lippmann, M. J. (2001). 'State of the art of geothermal reservoir simulation'. In: *Geothermics* 30.4, pp. 395–429. ISSN: 03756505. DOI: `10.1016/S0375-6505(01)00005-0`.

Oerlemans, P., Drijver, B., Koenen, M., Koornneef, J., Dinkelman, D., Bos, W. and Godschalk, B. (2022). 'First field results on the technical risks and effectiveness of mitigation measures for the full scale HT-ATES demonstration project in Middenmeer'. In: *Proceedings of the European Geothermal Congress 2022*.

Okada, Y. (1992). 'Internal deformation due to shear and tensile faults in a half-space'. In: *Bulletin of the Seismological Society of America* 82.2, pp. 1018–1040. ISSN: 0037-1106.

Paksoy, H. and Beyhan, B. (2015). 'Thermal energy storage (TES) systems for greenhouse technology'. In: *Advances in Thermal Energy Storage Systems*. Elsevier, pp. 533–548. ISBN: 9781782420880. DOI: `10.1533/9781782420965.4.533`.

Permann, C. J., Gaston, D. R., Andrš, D., Carlsen, R. W., Kong, F., Lindsay, A. D., Miller, J. M., Peterson, J. W., Slaughter, A. E., Stogner, R. H. and Martineau,

R. C. (2020). 'MOOSE: Enabling massively parallel multiphysics simulation'. In: *SoftwareX* 11, p. 100430. ISSN: 23527110. DOI: `10.1016/j.softx.2020.100430`.

Peška, P. and Zoback, M. D. (1995). 'Compressive and tensile failure of inclined well bores and determination of in situ stress and rock strength'. In: *Journal of Geophysical Research: Solid Earth* 100.B7, pp. 12791–12811.

Pirkenseer, C., Berger†, J.-P. and Reichenbacher, B. (2013). 'The position of the Rupelian/Chattian boundary in the southern Upper Rhine Graben based on new records of microfossils'. In: *Swiss Journal of Geosciences* 106.2, pp. 291–301. ISSN: 1661-8726. DOI: `10.1007/s00015-013-0146-4`.

Pirkenseer, C., Spezzaferri, S. and Berger, J.-P. (2011). 'Reworked microfossils as a paleogeographic tool'. In: *Geology* 39.9, pp. 843–846. ISSN: 0091-7613. DOI: `10.1130/G32049.1`.

Pluymaekers, M., Veldkamp, H. and van Wees, J.-D. (2016). 'Doubletcalc 2D: A free geothermal simulator'. In: *Proceedings of the European Geothermal Congress 2016*. Ed. by EGEC.

Pribnow, D. and Schellschmidt, R. (2000). 'Thermal tracking of upper crustal fluid flow in the Rhine graben'. In: *Geophysical Research Letters* 27.13, pp. 1957–1960. ISSN: 00948276. DOI: `10.1029/2000GL008494`.

REN21 (2019). *Renewables 2019 Global Status Report*. Paris, France. URL: `https://www.ren21.net/wp-content/uploads/2019/05/gsr_2019_full_report_en.pdf`.

REN21 (2022). *Renewables 2022 Global Status Report*. Paris, France. URL: `https://www.ren21.net/wp-content/uploads/2019/05/GSR2022_Full_Report.pdf`.

Rad, F. M. and Fung, A. S. (2016). 'Solar community heating and cooling system with borehole thermal energy storage – Review of systems'. In: *Renewable and Sustainable Energy Reviews* 60, pp. 1550–1561. ISSN: 13640321. DOI: `10.1016/j.rser.2016.03.025`.

Reinhold, C., Schwarz, M., Bruss, D., Heesbeen, B., Perner, M. and Suana, M. (2016). 'The Northern Upper Rhine Graben : Re-dawn of a mature petroleum province?' In: *Swiss Bull. angew. Geol.* 21.2, pp. 35–56. DOI: `10.5169/seals-658196`.

Réveillère, A., Hamm, V., Lesueur, H., Cordier, E. and Goblet, P. (2013). 'Geothermal contribution to the energy mix of a heating network when using Aquifer Thermal Energy Storage: Modeling and application to the Paris basin'. In: *Geothermics* 47, pp. 69–79. ISSN: 03756505. DOI: `10.1016/j.geothermics.2013.02.005`.

Rinck, G. (1987). *Bilan de l'exploration et de l'exploitation du petrole en Alsace durant la derniere decennie*. Strasbourg.

Rotstein, Y., Behrmann, J. H., Lutz, M., Wirsing, G. and Luz, A. (2005). 'Tectonic implications of transpression and transtension: Upper Rhine Graben'. In: *Tectonics* 24.6, n/a–n/a. ISSN: 02787407. DOI: `10.1029/2005TC001797`.

Rudnicki, J. W. (1986). 'Fluid mass sources and point forces in linear elastic diffusive solids'. In: *Mechanics of Materials* 5, pp. 383–393.

Rudolph, B., Bremer, J., Stricker, K., Schill, E., Koenen, M., Dinkelman, D., van Wees, J.-D. and Kohl, T. (2022). 'Large-scale storage capacities as the backbone of a renewable energy system'. In: *Proceedings of the European Geothermal Congress 2022*.

Rutqvist, J., Rinaldi, A. P., Cappa, F., Jeanne, P., Mazzoldi, A., Urpi, L., Guglielmi, Y. and Vilarrasa, V. (2016). 'Fault activation and induced seismicity in geological carbon storage – Lessons learned from recent modeling studies'. In: *Journal of Rock Mechanics and Geotechnical Engineering* 8.6, pp. 789–804. ISSN: 16747755. DOI: `10.1016/j.jrmge.2016.09.001`.

SOG (2022). *Schlumberger Oilfield Glossary*. URL: `https://glossary.oilfield.slb.com/`.

Sanner, B. and Knoblich, K. (2004). *Thermische Untergrundspeicherung auf höherem Temperaturniveau: Begleitforschung mit Messprogramm Aquiferspeicher Reichstag: Schlussbericht zum FuE-Vorhaben 0329809 B*. Gießen.

Sattel, G. (1982). 'In-situ-Bestimmung thermischer Gesteinsparameter aus ihrem Zusammenhang mit Kompressionswellengeschwindigkeit und Dichte'. Dissertation. Karlsruhe: Universität Karlsruhe.

Sauer, K., Nägele, R. and Tietze, R. (1981). *Geothermische Synthese des Oberrheingrabens zwischen Karlsruhe und Mannheim (Anteil Baden-Württemberg)*. Freiburg i. Br.

Sayegh, M. A., Jadwiszczak, P., Axcell, B. P., Niemierka, E., Bryś, K. and Jouhara, H. (2018). 'Heat pump placement, connection and operational modes in European district heating'. In: *Energy and Buildings* 166, pp. 122–144. ISSN: 03787788. DOI: `10.1016/j.enbuild.2018.02.006`.

Schad, A. (1962). 'Das Erdölfeld Landau'. In: *Abh. Geol. Landesamt Baden-Württemberg* 4, pp. 81–101.

Scheck, M. (1997). *Dreidimensionale Strukturmodellierung des Nordostdeutschen Beckens unter Einbeziehung von Krustenmodellen*. Potsdam.

Schnaebelé, R. (1948). 'Monographie géologique du champ pétrolifière de Pechelbronn'. In: *Mém. Serv. Carte geol d'Alsace et Lorraine* 7.

Schoenball, M., Sahara, D. P. and Kohl, T. (2014). 'Time-dependent brittle creep as a mechanism for time-delayed wellbore failure'. In: *International Journal of Rock Mechanics and Mining Sciences* 70, pp. 400–406. DOI: `10.1016/j.ijrmms.2014.05.012`.

Seithel, R., Gaucher, E., Mueller, B., Steiner, U. and Kohl, T. (2019). 'Probability of fault reactivation in the Bavarian Molasse Basin'. In: *Geothermics* 82, pp. 81–90. ISSN: 03756505. DOI: `10.1016/j.geothermics.2019.06.004`.

Skarphagen, H., Banks, D., Frengstad, B. S. and Gether, H. (2019). 'Design Considerations for Borehole Thermal Energy Storage (BTES): A Review with Emphasis on Convective Heat Transfer'. In: *Geofluids* 2019, pp. 1–26. ISSN: 14688115. DOI: `10.1155/2019/4961781`.

Skinner, B. J. (1966). 'Section 6: Thermal Expansion'. In: *Handbook of Physical Constants*. Ed. by S. P. Clark. Vol. 97. Geological Society of America Memoirs. Geological Society of America, pp. 75–96. DOI: `10.1130/MEM97-p75`.

Smith, L. and Chapman, D. S. (1983). 'On the thermal effects of groundwater flow: 1. Regional scale systems'. In: *Journal of Geophysical Research* 88.B1, p. 593. ISSN: 0148-0227. DOI: `10.1029/JB088iB01p00593`.

Sommer, W. T., Doornenbal, P. J., Drijver, B. C., van Gaans, P. F. M., Leusbrock, I., Grotenhuis, J. T. C. and Rijnaarts, H. H. M. (2014). 'Thermal performance and heat transport in aquifer thermal energy storage'. In: *Hydrogeology Journal* 22.1, pp. 263–279. ISSN: 1431-2174. DOI: `10.1007/s10040-013-1066-0`.

Sommer, W., Valstar, J., van Gaans, P., Grotenhuis, T. and Rijnaarts, H. (2013). 'The impact of aquifer heterogeneity on the performance of aquifer thermal energy storage'. In: *Water Resources Research* 49.12, pp. 8128–8138. ISSN: 00431397. DOI: `10.1002/2013WR013677`.

Sommer, W., Valstar, J., Leusbrock, I., Grotenhuis, T. and Rijnaarts, H. (2015). 'Optimization and spatial pattern of large-scale aquifer thermal energy storage'. In: *Applied Energy* 137, pp. 322–337. ISSN: 03062619. DOI: `10.1016/j.apenergy.2014.10.019`.

Steiger, R. P. and Leung, P. K. (1992). 'Quantitative Determination of the Mechanical Properties of Shales'. In: *SPE Drilling Engineering* 7.03, pp. 181–185. ISSN: 0885-9744. DOI: `10.2118/18024-PA`.

Straub, E. W. (1962). 'Die Erdöl- und Erdgaslagerstätten in Hessen und Rheinhessen'. In: *Abh. Geol. Landesamt Baden-Württemberg* 4, pp. 123–136.

Stricker, K., Egert, R., Schill, E. and Kohl, T. (2024). 'Risk of surface movements and reservoir deformation for high-temperature aqifer thermal energy storage (HT-ATES)'. In: *Geothermal Energy* 12.4. DOI: `10.1186/s40517-024-00283-9`. URL: `https://doi.org/10.1186/s40517-024-00283-9`.

Stricker, K., Grimmer, J. C., Egert, R., Bremer, J., Korzani, M. G., Schill, E. and Kohl, T. (2020). 'The Potential of Depleted Oil Reservoirs for High-Temperature Storage Systems'. In: *Energies* 13.24, p. 6510. DOI: `10.3390/en13246510`.

Stricker, K., Schimschal, S., Müller, B., Wessling, S., Bender, F. and Kohl, T. (2023). 'Importance of drilling-related processes on the origin of borehole breakouts — Insights from LWD observations'. In: *Geomechanics for Energy and the Environment* 34, p. 100463. ISSN: 23523808. DOI: `10.1016/j.gete.2023.100463`.

Stricker, K., Schimschal, S., Wessling, S., Müller, B., Bender, F. and Kohl, T. (2022). 'LWD breakout data from hydrocarbon fields in the Norwegian North Sea: Mendeley Data, V1'. In: DOI: `10.17632/r3tb2bdr7s.1`.

Suckale, J. (2009). 'Induced Seismicity in Hydrocarbon Fields'. In: vol. 51. Advances in Geophysics. Elsevier, pp. 55–106. ISBN: 9780123749116. DOI: `10.1016/S0065-2687(09)05107-3`.

Sui, D., Wiktorski, E., Røksland, M. and Basmoen, T. A. (2019). 'Review and investigations on geothermal energy extraction from abandoned petroleum wells'. In: *Journal of Petroleum Exploration and Production Technology* 9.2, pp. 1135–1147. ISSN: 2190-0558. DOI: `10.1007/s13202-018-0535-3`.

Thompson, N., Andrews, J. S., Reitan, H. and Rodrigues, N. E. T. (2022). 'Data Mining of In-Situ Stress Database Towards Development of Regional and Global Stress Trends and Pore Pressure Relationships'. In: *SPE Norway Subsurface Conference*.

Tingay, M., Reinecker, J. and Müller, B. (2008). *Borehole breakout and drilling-induced fracture analysis from image logs: World Stress Map Project Guidelines: Image Logs*.

Tollefsen, E., Weber, A., Kramer, A., Sirkin, G., Hartman, D. and Grant, L. (2007). 'Logging While Drilling Measurements: From Correlation to Evaluation'. In: *International Oil Conference and Exhibition*. SPE.

Tollefson, J. (2018). 'IPCC says limiting global warming to 1.5 °C will require drastic action'. In: *Nature* 562.7726, pp. 172–173. DOI: `10.1038/d41586-018-06876-2`.

Turgut, B., Dasgan, H. Y., Abak, K., Paksoy, H., Evliya, H. and Bozdag, S. (2009). 'AQUIFER THERMAL ENERGY STORAGE APPLICATION IN GREEN-

HOUSE CLIMATIZATION'. In: *Acta Horticulturae* 807, pp. 143–148. ISSN: 0567-7572. DOI: `10.17660/ActaHortic.2009.807.17`.

Twiss, R. J. and Moores, E. M. (2007). *Structural geology*. 2. ed., 2. print. New York, NY u.a.: Freeman. ISBN: 978-0-7167-4951-6. URL: `https://permalink.obvsg.at/AC06547787`.

Umweltbundesamt (2023). *Erneuerbare Energien in Deutschland: Daten zur Entwicklung im Jahr 2022*. Dessau-Roßlau. URL: `https://www.umweltbundesamt.de/sites/default/files/medien/1410/publikationen/2023-03-16_uba_hg_erneuerbareenergien_dt_bf.pdf`.

Van Thienen-Visser, K. and Fokker, P. A. (2017). 'The future of subsidence modelling: compaction and subsidence due to gas depletion of the Groningen gas field in the Netherlands'. In: *Netherlands Journal of Geosciences* 96.5, s105–s116. ISSN: 0016-7746. DOI: `10.1017/njg.2017.10`.

Vidal, R., Olivella, S., Saaltink, M. W. and Diaz-Maurin, F. (2022). 'Heat storage efficiency, ground surface uplift and thermo-hydro-mechanical phenomena for high-temperature aquifer thermal energy storage'. In: *Geothermal Energy* 10.1. DOI: `10.1186/s40517-022-00233-3`.

Vilarrasa, V., Carrera, J., Olivella, S., Rutqvist, J. and Laloui, L. (2019). 'Induced seismicity in geologic carbon storage'. In: *Solid Earth* 10.3, pp. 871–892. DOI: `10.5194/se-10-871-2019`.

Wang, S., Yan, J., Li, F., Hu, J. and Li, K. (2016). 'Exploitation and Utilization of Oilfield Geothermal Resources in China'. In: *Energies* 9.10, p. 798. DOI: `10.3390/en9100798`.

Wesselink, M., Liu, W., Koornneef, J. and van den Broek, M. (2018). 'Conceptual market potential framework of high temperature aquifer thermal energy storage - A case study in the Netherlands'. In: *Energy* 147, pp. 477–489. ISSN: 03605442. DOI: `10.1016/j.energy.2018.01.072`.

Wessling, S., Bartetzko, A., Pei, J. and Dahl, T. (2012). 'Automation in Wellbore Stability Workflows'. In: *SPE Intelligent Energy International*. SPE.

Wessling, S., Dahl, T. and Pantic, D. (2011). 'Challenges and Solutions for Automated Wellbore Status Monitoring - Breakout Detection as an Example'. In: *SPE Digital Energy Conference and Exhibition*. SPE.

Winterleitner, G., Schütz, F., Wenzlaff, C. and Huenges, E. (2018). 'The Impact of Reservoir Heterogeneities on High-Temperature Aquifer Thermal Energy Storage Systems. A Case Study from Northern Oman'. In: *Geothermics* 74, pp. 150–162. ISSN: 03756505. DOI: `10.1016/j.geothermics.2018.02.005`.

Wirth, E. (1962). *Die Erdöllagerstätten Badens*. Freiburg im Breisgau.

Wolf, A. and Hinners, G. (2013). 'Antrennung gelöster Kohlenwasserstoffe aus Lagerstättenwasser'. In: *DGMK/ÖGEW-Frühjahrstagung des Fachbereiches Aufsuchung und Gewinnung am 18. und 19. April 2013 in Celle*. Tagungsbericht / DGMK, Deutsche Wissenschaftliche Gesellschaft für Erdöl, Erdgas und Kohle. Hamburg: DGMK. ISBN: 978-3-941721-31-9.

Worum, G., van Wees, J.-D., Bada, G., van Balen, R. T., Cloetingh, S. and Pagnier, H. (2004). 'Slip tendency analysis as a tool to constrain fault reactivation: A numerical approach applied to three–dimensional fault models in the Roer Valley rift system (southeast Netherlands)'. In: *Journal of Geophysical Research: Solid Earth* 109.B2. ISSN: 2169-9313. DOI: `10.1029/2003JB002586`.

Xiao, X., Jiang, Z., Owen, D. and Schrank, C. (2016). 'Numerical simulation of a high-temperature aquifer thermal energy storage system coupled with heating and cooling of a thermal plant in a cold region, China'. In: *Energy* 112, pp. 443–456. ISSN: 03605442. DOI: `10.1016/j.energy.2016.06.124`.

Yang, J. H., Jiang, Q. H., Zhang, Q. B. and Zhao, J. (2018). 'Dynamic stress adjustment and rock damage during blasting excavation in a deep-buried circular tunnel'. In: *Tunnelling and Underground Space Technology* 71, pp. 591–604. ISSN: 08867798. DOI: `10.1016/j.tust.2017.10.010`.

Yang, T., Liu, W., Kramer, G. J. and Sun, Q. (2021). 'Seasonal thermal energy storage: A techno-economic literature review'. In: *Renewable and Sustainable Energy Reviews* 139, p. 110732. ISSN: 13640321. DOI: `10.1016/j.rser.2021.110732`.

Zang, A., Oye, V., Jousset, P., Deichmann, N., Gritto, R., McGarr, A., Majer, E. and Bruhn, D. (2014). 'Analysis of induced seismicity in geothermal reservoirs – An overview'. In: *Geothermics* 52, pp. 6–21. ISSN: 03756505. DOI: `10.1016/j.geothermics.2014.06.005`.

Zeynali, M. E. (2012). 'Mechanical and physico-chemical aspects of wellbore stability during drilling operations'. In: *Journal of Petroleum Science and Engineering* 82-83, pp. 120–124. ISSN: 09204105. DOI: `10.1016/j.petrol.2012.01.006`.

Zhang, B., Matchinski, E. J., Chen, B., Ye, X., Jing, L. and Lee, K. (2019). 'Marine Oil Spills—Oil Pollution, Sources and Effects'. In: *World Seas: An Environmental Evaluation*. Elsevier, pp. 391–406. ISBN: 9780128050521. DOI: `10.1016/B978-0-12-805052-1.00024-3`.

Zoback, M. D. (2007). *Reservoir geomechanics*. Cambridge University Press % Proceedings.

Zoback, M. D. and Gorelick, S. M. (2012). 'Earthquake triggering and large-scale geologic storage of carbon dioxide'. In: *Proceedings of the National Academy of Sciences of the United States of America* 109.26, pp. 10164–10168. DOI: `10.1073/pnas.1202473109`.

Zoback, M. D. and Zinke, J. C. (2002). 'Production-induced Normal Faulting in the Valhall and Ekofisk Oil Fields'. In: *The Mechanism of Induced Seismicity*. Ed. by C. I. Trifu. Basel: Birkhäuser Basel, pp. 403–420. ISBN: 978-3-7643-6653-7. DOI: `10.1007/978-3-0348-8179-1{\textunderscore}17`.

van Heekeren, V. and Bakema, G. (2015). 'Country Update the Netherlands'. In: *World Geothermal Congress 2015*.

van Thienen-Visser, K. and Breunese, J. N. (2015). 'Induced seismicity of the Groningen gas field: History and recent developments'. In: *The Leading Edge* 34.6, pp. 664–671. ISSN: 1070-485X. DOI: `10.1190/tle34060664.1`.

van Wees, J. D., Buijze, L., van Thienen-Visser, K., Nepveu, M., Wassing, B., Orlic, B. and Fokker, P. A. (2014). 'Geomechanics response and induced seismicity during gas field depletion in the Netherlands'. In: *Geothermics* 52, pp. 206–219. ISSN: 03756505. DOI: `10.1016/j.geothermics.2014.05.004`.

van Wees, J.-D., Osinga, S., Van Thienen-Visser, K. and Fokker, P. A. (2018). 'Reservoir creep and induced seismicity: inferences from geomechanical modeling of gas depletion in the Groningen field'. In: *Geophysical Journal International* 212.3, pp. 1487–1497. ISSN: 0956-540X. DOI: `10.1093/gji/ggx452`.

van Wees, J.-D., Pluymaekers, M., Bonté, D., van Gessel, S. and Veldkamp, H. (2017). 'Unlocking Geothermal Energy from Mature Oil and Gas Basins: A Success Story from the Netherlands'. In: *Perspectives for Geothermal Energy in Europe*. Ed. by R. Bertani. WORLD SCIENTIFIC (EUROPE), pp. 187–214. ISBN: 978-1-78634-231-7. DOI: `10.1142/9781786342324{\textunderscore}0007`.

van Wees, J.-D., Pluymaekers, M., Osinga, S., Fokker, P., Van Thienen-Visser, K., Orlic, B., Wassing, B., Hegen, D. and Candela, T. (2019). '3-D mechanical analysis of complex reservoirs: a novel mesh-free approach'. In: *Geophysical Journal International* 219.2, pp. 1118–1130. ISSN: 0956-540X. DOI: `10.1093/gji/ggz352`.

van der Baan, M. and Calixto, F. J. (2017). 'Human–induced seismicity and large–scale hydrocarbon production in the USA and C anada'. In: *Geochemistry, Geophysics, Geosystems* 18.7, pp. 2467–2485. ISSN: 1525-2027. DOI: `10.1002/2017GC006915`.

van der Gun, J., Aureli, A. and Merla, A. (2016). ‘Enhancing Groundwater Governance by Making the Linkage with Multiple Uses of the Subsurface Space and Other Subsurface Resources’. In: *Water* 8.6, p. 222. DOI: `10.3390/w8060222`.

DECLARATION OF AUTHORSHIP

CHAPTER 3: THE POTENTIAL OF DEPLETED OIL RESERVOIRS FOR HIGH-TEMPERATURE STORAGE SYSTEMS

Stricker, K., Grimmer, J. C., Egert, R., Bremer, J., Gholami Korzani, M., Schill, E., Kohl, T. (2020). 'The Potential of Depleted Oil Reservoirs for High-Temperature Storage Systems'. In: *Energies 13:24*, pp. 6510. DOI: 10.3390/en13246510.

This study was conducted within the Helmholtz program 'Renewable Energies' under the topic 'Geothermal Energy Systems' and the Helmholtz Climate Initiative (HI-CAM), which is funded by the Helmholtz Association's Initiative and Networking Fund. The study was further supported by EnBW, Energie Baden-Württemberg AG, Germany.

In this study, I compiled geological and petrophysical data of depleted and currently operating oil fields in the Upper Rhine Graben (URG). I developed a simplified generic thermo-hydraulic numerical model to simulate high-temperature aquifer thermal energy storage (HT-ATES) in depleted oil reservoirs in the URG using the MOOSE-based modeling software TIGER. I performed sensitivity analyses on the most relevant modeling parameters to investigate their influence on the recovery efficiency and storage capacity of the HT-ATES system. Additionally, the borehole configuration was varied from a purely vertical setup to also include horizontal sections. Based on the modeling results and the compiled geological and petrophysical data, I estimated the general storage potential of depleted oil reservoirs in the URG for HT-ATES. I visualized and interpreted the results. I wrote the manuscript of the paper.

CHAPTER 4: RISK OF SURFACE MOVEMENTS AND RESERVOIR DEFORMATION FOR HIGH-TEMPERATURE AQUIFER THERMAL ENERGY STORAGE (HT-ATES)

Stricker, K., Egert, R., Schill, E., Kohl, T. (2024). 'Risk of surface movements and reservoir deformation for high-temperature aquifer thermal energy storage (HT-ATES)'. In: *Geothermal Energy 12:4*. DOI: 10.1186/s40517-024-00283-9.

This work was partly supported by the German Federal Ministry for Economic Affairs and Climate Action (BMWK) and the Project Management Jülich (PtJ) under the grant agreement number 03EE4008C associated with the INSIDE project (https://inside-geothermie.de/en/inside-en/). This study was conducted as part of the subtopic "Geoenergy" in the program "MTET - Materials and Technologies for the Energy Transition" of the Helmholtz Association.

In this study, I developed a simplified generic thermo-hydraulic-mechanical numerical model to simulate high-temperature aquifer thermal energy storage (HT-ATES) in depleted oil reservoirs in the URG using the MOOSE-based modeling software TIGER. I set the focus on investigating the influence of HT-ATES on the (geo-)mechanical response of the reservoir and the ground surface. I investigate the contributions of poro- and thermoelasticity on displacements in the reservoir and how these displacements are translated into ground surface movements. I evaluated the influence of cyclic HT-ATES operation on the stress distribution in the reservoir, with a particular focus on the respective contributions of poro- and thermoelasticity. I performed sensitivity analyses on the most relevant modeling parameters to investigate their influence on ground surface movements induced by the HT-ATES operation. I visualized and interpreted the results. I wrote the manuscript of the paper.

CHAPTER 5: RISK ASSESSMENT OF FAULT REACTIVATION AND INDUCED SEISMICITY FOR HIGH-TEMPERATURE HEAT STORAGE (HT-ATES) AT THE DEEPSTOR DEMONSTRATOR IN THE UPPER RHINE GRABEN

Stricker, K., Fokker, P., van Wees, Jan-Diederik, Schill, E., Kohl, T. (2024). 'Risk assessment of fault reactivation and induced seismicity for high-temperature heat storage (HT-ATES) at the DeepStor demonstrator in the Upper Rhine Graben'. Prepared for submission to *Geothermics*.

This study was conducted as part of the subtopic "Geoenergy" in the program "MTET - Materials and Technologies for the Energy Transition" of the Helmholtz Association.

In this study, I developed a numerical model of the planned HT-ATES demonstrator DeepStor based on a subsurface geological model. I simulated the thermo-hydraulic response of the HT-ATES operation using the modeling software DoubletCalc3D. Afterward, the modeling results were used as input for a semi-analytical stress calculation on a fault next to the storage operation. I employed two approaches to evaluate the hazard of fault reactivation and induced seismicity associated with HT-ATES operation at the DeepStor site: 1) Assuming an unstressed fault, the hazards were evaluated based on the slip tendency distribution at the fault of interest. 2) Assuming a nearly critically stressed fault, the sensitivity of Coulomb stress changes at the fault, which could potentially lead to failure, was assessed. I performed sensitivity analyses (including a Monte Carlo analysis) on the most relevant modeling parameters to investigate their influence on fault reactivation and induced seismicity associated with the HT-ATES operation. I visualized and interpreted the results. I wrote the manuscript of the paper.

PUBLICATIONS

PEER-REVIEWED PUBLICATIONS

Stricker, K., Fokker, P., van Wees, J.-D., Schill, E., Kohl, T. (2024). 'Risk assessment of fault reactivation and induced seismicity for high-temperature heat storage (HT-ATES) at the DeepStor demonstrator in the Upper Rhine Graben'. Prepared for submission to *Geothermics*.

Stricker, K., Egert, R., Schill, E., Kohl, T. (2024). 'Risk of surface movements and reservoir deformation for high-temperature aquifer thermal energy storage (HT-ATES)'. In *Geothermal Energy 12:4*. DOI: 10.1186/s40517-024-00283-9.

Stricker, K., Schimschal S., Müller, B., Wessling, S., Bender, F., Kohl, T. (2023).' Importance of drilling-related processes on the origin of borehole breakouts – Insights from LWD observations'. In: *Geomechanics for Energy and the Environment 34*. DOI: 10.1016/j.gete.2023.100463.

Yan, G., Busch, B., Egert, R., Esmaeilpour, M., Stricker, K., Kohl, T. (2023). 'Transport mechanisms of hydrothermal convection in faulted tight sandstones'. In: *Solid Earth 14:3*, pp. 293–310. DOI: 10.5194/se-14-293-2023.

Stricker, K., Grimmer, J. C., Egert, R., Bremer, J., Gholami Korzani, M., Schill, E., Kohl, T. (2020). 'The Potential of Depleted Oil Reservoirs for High-Temperature Storage Systems'. In: *Energies 13:24*, pp. 6510. DOI: 10.3390/en13246510.

FURTHER PUBLICATIONS

Stricker, K., Egert, R., Grimmer, J., Gholami Korzani, M., Schill, E., Kohl, T. (2022). 'Thermal-hydraulic-mechanical (THM) modeling of high-temperature heat storage using DeepStor as a case study'. In: *Proceedings European Geothermal Congress 2022*. ISBN: 978-2-9601946-2-3.

Stricker, K., Grimmer, J, Egert, R., Bremer, J., Gholami Korzani, M., Schill, E., Kohl, T. (2020). 'The Potential of High-Temperature Storage Systems in Depleted Oil Reservoirs in the Upper Rhine Graben'. In: *Proceedings 1st Geoscience & Engineering in Energy Transition Conference*. DOI: 10.3997/2214-4609.202021041.

Stricker, K., Grimmer, J., Dashti, A., Egert, R., Gholami Korzani, M., Meixner, J., Schaetzler, K., Schill, E., Kohl, T. (2020). 'Utilization of Abandoned Hydrocarbon Reservoirs for Deep Geothermal Heat Storage'. In: *Proceedings DGMK/ÖGEW Frühjahrstagung*. ISBN: 978-3-947716-04-3.

Stricker, K., Schimschal, S., Kohl, T., Meixner, J., Müller, B., Wessling, S. (2019). 'Drilling Induced Borehole Breakouts – New Insights From LWD Data Analysis'. In *Proceedings EAGE/BVG/FKPE Joint Workshop on Borehole Geophysics and Geothermal Energy*. DOI: 10.3997/2214-4609.201903161.

PRESENTATIONS WITH ABSTRACTS

Stricker, K., Fokker, P., van Wees, J.-D., Marelis, A., Schill, E., Kohl, T. (2023). 'Risk assessment of fault reactivation and induced seismicity for the high-temperature heat storage demonstrator, DeepStor, in the Upper Rhine Graben'. *European Geothermal Workshop 2023*. Utrecht, Netherlands.

Stricker, K., Fokker, P., van Wees, J.-D., Marelis, A., Schill, E., Kohl, T. (2023). 'Risk assessment of fault reactivation and induced seismicity for high-temperature storage in former hydrocarbon reservoirs in the Upper Rhine Graben'. *Der Geothermiekongress 2023*, Essen, Germany.

Stricker, K., Egert, R., Fokker, P., Vardon, P., van Wees, J.-D., Schill, E., Kohl, T. (2023). 'Risk assessment of high-temperature heat storage (HT-ATES) at the DeepStor demonstrator'. *European Geosciences Union General Assembly 2023*. Wien, Austria.

Stricker, K., Egert, R., Grimmer, J. C., Gholami Korzani, M., Schill, E., Kohl, T. (2022). 'Thermal-hydraulic-mechanical (THM) modeling of high-temperature heat storage using DeepStor as a case study'. *European Geothermal Congress 2022*. Berlin, Germany.

Stricker, K., Grimmer, J., Egert, R., Bremer, J., Gholami Korzani, M., Schill, E., Kohl, T. (2021). 'THM modeling of former hydrocarbon reservoirs for high-temperature heat storage'. *Joint EAGE/BVG/FKPE Workshop Hydro- Thermal- Mechanical Modelling (THM) and Ground Truth*. Online.

Stricker, K., Egert, R., Grimmer, J. C., Gholami Korzani, M., Bauer, F., Schill, E., Kohl, T. (2021). 'Thermisch-Hydraulisch-Mechanische (THM) Modellierung von Hochtemperatur-Wärmespeicherung am Fallbeispiel DeepStor'. *Der Digitale Geothermiekongress 2021*. Online.

Stricker, K., Schimschal, S., Müller, B., Wessling, S., Bender, F., Kohl, T. (2021). 'New insights on the origin of borehole breakouts from LWD observations' *Celle Drilling - International Conference and Exhibition for Advanced Drilling Technology 2021*. Online.

Stricker, K., Grimmer, J., Egert, R., Bremer, J., Gholami Korzani, M., Schill, E., Kohl, T. (2021). 'Numerische und chemische Modellierung der Speicherstrukturen im tiefen Tertiär / Numerical and chemical modeling of the deep tertiary reservoir structures'. *GeoTHERM - expo & congress 2021*. Online.

Stricker, K., Grimmer, J. C., Egert, R., Bremer, J., Gholamikorzani, M., Schill, E., Kohl, T. (2021). 'Utilization of Former Hydrocarbon Reservoirs for High-temperature Heat Storage'. *DGMK/ÖGEW Frühjahrstagung "Shaping the Energy Transition with Upstream and Storage Technologies" 2021*. Online.

Stricker, K. (2020). 'Utilization of depleted hydrocarbon reservoirs for deep geothermal heat storage'. *Symposium "Energie-Campus" der Stiftung Energie & Klimaschutz im Rahmen des Ideenwettbewerbs "Energie und Umwelt - Meine Idee für morgen" 2020*. Online.

Stricker, K., Grimmer, J., Egert, R., Bremer, J., Gholami Korzani, M., Schill, E., Kohl, T. (2020). 'The potential of high-temperature storage systems in depleted oil reservoirs in the Upper Rhine Graben'. *1st Geoscience & Engineering in Energy Transition Conference 2020*. Online.

Stricker, K., Grimmer, J., Egert, R., Bremer, J., Gholami Korzani, M., Schill, E., Kohl, T. (2020). 'Wärmespeicherung in ehemaligen Kohlenwasserstofflagerstätten des Oberrheingrabens'. *Der digitale Geothermiekongress 2020*. Online.

Stricker, K., Grimmer, J., Egert, R., Bremer, J., Gholami Korzani, M., Schill, E., Kohl, T. (2020). 'Potential für Wärmespeicherung in ehemaligen Kohlenwasserstofflagerstätten des Oberrheingrabens'. *25. Dresdner Fernwärme-Kolloquium 2020*. Online.

Stricker, K., Grimmer, J., Egert, R., Bremer, J., Gholami Korzani, M., Schill, E., Kohl, T. (2020). 'Heat storage in depleted hydrocarbon reservoirs of the Upper Rhine Graben'. *8th European Geothermal Workshop 2020*. Online.

Stricker, K., Grimmer, J., Meixner, J., Dashti, A., Egert, R., Gholamikorzani, M., Schaetzler, K., Schill, E., Kohl, T. (2020). 'Utilization of abandoned hydrocarbon reservoirs for deep geothermal heat storage'. *European Geosciences Union General Assembly 2020*. Online. DOI: 10.5194/egusphere-egu2020-20723.

Stricker, K., Schimschal, S., Kohl, T., Meixner, J., Müller, B., Wessling, S. (2019). 'Drilling induced borehole breakouts - new insights from LWD data analysis'. *EAGE/BVG/FKPE Joint Workshop on Borehole Geophysics and Geothermal Energy 2019*. München, Germany.

Stricker, K., Schimschal, S., Kohl, T., Meixner, J., Müller, B., Wessling, S. (2019). 'Analysis of image and drilling logs for formation instability uncertainty analysis'. *Student Technical Congress 2019*. Aachen, Germany.

Stricker, K., Schimschal, S., Kohl, T., Meixner, J., Müller, B., Wessling, S. (2019). 'Drilling induced borehole breakouts - new insights from LWD data analysis'. *7th European Geothermal Workshop 2019*. Karlsruhe, Germany.

Stricker, K., Grimmer, J., Meixner, J., Schill, E., Kohl, T. (2019). 'Utilization of abandoned hydrocarbon reservoir for deep geothermal heat storage'. *7th European Geothermal Workshop 2019*. Karlsruhe, Germany.

Stricker, K., Krasnonosov, K., Wittmann, N. (2019). 'New Approach to Link Depletion and Induced Seismicity in Lower Saxony Gas Fields'. *5th GSSPE YP Workshop 2019*. Lüneburg, Germany.

ACKNOWLEDGMENTS

A very large group of people have supported me during my PhD and I would like to say thank you to all of them. However, there are some people I would like to address separately, without all of you this thesis would not have been possible.

First of all, I would like to thank my supervisor Thomas Kohl for giving me the opportunity to pursue my PhD. Thank you for your great ideas and support throughout the last 4.5 years. I am very grateful for your support, especially in complicated times.

Thank you to Phil Vardon, who thankfully agreed to be the co-supervisor of this thesis.

I would also like to thank Jan-Diederik and Peter for your supervision during my great time at TNO in Utrecht and extend my thanks to everyone who made me feel very welcome during my stay in Utrecht.

A big thank you is reserved for the whole Geothermal working group. I enjoyed my time here a lot, you always made me feel welcome at work. Thanks for all the fruitful (more or less) scientific discussions and all the fun we had together during coffee breaks or after hours. However, I want to give some extra thanks to some people in the group, without whom this thesis would not have been possible.

Many thanks to Eva, Jens, and Maziar for your support, especially during the beginning of my thesis, when I was still figuring out how science works.

A special thank you goes to Robert for (unofficially) supervising me during the majority of my thesis and your large support on all numerical issues throughout my thesis (even after you left KIT).

A big thank you I also want to say to Silke for all your help with KIT administration and bureaucracy.

Last but not least, I want to thank my parents and my whole family for your unconditional support during my whole life.

A

STRICKER ET AL. (2020) APPENDIX

Table A.1: Parameter variation used for the parameter sensitivity analysis on recovery efficiency.

Parameter		**Variation**							
Reservoir permeability [m^2]	Vertical well			6.6×10^{-15}	10^{-14}	3.3×10^{-14}	6.6×10^{-14}	10^{-13}	3.3×10^{-13}
	Horizontal well	10^{-15}	3.3×10^{-15}	6.6×10^{-15}	10^{-14}	3.3×10^{-14}	6.6×10^{-14}	10^{-13}	3.3×10^{-13}
Reservoir thickness [m]		5	10	20					
Thermal conductivity [$W.m^{-1}K^{-1}$]	Reservoir (λ_{res})	2	2.5	3					
	Cap rock (λ_{cap})	1	1.4	2					
Injection/production flow rate [Ls^{-1}]		1	2	5	7.5	10			

Table A.2: Overview of 41 wells from 10 depleted French and German oil fields in the URG that are used to assess their potential for HT-ATES in Chapter 3.5. The data also include values obtained from log calculations. The reservoir permeability (10^{-15} – 4×10^{-12} m²) and thickness (3 – 48 m) distributions of these wells map representative values of the data basis in the Upper Rhine Graben (see Chapter 3.2). The abbreviations of the reservoir formations stand for the following: Niederrödern Fm. (NF), Cyrena marls (CyM), Meletta beds (Me), Pechelbronn Fm. (PBF), Eocene basis sands (EBS), Série grise (comprising, among others, Cyrena marls and Meletta beds; SG), and Beinheim sandstones (BS).

Field	Well	Reservoir Formation	Reservoir Depth [m]	Reservoir Thickness [m]	Permeability Min [m²]	Permeability Avg [m²]	Permeability Max [m²]	Source
Eich-Königsgarten	Eich 27	PBF	1760–1855	20–30	10^{-14}	2×10^{-13}	4×10^{-12}	Jantschik et al. (1996)
Eschau	1	NF, CyM, Me	280–450	34	10^{-14}	3.2×10^{-14}	10^{-13}	Grandarovski (1971)
	2	SG	375–552	17,5	10^{-14}	3.2×10^{-14}	10^{-13}	Grandarovski (1971)
	3	SG	390.2–608.3	15	10^{-14}	3.2×10^{-14}	10^{-13}	Grandarovski (1971)
	5	SG	599.7–633.3	11	10^{-14}	3.2×10^{-14}	10^{-13}	Grandarovski (1971)
	6	NF	294–352	10	10^{-14}	3.2×10^{-14}	10^{-13}	Grandarovski (1971)
	6	SG	475–575	7	10^{-14}	3.2×10^{-14}	10^{-13}	Grandarovski (1971)
	7	NF		30	10^{-14}	3.2×10^{-14}	10^{-13}	Grandarovski (1971)
	7	SG	433–465	22	10^{-14}	3.2×10^{-14}	10^{-13}	Grandarovski (1971)
	9	NF	318–324	6	10^{-14}	3.2×10^{-14}	10^{-13}	Grandarovski (1971)
	9	SG	450–555	19	10^{-14}	3.2×10^{-14}	10^{-13}	Grandarovski (1971)
	10	SG	432–520	48	10^{-14}	3.2×10^{-14}	10^{-13}	Grandarovski (1971)
	11	NF	287–392	28	10^{-14}	3.2×10^{-14}	10^{-13}	Grandarovski (1971)
	11	SG	400–620	25	10^{-14}	3.2×10^{-14}	10^{-13}	Grandarovski (1971)
	101	NF	290–440	37	10^{-14}	3.2×10^{-14}	10^{-13}	Grandarovski (1971)
	102	NF	305–490	41	10^{-14}	3.2×10^{-14}	10^{-13}	Grandarovski (1971)
	103	NF	290–440	23	10^{-14}	3.2×10^{-14}	10^{-13}	Grandarovski (1971)
	104	NF	543–550	3	10^{-14}	3.2×10^{-14}	10^{-13}	Grandarovski (1971)

Field	Well	Reservoir Formation	Reservoir Depth [m]	Reservoir Thickness [m]	Permeability Min [m²]	Permeability Avg [m²]	Permeability Max [m²]	Source
Landau	104	EBS		25	5×10^{-15}	7.1×10^{-15}	10^{-14}	Böcker (2015), Boigk (1981) Schad (1962)
Leopoldshafen	N1	NF	1196	5.6	2.4×10^{-15}	1.4×10^{-14}	7.7×10^{-14}	Bruss (2000)
	N1a	Me	1233.3–1237.4	18	1.3×10^{-15}	2.2×10^{-15}	3.8×10^{-15}	Bruss (2000)
Neureut	2H	NF	1107–1111.2	9	1.1×10^{-13}	1.1×10^{-13}	1.1×10^{-13}	Bruss (2000)
Offenbach		CyM, Me		11	4×10^{-13}	6.6×10^{-13}	1.1×10^{-12}	Boigk (1981), Durst (1991)
Schaffhouse		BS	950	7.5–20	10^{-12}	10^{-12}	10^{-12}	Grandarovski (1971)
	2		950	10	10^{-12}	10^{-12}	10^{-12}	Grandarovski (1971)
	3		945	15	10^{-12}	10^{-12}	10^{-12}	Grandarovski (1971)
Souffenheim	8	SG	188–193	5	10^{-13}	10^{-13}	10^{-13}	Grandarovski (1971)
	10		166–183	11	10^{-13}	10^{-13}	10^{-13}	Grandarovski (1971)
	11		150–167	15	10^{-13}	10^{-13}	10^{-13}	Grandarovski (1971)
	12		160–180	18	10^{-13}	10^{-13}	10^{-13}	Grandarovski (1971)
	13		162–180	13	10^{-13}	10^{-13}	10^{-13}	Grandarovski (1971)
	14		151–167	10	10^{-13}	10^{-13}	10^{-13}	Grandarovski (1971)
	17		151–223	36	10^{-13}	10^{-13}	10^{-13}	Grandarovski (1971)
	18		158–187	10	10^{-13}	10^{-13}	10^{-13}	Grandarovski (1971)
	20		169–183	8	10^{-13}	10^{-13}	10^{-13}	Grandarovski (1971)
	21		161–176	13	10^{-13}	10^{-13}	10^{-13}	Grandarovski (1971)
	24		167–187	16	10^{-13}	10^{-13}	10^{-13}	Grandarovski (1971)
	25		149–223	36	10^{-13}	10^{-13}	10^{-13}	Grandarovski (1971)
Stockstadt		PBF	1400–1700	10	10^{-15}	3.2×10^{-15}	10^{-14}	Boigk (1981)
Weingarten	Wiag-Deutag 204	Me	408.2	7	1.4×10^{-13}	1.4×10^{-13}	1.4×10^{-13}	Böcker (2015), Bruss (2000)
	Wiag-Deutag 205		243.3	16	1.3×10^{-13}	1.3×10^{-13}	1.3×10^{-13}	Bruss (2000)

STRICKER ET AL. (2023) IMPORTANCE OF DRILLING-RELATED PROCESSES ON THE ORIGIN OF BOREHOLE BREAKOUTS - INSIGHTS FROM LWD OBSERVATIONS

This chapter was published in Geomechanics for Energy and the Environment 34 (2023) 100463[1]
DOI: 10.1016/j.gete.2023.100463

ABSTRACT

Logging while drilling (LWD) images are widely used for the analysis of borehole stability. In this context, borehole breakouts are a crucial indication of rock failure developing when the circumferential stress around the borehole exceeds the yield value of the rock. This study investigates the impact of drilling-related processes (DRPs) on the origin of borehole breakouts. DRPs, for instance, include connections or tripping operations. For this purpose, we analyze data from 12 boreholes in different geological settings throughout the Norwegian and Danish North Sea, containing a total of 208 borehole breakouts. The extensive data acquisition of LWD offers the unique possibility to link the imaging to real-time drilling operations and to monitor anomalies of e.g., bottom hole pressure. These records allow us to connect any thermal, hydraulic, or mechanical interaction next to the borehole wall to perturbations of the stress field. This analysis resulted in an apparent strong coincidence of borehole breakouts, representing major stress perturbations, with DRPs. The causal relationship is highlighted by one order of magnitude higher occurrence of DRPs in depth sections containing breakouts. Major pressure reductions in the annulus of the borehole seem to be the most significant cause of drilling-related wellbore failures. This applies in particular to shutting off the pumps during connections, where pressure reductions of up to 16 % of the annulus pressure led to higher circumferential stresses. This process will increase the likelihood of compressive and shear failure, therefore causing borehole breakouts. These observations further open the perspective of counteracting wellbore instabilities by pressure modification. In addition to the initiation of breakouts, their temporal evolution – as seen in relogs – can also be ascribed to DRPs. This study indicates that not only plasticity but also

---

[1] The work published in this journal does not constitute an inherent part of this thesis but was compiled during this PhD thesis and represents a supplement thereof.

mechanical interaction from DRPs is a key driver of the temporal growth of borehole breakouts.

B.1 INTRODUCTION

In drilling operations, wellbore stability is crucial for preserving the drilling investments (Albukhari et al., 2018; Ashena et al., 2020; Steiger and Leung, 1992; Wessling et al., 2012). In a given stress field, possible wellbore instabilities are typically due to low rock strength resulting in compressive borehole breakouts, which potentially lead to the collapse of the borehole (Zoback, 2007). Using image logs, the orientation of the stress components (Bell, 1996; Brudy and Kjorholt, 1992; Tingay et al., 2008) and the stress magnitude around wellbores (Barton et al., 1988; Moos and Zoback, 1990; Zoback, 2007) are determined. Borehole instabilities can further be used to derive characteristic geomechanical parameters for reservoir models (Zoback, 2007). In the past, they have been monitored mostly by wireline logging (Aadnoy, Bell et al., 1998; Gaillot et al., 2007; Tingay et al., 2008), whereas recently, logging while drilling (LWD) tools are gaining more importance (Li et al., 2001; Tollefsen et al., 2007; Wessling et al., 2012, 2011).

Borehole breakouts develop when concentrations of the circumferential stress around the borehole exceed the yield value of the rock. Their average orientation corresponds to the minimum stress component S_{min}. In contrast, tensile fractures (e.g. hydraulic fractures or so-called drilling-induced fractures (DIFs)) originate from the drilling process and are caused when the circumferential stress falls below the tensile strength of the rock (Hillis and Reynolds, 2000; Zoback, 2007). They are oriented in the direction of the maximum stress component, S_{max}. The azimuthal orientation and inclination of a borehole in the subsurface additionally influence the circumferential stress state and thus the development of both, breakouts and tensile fractures (Peška and Zoback, 1995). Besides their geological origin – thus as a consequence of high tectonic differential stresses, they may be caused through drilling operations (AlBahrani and Morita, 2020; Kristiansen, 2004; Zeynali, 2012). Mechanical erosion by reciprocation or rotation of the drill string or hydraulic pressure through excessive mud circulation are typical sources that yield stress concentrations locally exceeding the yield value of the rock (Gallant et al., 2007). Also, an inappropriate selection of the mud weight may induce borehole instabilities when the pressure level cannot be kept in the window defined by collapse and fracture pressure (Hayavi and Abdideh, 2017; Zeynali, 2012). Throughout this paper, we will refer to all compressive borehole failure phenomena as "borehole breakouts". This includes borehole breakouts occurring in areas with extensive reaming or circulation.

While the physical principles for the occurrence of borehole breakouts are mathematically well described, their temporal development remains controversial. Whereas Zoback (2007) states that breakouts tend to deepen over time but generally show no increase in width, other studies describe a temporal growth of breakouts in all dimensions (Moore et al., 2011; Schoenball et al., 2014). Advances in technologies, such as enhanced digital communication between bit and surface or recent improvements in LWD measurements (e.g. high-resolution LWD images) are now opening the pathway for real-time wellbore stability services (Wessling et al., 2011). Especially, it is now possible to investigate the dynamic processes in a borehole and to combine multiple types of LWD datasets with drilling-related processes (DRPs).

Today modern LWD techniques enable the combined evaluation of formation imaging with operational drilling data. In this paper, we utilize the extensive data acquisition of LWD to expand the standard interpretation of borehole breakouts, as being the result of heterogeneities in stress state and rock strength, towards the impact of DRPs. This innovative approach leads to new data analysis methods that allow for the differentiation between drilling-induced breakouts and breakouts of purely geological origin. We analyze LWD image logs and their relog sections (image recordings during tripping procedures) as well as other real-time measured drilling-related parameters (such as the mud pressure) by extending standard industry application tools to improve the general understanding of the origin of breakouts. Next, the impact of DRPs on the dynamic hydraulic conditions in the borehole and their implications on the origin of breakouts is investigated. Finally, relog sections and recordings of multiple imaging tools are analyzed to investigate the time-dependent behavior of breakouts. Conclusively, this should deepen the understanding of the influence of DRPs on the development of breakouts and open the perspective of adapting drilling operations to counteract wellbore instabilities.

B.2 BACKGROUND INFORMATION

B.2.1 *Geomechanical models around boreholes*

Failure of rock depends on the effective stress and is well described in literature on rock mechanics (e.g. Jaeger et al., 2007; Zoback, 2007). The Mohr circle illustrates the relationship between the failure of rock and the stress state (Figure B.1). The yield envelope indicates the limit of elasticity, beyond which permanent deformations occur. At low confining pressures, the yield envelope can be interpreted as a failure threshold. Various failure criteria are described in literature (e.g. Colmenares and Zoback, 2002), a detailed consideration of these criteria is beyond the scope of this study. The increase of pore pressure leads to a reduction of the effective stress and consequently to a stress state closer to failure (Jaeger et al., 2007).

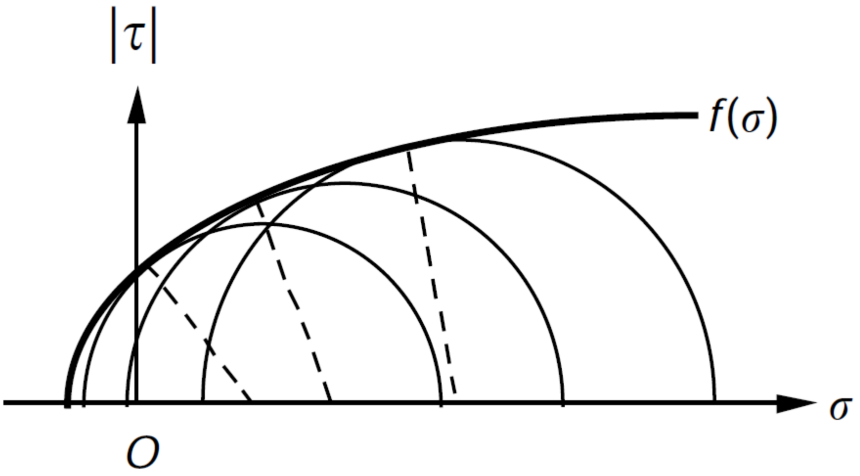

Figure B.1: Mohr circles with yield envelope (or failure curve) f(σ) defining the limit of elasticity, beyond which permanent deformations (or failure for low confining pressure) occur. σ is the stress normal to the failure plane, τ is the shear stress on the failure plane. Source: Adapted from Jaeger et al. (2007).

In a far-field stress field, the removal of material through the drilling process leads to a stress concentration around the borehole (Kirsch, 1898; Zoback, 2007). When the maximum magnitude of effective circumferential stress $\sigma_{\theta\theta,eff}^{max}$ exceeds the yield value, borehole breakouts will occur at this orientation. At the wall of a vertical borehole where the normal vertical stress is one of the principal stresses, $\sigma_{\theta\theta,eff}^{max}$ is parallel to the minimum principal horizontal stress, S_h, and is given by

$$\sigma_{\theta\theta,eff}^{max} = 3S_H - S_h - 2P_0 - \Delta P - \sigma^{\Delta T} \tag{B.1}$$

where S_H is the maximum principal horizontal stress, P_0 the pore pressure of the formation, ΔP the difference between the wellbore pressure and the formation pore pressure, and $\sigma^{\Delta T}$ the thermal stress caused by the temperature difference between drilling mud and formation (Zoback, 2007).

Assuming a given stress state, it becomes clear that the variation of the pressure in the wellbore affects $\sigma_{\theta\theta,eff}^{max}$ and thus the stability of the wellbore. A pressure decrease in the wellbore (resulting in a decrease of ΔP) increases $\sigma_{\theta\theta,eff}^{max}$ and can lead to the occurrence of breakouts. In contrast, a pressure increase decreases the effective circumferential stress, potentially leading to tensional failure (Zoback, 2007). Even though the calculation of the circumferential stress for inclined boreholes is slightly more complex (see Peška and Zoback, 1995), the effect of changes in the wellbore pressure are comparable to vertical boreholes.

In standard breakout models, changes in the circumferential stress around the borehole are considered for the initial development of breakouts (e.g. Zoback, 2007). These static models neglect dynamic changes. However, in other disciplines, the dynamic impact on pressure/stress changes is well-known e.g. for water hammering in pipes (Bergant et al., 2006) or during blasting excavation in tunnels (e.g. Yang et al., 2018). For the latter, blast loading and transient unloading lead to strong dynamic stress fluctuations in the range of milliseconds that finally lead to the failure of the rock (Yang et al., 2018). We may consider this recurring influence as being an approximate analog of the short-time-scale pressure perturbations occurring during DRPs, which lead to dynamic changes in the effective circumferential stress.

B.2.2 *Drilling-related processes and logging while drilling (LWD) borehole measurements*

Various processes are necessary for a smooth continuation of a drilling operation, including connections and different variations of pipe trips (SOG, 2022). These processes can cause thermal, hydraulic, and mechanical loads on the rock surrounding the borehole, potentially leading to conditions that are favorable for borehole instabilities. In this section, we will shortly review how these perturbations may impact the mechanical stability of the rock, especially at the bottom of the borehole (e.g. Bagala et al., 2010). Both the execution of connections (i.e. stop pumping down hole; SOG, 2022) and tripping operations (pulling the drill string out of the borehole; Lake, 2006) lead to pressure reductions (swab pressures) within the annulus of the borehole. This further leads to an increase in the effective circumferential stress around the borehole wall (Zoback, 2007); consequently, borehole breakouts may occur if the yield value at the borehole wall is exceeded by this stress (Hillis and Reynolds, 2000). On the contrary, lowering the drill string too fast into the hole leads to significant pressure increases (surging effect; Burkhardt, 1961). This decreases the effective circumferential stress around the borehole, facilitating the generation of tensile fractures if this stress drops below the tensile strength of the rock (Zoback, 2007). In addition to their influence on hydraulic conditions within a borehole, tripping operations also exert mechanical loads on boreholes and may affect their stability. They are frequently part of so-called reaming operations to clean a borehole, e.g. before a connection, and are reported to have a direct (negative) influence on the wellbore stability (Bagala et al., 2010; Dupriest et al., 2010).

In contrast to wireline logging, which relies mainly on gravity to run the device into the borehole, LWD measurements can be easily utilized in inclined or horizontal boreholes with complex geometries. The LWD tools are installed within drill collars at the lowermost part of the drill string and allow the real-time quantification of perturbations (e.g. pressure) while drilling as well as their impact on wellbore stability (Ellis and Singer, 2007). The acquisition timing of LWD is the central advantage compared to wireline logging (Lindsay et al., 2007), opening the pathway to investigate the relationship between DRPs and borehole breakouts.

Among other measurements, LWD tools can be used to record an image of the wellbore wall by measuring different physical properties. This includes, for instance, acoustic, density, and electrical images (Fulda et al., 2010). Acoustic image logs are based on the reflection of acoustic signals from the borehole wall, allowing to record both the amplitude and the travel time of these signals with a large bandwidth of possible applications (Gillen et al., 2018). Density image logs rely on the scattering of Gamma rays that are sent into the formation depending on the density thereof. Borehole enlargements become apparent through measurement values below the expected bulk density due to increased drilling fluid fraction in the measured sample volume (Meyer et al., 2005). Electrical image logs enable the measurement of the shape of the borehole wall based on the resistivity contrast between the drilling mud and the formation surrounding the borehole. The shallow depth of investigation of ca. 0.5 in for modern LWD tools allows for a detailed shape determination of borehole enlargements (Ekstrom et al., 1987; Fulda et al., 2010).

B.2.3 *Data and methods*

Data overview

The data sets used for this study were acquired in multiple geological settings throughout the Norwegian and Danish North Sea (Evans et al., 2003). In total, we analyzed data originating from 12 boreholes located in six hydrocarbon fields with varying inclinations, mostly either strongly inclined or horizontal (Table B.1). The data comprise various image log types that range from electrical, over density, to low- and high-resolution acoustic images. Furthermore, supplementary information from caliper, pressure, and temperature logs were utilized. Table B.1 gives an overview of the used logs for each investigated borehole.

Most of the data originate from the reservoir level of the respective wells. Logs acquired in the Northern Viking Graben cover thinly laminated mud rocks of the Late Jurassic age Heather Formation and interbedded sandstone, paleosol, and coal intervals of the Middle Jurassic Brent Group (Oseberg Field). On the Horda Platform, image logs originate from Middle to Late Jurassic tide-dominated delta sandstone sequences (Troll Field). Data from the Central Graben and the Norwegian-Danish Basin are mainly acquired in chalk carbonates of the Late Cretaceous age (Valhall Field). To extend the variety of lithofacies covered, additional data from in-situ and weathered magmatic basements were used (Rolvsnes Field) (Gradstein et al., 2010). All formations within the sedimentary sequence are situated in a normal faulting environment, close to isotropic stresses (Thompson et al., 2022). The stress regime in the basement is assumed to be unrelated to that in the sedimentary sequence (Hillis and Nelson, 2005). References to the geology and the geomechanics of the hydrocarbon fields are provided in Table B.1.

Table B.1: Overview of the analyzed data in this study (confidential data was omitted). All data is older than two years and thus available on the Diskos Well Database of the Norwegian Petroleum Directorate (NPD, 2022). Non-confidential analyzed data has been made available in an online repository (Stricker et al., 2022).

Field name	**Well name**	**Depth extent (MD) [m]**	**Inclination [°]**	**Analyzed logs**	**Sources for geology and geomechanics**
Oseberg	30/6-E-5 B	3647-6259	65.7-90.0	ACL, DEN, CAL, P, T	Refs. A,B
	30/6-E-8 A	3490-5837	63.4-90.0	ACL, DEN, CAL, P, T	
	30/6-H-2	2741-4022	54.3-88.4	ACL, ACH, DEN, CAL, P, T	
	30/6-H-8 AY1	3308-4219	81.2-90.0	ACL, DEN, CAL, P, T	
	30/9-B-11 B	5170-6149	69.7-90.0	ACL, DEN, CAL, P, T	
	30/9-F-17 CT2	4800-5531	74.590.0	ACL, DEN, CAL, P, T	
Rolvsnes	16/1-28 S	3244-4782	86.8-90.0	ACL, DEN, CAL, P, T	Ref. C
Troll	31/2-L-22	2001-4805	88.0-90.0	ACL, DEN, CAL, P, T	Refs. A,D,E
	31/2-N-22	2151-4345	88.0-90.0	ACL, DEN, CAL, P, T	
Valhall	2/8-G-17	3459-5289	4.1-90.0	ACL, ACH, DEN, CAL, P, T	Refs. F,G,H

Analyzed logs: ACL (low-resolution ultrasonic image log), ACH (high-resolution ultrasonic image log), DEN (density image log), CAL (caliper log), P (measurements of the annulus and stand pipe pressures), T (measurements of the annulus temperatures). References: A (Johnsen et al., 1995), B (Løseth et al., 2009), C (Ceccato et al., 2021), D (Bretan et al., 2011), E (Holgate et al., 2013), F (Munns, 1985), G (Zoback and Zinke, 2002), H (Kristiansen and Plischke, 2010).

Analysis concept

To evaluate the relationship between breakouts and DRPs, multiple image log types (acoustic, density, and electrical) are used to identify breakouts. The identification of the breakouts and the discrimination of them from other deformations has been performed according to prior research on this topic (Alizadeh et al., 2015; Tingay et al., 2008; Wessling et al., 2011). The analysis of caliper logs further supports the selection of breakouts. The occurrence and frequency of DRPs and their relationship to the origin of borehole breakouts are analyzed under the application of different methods. First, the frequency of occurrence of DRPs is determined for all selected breakouts, and subdivided into pump shut-off events (e.g. connections) as well as minor (< 5 m) and major (> 5 m) tripping operations. Afterward, the frequency of occurrence of tripping operations and pump shut-off events within and outside of breakout sections is compared. Further, mud pressure anomalies in the wellbore are analyzed due to their strong influence on the effective circumferential stress at the borehole wall. This may impact the wellbore stability, e.g., when the effective circumferential stress exceeds the yield value of the rock. The described procedure was applied to the borehole image, supplementary caliper, and pressure data that was obtained from 12 boreholes located in six hydrocarbon fields.

In the case image relog data (data recorded over the same depth interval, but at later times during tripping operations) are available for the respective borehole breakout, potential temporal geometrical changes, as described in Zoback (2007), can be analyzed. These time-dependent changes of breakouts were additionally used for the identification of a relationship between the breakout occurrence and the performed DRPs during this time frame.

B.3 RESULTS

B.3.1 *Observed borehole instabilities*

In the investigated data sets breakouts occur frequently. In total, 208 breakout sections were identified. Detailed information on their location (i.e. the well they have been identified in) and their geometry (i.e. their depth, length, or orientation) is provided in the supplementary material of this study (Stricker et al., 2022). Figure B.2 shows examples of breakout sections that were identified in a high-resolution ultrasonic image (Figure B.2a) and a high-resolution electrical image (Figure B.2b).

Various other borehole instabilities can be observed in the investigated datasets. Frequently, breakout sections contain superimpositions of a breakout and an additional borehole enlargement, which e.g. occurs along a bedding plane. This kind of superimposition occurs for a third of all breakout sections (70 out of 208) and is mostly related to beds with a lower density than the surrounding rock. Reasons for these enlargements comprise generally unstable formations, shales that are prone to roof collapse due to reduced arch support, or sloughing. Thus, in such formations, the origin of borehole breakouts may be further linked to the respective bedding structure, leading to failure structures with a broader azimuthal extent. Very rarely breakouts are superimposed by borehole enlargements that extend over the complete azimuthal section of the well (i.e. washouts) or with the scraping of the bit on either the low (probably a key seat) or the top side of the borehole. All mentioned instability phenomena are not limited to a superimposition with breakouts but can also occur individually. In conclusion, however, most investigated breakout sections (138 out of 208) seem to be unrelated to a specific lithology or other geological reasons.

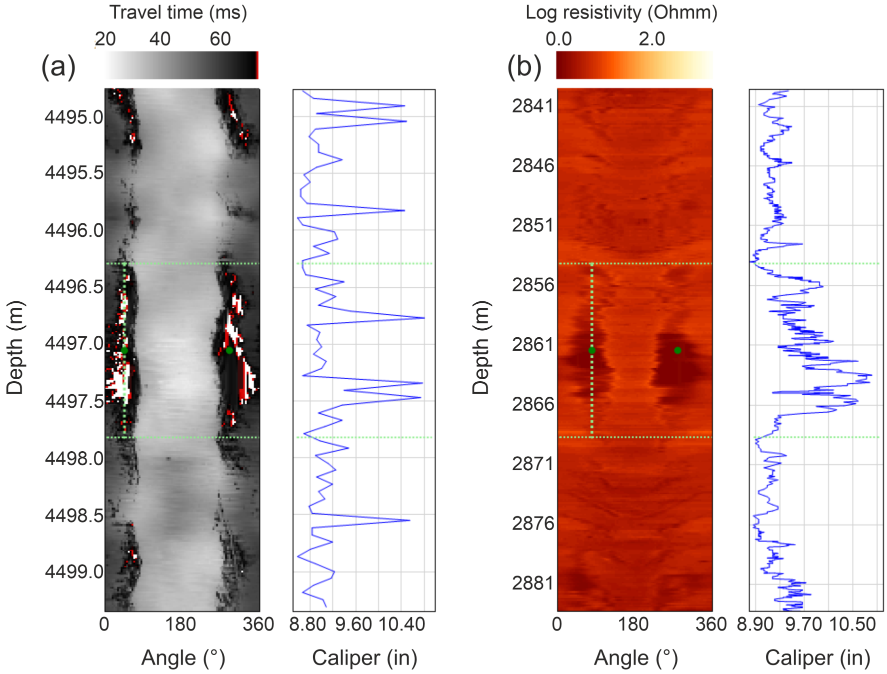

Figure B.2: Examples of breakouts that were identified in a high-resolution (256-sector) LWD ultrasonic image obtained from well 2/8-G-17 in the Valhall field on the Norwegian continental shelf (a) and an electrical image obtained from the Valdemar field on the Danish continental shelf (b). The identification of the breakouts was aided by the recomputed average caliper log (blue curves). The horizontal dashed green lines indicate the vertical extent of each breakout, whereas the filled green circles mark the orientation of the two opposed parts of the respective breakout.

B.3.2 *Relationship between drilling-related processes and borehole breakouts*

The investigated data, comprising 208 identified breakouts in 16 runs of 12 different boreholes, is impacted by a large number of the before-described DRPs. The analysis of the data shows that 190 out of 208 breakouts are associated with one or more of these processes. This is illustrated by the grey bar in Figure B.3a. Conversely, this means that only 18 breakouts (or ca. 10 % of the investigated data) occur without any relation to drilling procedures and are most likely caused by the stress state around the borehole. With only one exception, drilling-controlled breakout sections are always accompanied by at least one pump shut-off event (red bar in Figure B.3a). This can be expected as connections need to be performed to continue the drilling operation. In addition to pump shut-offs, minor tripping events (< 5 m; green bar), without any relation to connections, and major tripping events (> 5 m; blue bar), such as wiper trips, are present in ca. 30 % of the investigated breakouts.

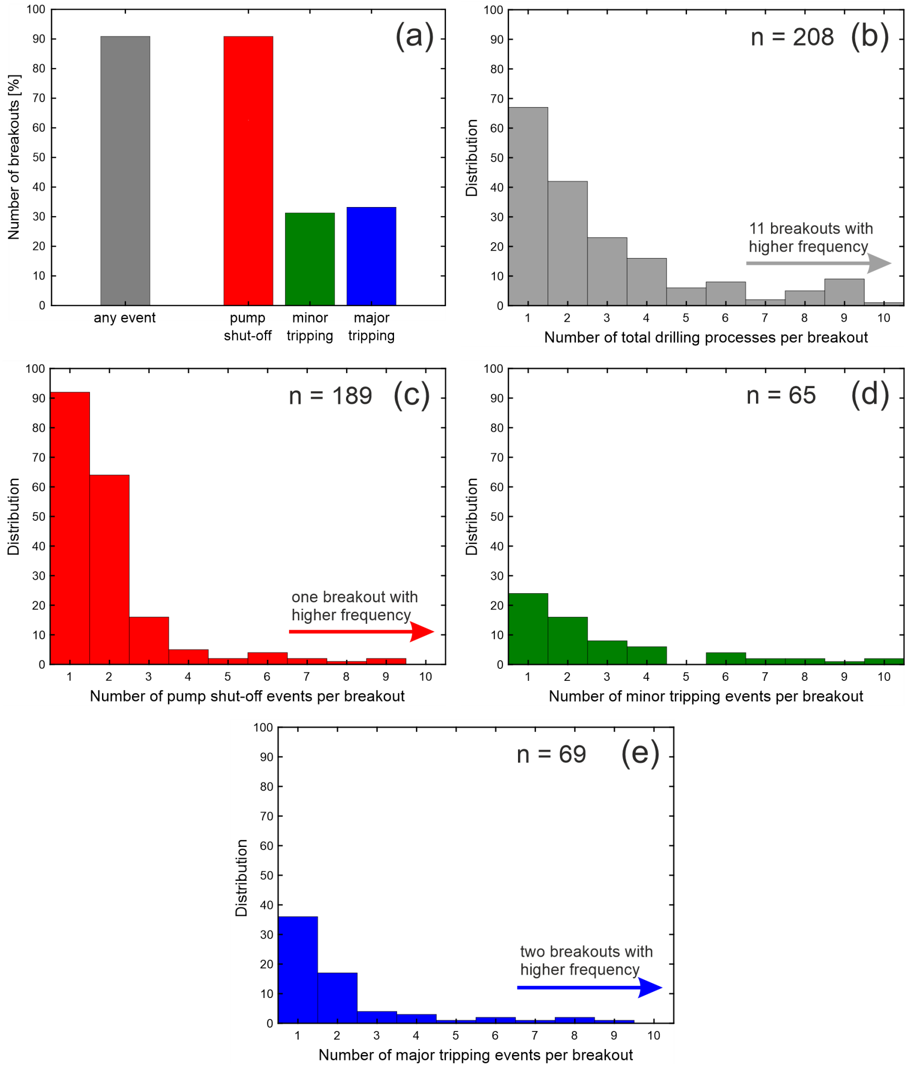

Figure B.3: Relationships between borehole breakouts and drilling-related processes (DRPs). (a) Number of breakouts associated with any DRP (grey) as well as pump shut-off events (red), minor (< 5 m; green), and major tripping events (> 5 m, blue). Distribution of the frequency of occurrence of the total amount of DRPs (b), pump shut-off events (c) as well as minor (d) and major (e) tripping events.

Figure B.3b shows the frequency histogram of all DRPs occurring during the investigated breakout sections. Moreover, the number of pump shut-off events (Figure B.3c), minor (Figure B.3d), and major (Figure B.3e) tripping operations are displayed. The color of the histograms corresponds to the respective bars in Figure B.3a; the x-axes of all histograms are further limited to a maximum of ten processes per breakout for better visibility. Figure B.3b illustrates the frequency distribution of all DRPs occurring during drilling-controlled breakout sections that are associated with at least one DRP. The vast majority (148) of these breakouts are related to less than five DRPs, whereas only a smaller amount of these breakout sections (31) is affected by up to ten DRPs. Breakouts that are related to more than ten DRPs are even scarcer (not displayed in the figure).

Breakout sections that comprise a relation to one or two DRPs are mostly related to pump shut-off events during connections, which are regularly performed while drilling (i.e. adding new stands of drill pipe to the drill string). This is underpinned by the frequency distribution of pump shut-off events displayed in Figure B.3c, showing that 156 out of 190 drilling-controlled breakout sections contain one or two pump shut-off events. Consequently, breakout sections comprising more than one or two DRPs are very likely additionally influenced by tripping operations. Figure B.3d and Figure B.3e show the frequency distributions of minor and major tripping operations, respectively. The frequency distributions show that most breakouts that are related to tripping operations only include a relatively low number of these operations. However, minor tripping operations tend to occur more frequently with higher absolute numbers, than their major counterpart does.

In the next step, we compared the frequency of occurrence of tripping operations and pump shut-off events within and outside of breakout sections. The intention was to improve our understanding of the relationship between the drilling procedure and breakouts. For tripping operations, this analysis has been limited to major trips with a length of more than five meters. It can be shown that both tripping operations and pump shut-off events occur significantly more frequently within breakout sections than outside. Tripping operations tend to occur by one order of magnitude more frequently within breakout sections than outside of these sections (9.27 compared to 0.92 tripping operations per 100 m measured depth (MD)). Similarly, pump shut-off events (e.g. connections) are also significantly more common within breakout intervals than outside (0.16 compared to 0.03 events per m MD). This illustrates that in depth intervals with breakouts more DRPs, which are not necessarily related to the normal drilling procedure, were performed. In addition, it can be stated that either these DRPs contribute to the causation of breakouts or that their execution is a reaction to the breakout occurrence.

The increased frequency of occurrence of tripping operations and pump shut-off events within breakout sections can be further identified within a crossplot (Figure B.4). The data are sorted by the wells they are originating from. The frequency of tripping operations and pump shut-off events for each well is represented by one marker for depths within breakouts (blue crosses) and outside of breakouts (red circles), respectively. The separation between the frequency of the two processes within breakout sections and outside of these is clearly visible, further pointing to a causal relationship between DRPs and the development of breakouts. Outside of breakout sections, both tripping operations and pump shut-off events occur very infrequently (except for one outlier) and show no clear relationship between the two parameters. Within breakout sections, however, the investigated data shows a linear trend between pump shut-off events and related major tripping operations. This means that individual trips were accompanied by a multitude of pump shut-off events, indicating a high likelihood that the breakouts in the respective wells were caused or enhanced by the interaction with these processes. This interpretation, however, is solely based on the statistical relationship between pump shut-off events and related major tripping operations. This means that as no individual breakouts were analyzed here, the actual stress state of the rocks surrounding the borehole, i.e. how close they already were to failure without the influence of the DRPs, was not considered.

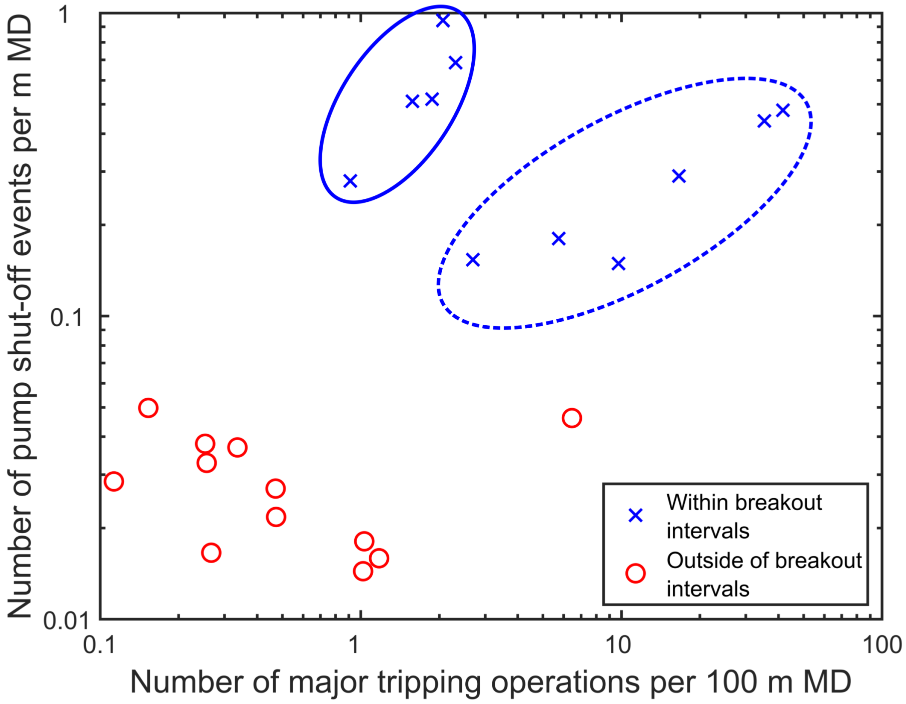

Figure B.4: Relationship between major tripping operations and pump shut-off events for different wells. Both processes occur more frequently within breakout sections (blue) than outside (red), pointing at a potential causal relationship. The data related to the breakout sections shows an increasing trend between the two processes, whereas outside of breakouts no trend is visible.

B.3.3 *Impact of drilling-related processes on borehole hydraulics*

A multitude of negative pressure anomalies, which deviate from the hydrostatic pressure profile, were observed in the investigated breakout sections. Additionally, some positive pressure anomalies occur as well. The most prominent pressure variations are linked to connections (89 occurrences), tripping operations (74 occurrences), or other periods with shut-off pumps (21 occurrences). The pressure variations related to connections do not only comprise pressure decreases, initiated by the pumps shut-off during the connection itself but also generate smaller pressure decreases after the pumps are switched on again. In total, about two-thirds of all investigated breakout sections (139 out of 208) comprise at least one negative pressure anomaly related to these processes. Furthermore, additional negative pressure anomalies related to downlinks, i.e. communication between the surface and the tools in the bottom hole assembly (BHA), could be observed in about a third of all breakout sections (61 out of 208). This means that most of the investigated breakouts contain reductions in the annulus pressure that are related to the drilling procedure and may contribute to the development of breakouts.

The observed pressure reductions are not only caused by different types of DRPs but also vary strongly in their magnitudes. Figure B.5 illustrates the normalized distributions of pressure reductions related to swab pressures, downlinks, and pump shut-off events. To minimize the influence of depth changes on the data (i.e. increasing hydrostatic pressure with depth), the histograms displayed in Figure B.5 show the distribution of the pressure reductions normalized to the average annulus pressure of the respective breakout section. Both, swab pressures and pressure reductions related to downlinks, vary in the range of 0 – 2 MPa, reaching up to four and eight percent of the average annulus pressure, respectively. Pump shut-off pressures comprise a broader range and reach much higher reductions of up to 6.5 MPa or 16 % of the average annulus pressure. Such pressure reductions have a strong impact on the effective circumferential stress around the borehole, increasing it significantly. This enhances the likelihood of rock failure (e.g. breakouts) as the effective circumferential stress may exceed the yield value of the rock (Peška and Zoback, 1995; Zoback, 2007). Hence, the high sensitivity of the annulus pressure and consequently also the effective circumferential stress on e.g. swab pressures (AlBahrani and Morita, 2020) or pump shut-off events (Li et al., 2020) have been investigated by various numerical studies.

Figure B.6 illustrates the relation between pressure drop anomalies and DRPs during an exemplary breakout section. Figure B.6a shows the MD of the drill bit (blue) and the image tool sensor (red) as a function of time. The deviations from a monotonous increase are caused by various pump shut-off events (P) and tripping operations (T). Figure B.6b shows the corresponding anomalies in pressure and temperature caused by these DRPs. It is depicted that tripping operations (e.g. T1 – T3) often cause a rather slow pressure decrease, followed by a very sharp increase in pressure (black ovals). These pressure variation patterns can be attributed to swabbing and surging pressures. Connections (or generally pump shut-off events) are associated with the strongest pressure reductions (dotted blue lines). Their magnitude of ca. 1.5 MPa for this example is seven times larger than the pressure reductions related to tripping operations (0.2 MPa). Both examples in Figure B.6 (P1 and P2) are additionally accompanied by minor tripping operations and multiple additional pump shut-off events.

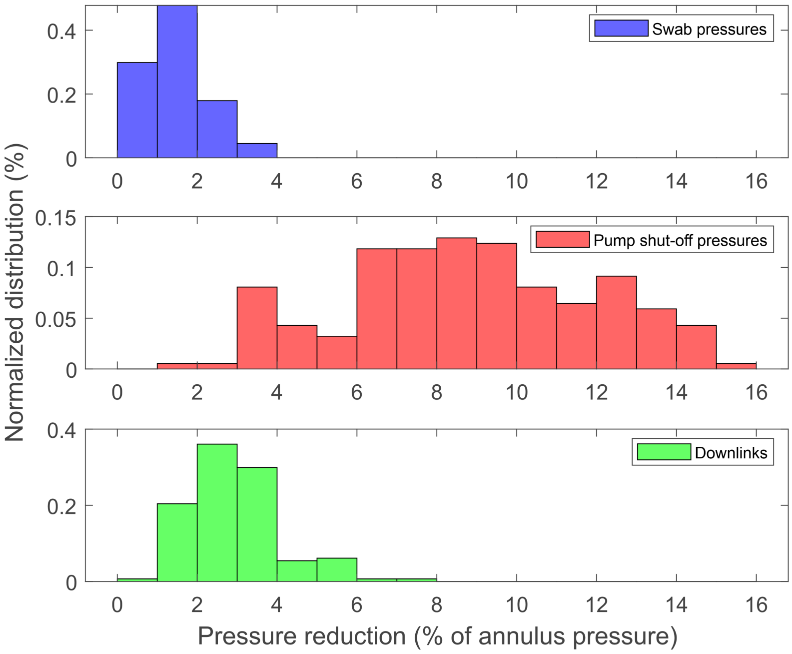

Figure B.5: Normalized distributions of observed pressure reduction mechanisms during breakout sections: Swab pressures related to tripping operations (blue), pump shut-off events (primarily related to connections; red), and downlinks (green). All histograms are normalized to the total number of occurrences. The pressure reductions displayed in the histograms range from 0.1 to 6.5 MPa.

Grey ovals highlight additional pressure reductions that are related to downlinks. The first and third downlink overlap with tripping operations that precede a connection. This can be explained by the communication of the team at the surface of the rig with the tools in the BHA preceding a connection, potentially during a reaming procedure. In contrast, the second downlink follows the completion of a connection. Tripping operation T1 may represent a reaming procedure occurring directly before connection P1. Here, in addition to the hydraulic influence caused by the pressure reduction, lateral mechanical forces are applied to the wellbore wall, potentially leading to both ductile and brittle failure of the rocks surrounding the borehole (AlBahrani et al., 2018).

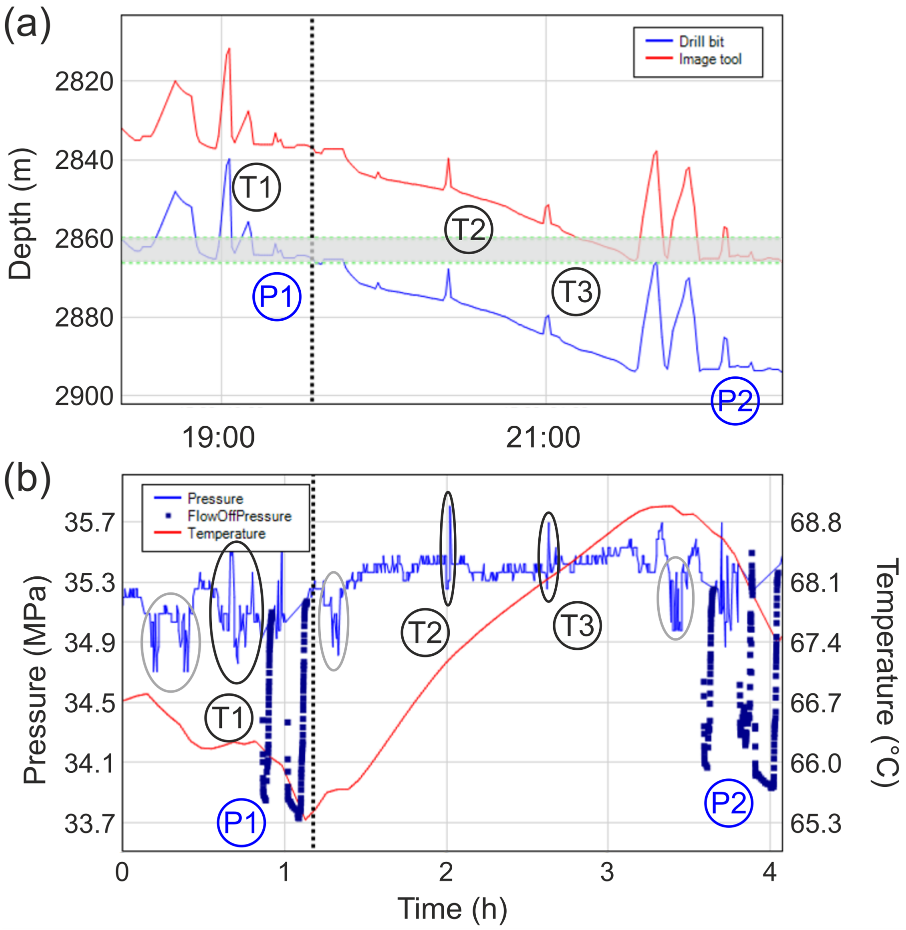

Figure B.6: Relationship between pressure anomalies and various drilling-related processes (DRPs) for an exemplary breakout section (the grey bar in (a) highlights its depth extent). (a) Bias between the occurrence of the breakout at the drill bit (blue) and detection at the image sensor (red), 27 m apart. (b) Pressure and temperature values recorded next to the drill bit in the breakout section. The labels T1, T2, and T3 mark different tripping operations (highlighted by black ovals in (b)); whereas the labels P1 and P2 mark two pump shut-off events. The labels apply both to variations in the depth of the drill bit and the image tool sensor (a) and their respective influences on pressure and temperature (b). Grey ovals further highlight pressure decreases that are related to downlinks. The displayed data originate from the Valdemar field in the Danish continental shelf.

B.3.4 *Time-dependent borehole instabilities*

In addition to the investigation of DRPs, LWD further offers the advantage of evaluating the mechanical development at logged sections. Here, we show the evolution of the resistivity image during relogs of the same depth interval. Figure B.7 illustrates such a development with an associated breakout growth during drilling, both in the azimuthal and in the MD direction. We compare the initial image to relog 1 recorded 112 min and relog 2 recorded 124 min after the logging of the respective depth section has taken place. Growth in breakout length and the opening angle is visible, even for the relatively small period between the two relogs.

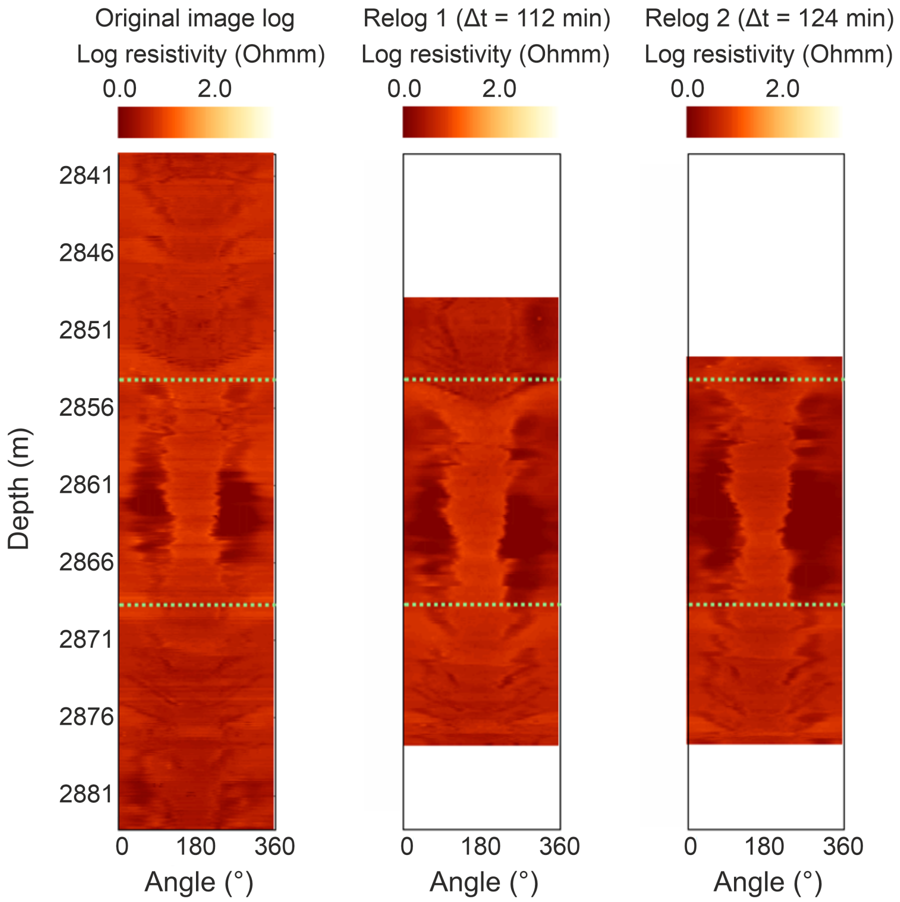

Figure B.7: Original image log (left) with a breakout section between 2860 – 2866 m and two relogs of the same depth interval illustrating breakout growth over time. Relog 1 (center) was recorded 112 min after the original log, whereas relog 2 (right) was recorded shortly afterward at a time lag of 124 min.

Figure B.7 exposes a primary growth of the breakouts in length to be ca. 2.5 m downwards and ca. 5 m upwards from an initial length of ca. 6 m. In the azimuthal direction, the growth is also visible with relog widths of up to 165° from initially 118°. Such observation adds to earlier analyses of azimuthal growth. As such, Zoback (2007) distinguishes between stable wells with initial breakout widths of less than 60° and unstable wells that are prone to temporal growth and subsequently increase the risk of failure due to their high initial breakout width of more than 90°. In this context, our observation resembles the second type of breakouts.

B.4 DISCUSSION

B.4.1 *Breakouts originating from dynamic borehole processes*

The existence of dynamic processes in the borehole (e.g. pressure fluctuations caused by DRPs) is well-known for many years (Burkhardt, 1961; Lake, 2006). However, only now with the rise of fully monitored LWD technology they can also be brought into context to borehole breakouts. Meng et al. (2019) emphasized the need for the consideration of dynamic hydraulic conditions in the borehole by numerical and experimental analyses highlighting the influence of these conditions on borehole stability.

The analyses of 208 breakout datasets, presented herein, highlight the possible impact of dynamic processes. This first investigation already enables a statistical assessment that should be further refined in the future. We observed strong pressure fluctuations of up to 16 % of the absolute annulus pressure in the openhole sections occurring within minutes after being drilled (Figure B.5). There are clear indications that they have been caused by DRPs, most prominently by pump shut-off events. These pressure changes consequently result in fluctuations in the effective circumferential stress around the borehole leading to possible rock failure (i.e. breakouts). Our results further show that these pressure (and subsequent stress) fluctuations occur in almost every investigated breakout section. This points out the need of controlling such pressure fluctuations in well operations for improving wellbore stability.

B.4.2 *Temporal development of borehole breakouts*

The exemplary result in chapter 3.4 (Figure B.7) shows that breakouts may grow in both length and opening angle. When a BHA contains multiple imaging tools that are installed at different offsets to the bit, it will acquire images at different times after the formation has been drilled. This opens the pathway to analyzing breakout geometries at different acquisition times in addition to utilizing relogs. Figure B.8 shows the recording of such a BHA having both, a resistivity and a density image tool, with offsets to the bit of 16 and 31 m, respectively. It can be seen that the breakout appears to widen slightly in the density image with a more pronounced shape, especially in the upper part of the breakout, which is only indicated in the resistivity image. Additionally, the different depth of investigation (DOI) of the two tools has to be considered. Whereas the resistivity image has a DOI of ca. 0.5 in, representing a breakout width directly at the borehole wall, the density image reading is related to a DOI of ca. 3.5 in. This results in an underestimation of the breakout width in the density image. Thus, it can be concluded that the breakout width grew significantly over time between the acquisitions of the two images.

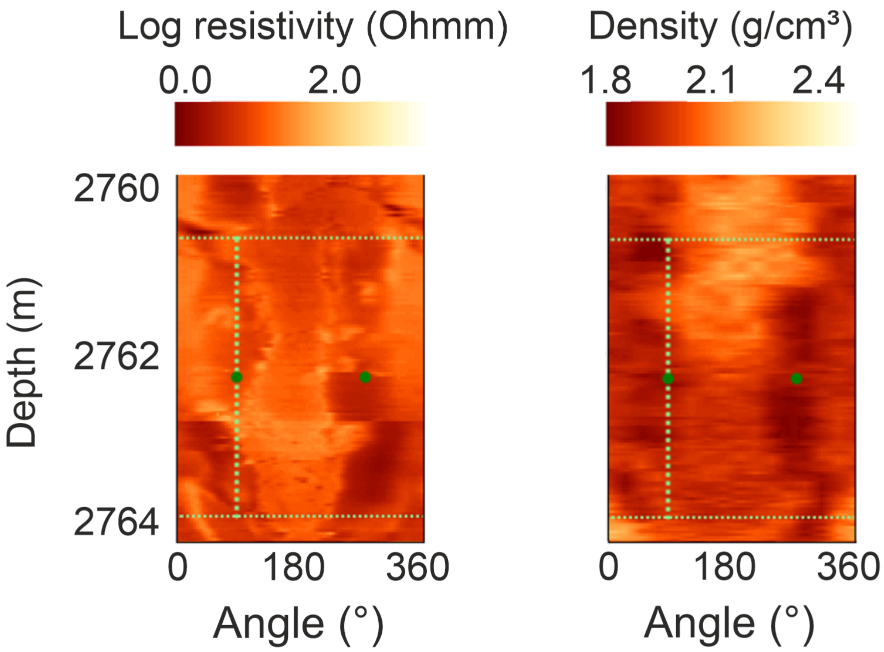

Figure B.8: Temporal geometrical changes of a breakout from a BHA with multiple imaging tools: a resistivity image with ≈16 m offset to the bit (left) and a density image with ≈31 m offset to the bit (right).

A similar analysis approach was described by Moore et al. (2011) evaluating changes in breakout width between two different images in the same BHA observed under constant hydraulic conditions. In contrast to these findings, the breakout development shown in Figure B.8 was influenced by pressure fluctuations due to a connection, which was performed during the acquisition of the resistivity image (closer to the bit). Hence, the annulus pressure was reduced by approximately 1.5 MPa. The connection, however, was already finished before the density image was recorded. This succession may lead to the conclusion that the borehole conditions captured by the density image were more strongly influenced by the connection than at the time when the resistivity image was acquired. These differences are especially prevalent in the shallower part of the images: the breakout is only slightly indicated in the resistivity image, whereas it is visible in the density image.

This observation over time may also explain earlier studies of the temporal development of breakouts (Azzola et al., 2019; Moore et al., 2011). It illustrates the influence of dynamic conditions on breakout development. It also has consequences for the derivation of far-field stress magnitudes as they are directly related to the breakout width (Barton et al., 1988).

B.5 CONCLUSIONS

Our investigation provides a clear correlation between the occurrence of borehole breakouts and DRPs exists, mostly due to connections and tripping operations. When major DRP activities took place in a specific borehole interval, it also exhibits a strong breakout signature. The fact that in breakout sections, DRPs were conducted ten times more often than in other drilling sections points to a causal relationship between the drilling activity and the origin of breakouts. It is therefore suggested that their occurrence not only depends on rock strength and the naturally occurring stress state already beyond the yield envelope but also on drilling activities leading to an effective stress state beyond failure. This concept could only be obtained using modern LWD technology with real-time drilling data acquisition – traditional wireline logging would not allow for this observation. It has the potential to lead to novel breakout analyses.

DRPs have also a significant impact on the conditions within and around a borehole. This includes the pressure and temperature fields as well as mechanical rock properties. Frequent dynamic changes in pressure and temperature at the bottom hole may serve as a proxy for breakouts. We observed that dynamic drilling-induced pressure changes may directly contribute to wellbore failure. Especially pump shut-off events (e.g. during connections) could be related to significant pressure drop anomalies of up to 16 % of the average annulus pressure.

These findings can also support decision processes to secure borehole stability. They demonstrate the necessity to control the downhole pressure to prevent changes in the effective stresses around a well. When an unexpected pressure change is observed, possible countermeasures such as mud weight adaptation should be taken. Alternatively, a larger safety margin on the pre-drilling pressure window could be applied. In contrast to these preventive measures, actively initiated pressure changes and related perturbations of the effective stress can cause wellbore instabilities in specific sections. DRPs could also influence the occurrence of tensile fractures (i.e. DIFs or hydraulic fractures parallel to S_{max}) or compressive borehole breakouts (i.e. parallel to S_{min}). The results of this study show that drilling can accidentally stimulate a borehole and future drilling operations have to be adapted.

In terms of research on mechanical behavior, relogs of breakout intervals open the perspective of investigating the time-dependency of breakouts and the influence of DRPs thereof. Our analysis shows that breakouts may tend to grow both azimuthally and in the measured depth direction, confirming the findings published earlier.

It adds an important component for geomechanical analyses when using the azimuthal width of breakouts to determine the magnitude of the maximum horizontal stress. We could further show that running a BHA with different image tools additionally enables us to investigate time-dependent borehole failure and to show the direct impact of DRPs on breakout growth.

The data used in this study only rarely included abundant relog sections or multiple images with sufficient quality. In a thorough investigation, this data basis should be improved to better quantify the causality of the relationship between DRPs and the occurrence of breakouts. For this purpose, future research should focus on clarifying this causality between DRPs and breakouts. This could be realized by comparing two nearby boreholes with one having previously performed DRPs and the other rather avoiding it in similar depths.

ACKNOWLEDGMENTS

We thank the two reviewers Thomas Poulet and Michal Kruszewski for their very comprehensive and extraordinarily helpful review of this paper, which helped us significantly to improve this paper. We acknowledge Baker Hughes for the opportunity to create this case study. We further thank Jörg Meixner (Baden-Württemberg State Authority for Geology, Mineral Resources, and Mining) for his contribution in the early stages of this study. This study is part of the subtopic "Geoenergy" in the program "MTET - Materials and Technologies for the Energy Transition" of the Helmholtz Association. The authors are responsible for the content of this publication.

C

STRICKER ET AL. (2024) ADDITIONAL FILE: VALIDATION OF TIGER

C.1 OVERVIEW

This document presents the results of a validation study comparing the open-source code TIGER (Egert et al., 2022; Gholami Korzani et al., 2020) to the analytical solution of Rudnicki (1986), following the procedure outlined in Altmann et al. (2010). A 3D cylindrical numerical model with a radius and depth extent of 25 km each, consisting of 605'417 tetrahedral elements, was employed. At a depth of five km, a constant concentric injection of 0.02 $m^3 s^{-1}$ was applied. The bottom and shell surface of the cylindrical model were constrained in normal direction. No constraints were applied to the top of the model. Additionally, gravity was not considered in the simulation. Undrained Neumann boundary conditions were applied to all sides of the model, preventing fluid flow out of the model. Table C.1 summarizes the remaining model parameters.

Table C.1: Parametrization of the model used to validate the open-source code TIGER against the analytical solution of Rudnicki (1986).

Parameter	Value
Permeability	10^{-14} m²
First Lamé constant	15.2 GPa
Second Lamé constant	10.2 GPa
Young's modulus	26.4 GPa
Poisson's ratio	0.3
Porosity	0.091
Effective porosity of the caprock	0.01
Specific rock density	2500 kg m^{-3}
Biot coefficient	0.45
Compressibility of the solid porous media	4.55×10^{-11} Pa^{-1}

C.2 BENCHMARK OF SPATIAL PRESSURE AND STRESS STATE DISTRIBUTION

Figure C.1 presents the distribution of the pressure and stress along the x-axis, extending radially from the injection point to the model's shell surface. The analytical solution and the numerical simulation, conducted after 34 days of simulation, are compared. High correlation coefficients of 0.9998 for the pressure (red), 1.0000 for the radial stress (green; in x-direction), and 0.9945 for the tangential stress (blue; in z-direction) indicate excellent agreement, validating the numerical simulation using TIGER.

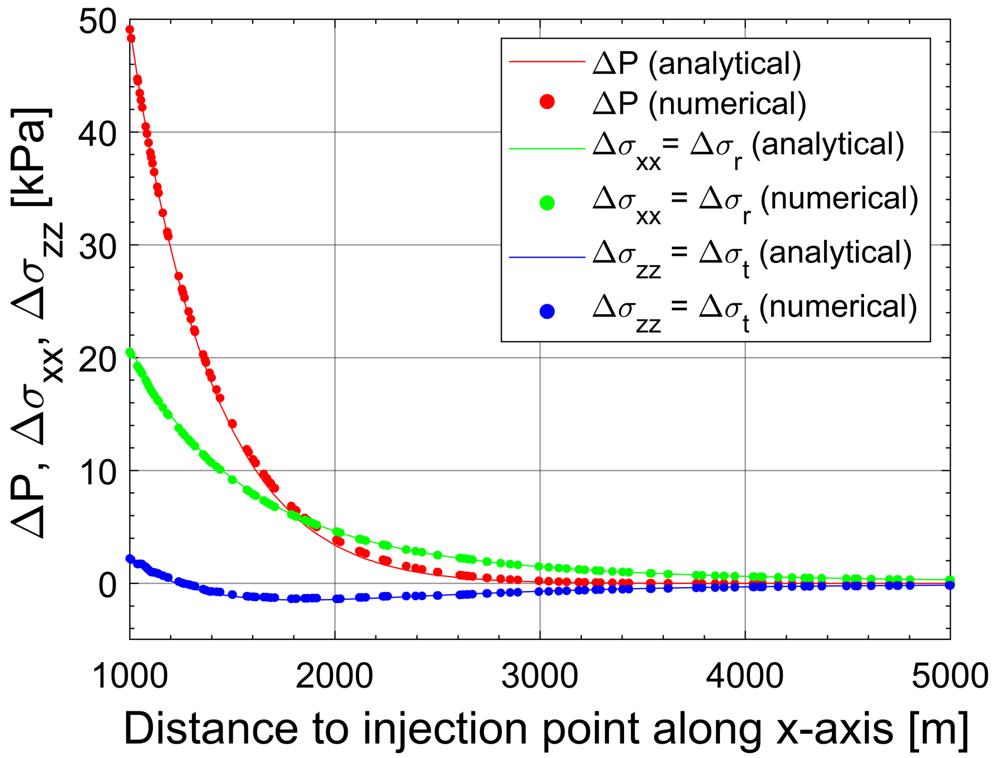

Figure C.1: Results of the spatial benchmark between TIGER and the analytical solution of Rudnicki (1986). The filled circles represent the results of the numerical simulation with TIGER and the solid lines the calculation results of the analytical solution, for the pore pressure (red), the radial stress (in x-direction; green), and the tangential stress (in z-direction; blue) along the x-axis in a distance of 1000 m to 5000 m to the injection point.

C.3 BENCHMARK OF TEMPORAL PRESSURE AND STRESS STATE DISTRIBUTION

Similarly, to the spatial benchmark, Figure C.2 depicts the pressure and stress state at different simulation times for an observation point located along the x-axis, 206 m from the injection point. For this validation scenario as well, high correlation coefficients of 0.9999 for all three parameters (pressure, radial stress, tangential stress) reaffirm the validity of the numerical simulation using TIGER.

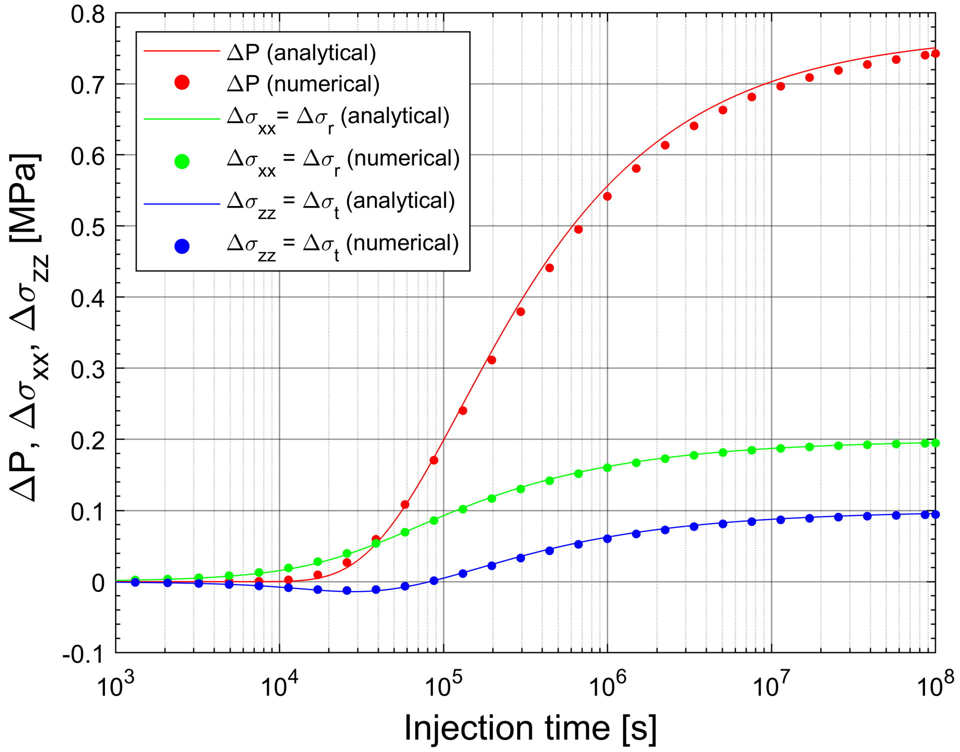

Figure C.2: Results of the temporal benchmark between TIGER and the analytical solution of Rudnicki (1986). The filled circles represent the results of the numerical simulation with TIGER and the solid lines the calculation results of the analytical solution, for the pore pressure (red), the radial stress (in x-direction; green), and the tangential stress (in z-direction; blue) at an observation point in a distance of 206 m along the x-axis.